

MECHANICAL PROPERTIES OF NICKEL ZIRCONIA
INTERPENETRATING PHASE COMPOSITES

MECHANICAL PROPERTIES OF NICKEL ZIRCONIA
INTERPENETRATING PHASE COMPOSITES

By

JAMES REAVLEY CLARKE, B.Sc. (Eng.)

A Thesis

Submitted to the School of Graduate Studies

In Partial Fulfillment of the Requirements

for the Degree

Masters of Engineering

McMaster University

© Copyright by James Reavley Clarke, 1997

MASTERS OF ENGINEERING (1997)
(Materials Science and Engineering)

MCMASTER UNIVERSITY
Hamilton, Ontario

TITLE: Mechanical Properties of Nickel Zirconia Interpenetrating Phase
Composites.

AUTHOR: James Reavley Clarke B.Sc. (Eng.) Queen's University

SUPERVISOR: Professor D.S. Wilkinson

NUMBER OF PAGES: xiii, 127

ABSTRACT

This thesis describes the processing and testing of homogeneous nickel and fully yttria stabilized cubic zirconia interpenetrating phase composites. This work was part of a research program investigating step graded Functionally Gradient Materials. This work was focused on understanding the deformation behaviour of the interpenetrating composites near the percolation threshold of the ceramic phase.

The composite grades selected for this study included the pure materials, nickel and zirconia, as well as composites with volume fractions of zirconia of 5%, 10%, 15%, 20% and 25%. These compositions were selected to provide data near the zirconia percolation threshold.

Processing of the composites involved tape casting, lamination, organic removal, reduction, and hot pressing. All composites except the 5% volume fraction achieved densities greater than 98% of theoretical.

Tensile testing was performed on composite grades up to and including the 20% zirconia material, and flexural testing was carried out on the 25% material and pure zirconia. The maximum tensile strength of 530 MPa was obtained in the 10% material resulting from load transfer to the zirconia phase. Ductility decreased as the volume fraction of zirconia increased, with no macroscopic plasticity above 15% volume fraction zirconia. Hardness tests and compression tests were carried out on all composite grades and the yield stress was determined.

The compressive yield stress was found to be related to the hardness by the equation:

$$H = 6\sigma_y$$

This relationship is a result of the constraint imposed on the nickel phase by the zirconia network.

Measurements of damage in one pure nickel sample were also performed. The area fraction of voids as a function of local strain was found to follow an exponential relationship. The Young's modulus of each material was determined ultrasonically and found to be uniform as expected.

Modeling of the tensile specimens indicated that materials above the zirconia percolation threshold work harden more rapidly than those below it. This is not accounted for in the model by Ravichandran.

ACKNOWLEDGEMENTS

I would like to thank all those people who made the preparation of this manuscript possible. Specifically, I would thank:

Dr. Wilkinson for providing an exciting research topic and a stimulating working environment.

Dr. Weatherly for his assistance with editing and proofreading and for his participation in extra-curricular activities.

Connie Barry, Martin Van Oosten, Chris Butcher and Klaus Schultz for their assistance in carrying out my research and for their advice freely given.

The Graduate Students of MSE, especially Brian, Joey, Colin and Mike for their friendship.

My fellows in A206 for their support, guidance and good humour, and especially Doris Clayton, a fellow purveyor of the black art of casting.

My parents for their continuing support and encouragement in all my endeavours, with special mention to my mother Jean for her efforts in preparing this document.

Finally, and most importantly, I would like to thank my future wife Laura Stiles. Her support, encouragement, and understanding are appreciated beyond measure.

TABLE OF CONTENTS

Abstract	(iii)
Acknowledgments	(v)
Table of Contents	(vi)
List of Tables	(ix)
List of Figures	(x)
CHAPTER 1: INTRODUCTION	1
CHAPTER 2: LITERATURE REVIEW	4
2.1 Tape Casting	4
2.2 Powder Consolidation	8
2.2.1 Sintering	9
2.2.2 Hot Pressing	10
2.3 Interpenetrating Phase Composites	11
2.3.1 Liquid Metal Infiltration	13
2.3.2 Directional Metal Oxidation	13
2.3.3 Solid State Decomposition	14
2.3.4 Cosintering	15
2.4 Percolation Theory	16
2.5 Mechanical Properties	21
2.5.1 Metals and Ceramics	21
2.5.1.1 Ductile Fracture in Metals	24
2.5.2 Behaviour of Metals and Ceramics in Composites.....	26
2.5.2.1 Thermal Expansion Mismatch	26
2.5.2.2 Strain Induced Dislocations	26

	2.5.2.3 Elastic Moduli	28
	2.5.2.4 Constraint	29
	2.5.3 Metal Ceramic Interfaces	31
	2.5.4 Metal Ceramic Composites	32
	2.5.5 Interpenetrating Phase Composites	35
	2.5.5.1 Modeling of IPCs	37
	2.5.5.2 Experimental Data on IPCs	40
CHAPTER 3:	PROCESSING	42
3.1	Raw Materials	42
3.2	Tape Casting and Lamination	44
3.2.1	Lamination	47
3.3	Organic Burnout and Reduction	48
3.4	Hot Pressing	53
CHAPTER 4:	EXPERIMENTAL PROCEDURE	55
4.1	Tensile and Four Point Bend Specimen Preparation	55
4.2	Compression Tests	56
4.3	Microstructural Analysis	57
4.4	Young's Modulus	59
4.5	Hardness Testing	59
4.6	Fractography	59
4.7	Carbon Analysis	60
CHAPTER 5:	RESULTS	62
5.1	Microstructure	62
5.2	Deformation Behaviour	72
5.3	Fractography	82
5.4	Young's Modulus Measurements	92

5.5	Hardness Testing	92
5.6	Carbon Analysis	92
CHAPTER 6:	DISCUSSION	95
6.1	Processing	95
6.1.1	Raw Materials	95
6.1.2	Tape Casting Process	96
6.1.3	Lamination, Burnout and Reduction	97
6.1.4	Hot Pressing	98
6.2	Microstructure	99
6.2.1	Percolation Threshold	101
6.3	Fractography	102
6.3.1	Fracture Mechanisms	102
6.3.2	Damage in Nickel Sample	103
6.4	Mechanical Properties	104
6.4.1	Flexural Strength	105
6.4.2	Tensile Strength	106
6.4.3	Yield Strength	108
6.4.4	Young's Modulus	111
6.4.5	Microstructural Effects	112
6.5	Modeling Deformation	115
6.6	Summary of Mechanical Properties	120
CHAPTER 7:	SUMMARY AND CONCLUSIONS	121
References		124

LIST OF TABLES

Table 2.1:	Site and Bond Percolation Thresholds for Different Lattices (Stauffer and Ahonary, 1994)	17
Table 3.1	Powder Compositions	43
Table 3.2	Compositions of Slurries	46
Table 3.3	Typical Thickness of Dried Tapes	47
Table 5.1	Densities of Composites	70
Table 5.2	Grain Size of Materials	71
Table 5.3	Carbon Levels Throughout Processing	92

LIST OF FIGURES

Figure 2.1 Slurry Preparation Flowsheet (Roosen, 1988)	7
Figure 2.2 Tape Casting Apparatus	8
Figure 2.3 Illustration of R-curve Behaviour Showing Rising Fracture Toughness as a Function of Crack Length	12
Figure 2.4 Square Lattice with the Probability of Each Site Being Occupied Being 0.6 Illustrating the Presence of an Infinite Cluster	18
Figure 2.5 Illustration of Excluded Volume Around 2D Objects (Nan, 1993)	19
Figure 2.6 Percolation Threshold Dependence on Particle Size Ratio (Nan, 1993)	20
Figure 2.7 Stresses in Metal and Ceramic Portions of Composite	27
Figure 2.8 Critical Condition for Orowan Strengthening	33
Figure 2.9 a and b. Parallel and Series Representations of Phases in a Composite Material	35
Figure 2.10 Finite Difference Model of Discontinuous Fibre with Imposed Far Field Matrix Strain	36
Figure 2.11 Unit Cell in Ravichandran Model (Ravichandran, 1994)	37
Figure 2.12 Stress Strain Behaviour and Predictions for Silver Iron System	39
Figure 2.13 Stress Strain Behaviour and Predictions for Copper Silver System	40

Figure 2.14 Strength and Toughness Variation with Volume Fraction of Aluminum in Composite	41
Figure 3.1 Illustration of Lamination Components	49
Figure 3.2 Thermogravimetric Analysis Curve for Burnout of 25% Composite in Air	51
Figure 3.3 Burnout Profile for Laminated Discs	52
Figure 3.4 TGA curve of Nickel Sample in Reducing Atmosphere	54
Figure 4.1 Four Point Bend Test Rig	58
Figure 5.1 Transverse and Parallel Orientations in Samples	63
Figure 5.2 (a) Parallel and (b) Transverse Optical Micrographs of 5% Zirconia Composite (800× magnification)	64
Figure 5.3 (a) Parallel and (b) Transverse Optical Micrographs of 10% Zirconia Composite (800× magnification)	65
Figure 5.4 (a) Parallel and (b) Transverse Optical Micrographs of 15% Zirconia Composite (800× magnification)	66
Figure 5.5 (a) Parallel and (b) Transverse Optical Micrographs of 20% Zirconia Composite (800× magnification)	67
Figure 5.6 (a) Parallel and (b) Transverse Optical Micrographs of 25% Zirconia Composite (800× magnification)	68
Figure 5.7 Optical Micrograph of Etched Surface of 15% Composite	71
Figure 5.8 Flexural Strengths Determined Using Four Point Bend Test	72
Figure 5.9 Stress Strain Curve for 25% Composite Undergoing Four Point Bending	73
Figure 5.10 Stress Strain Curve for 100% Zirconia Sample Undergoing Four Point Bending	74
Figure 5.11 Tensile Strength of Composites	75

Figure 5.12 Stress Strain Curve of Pure Nickel Sample	76
Figure 5.13 Stress Strain Curve of 10% Zirconia Sample	77
Figure 5.14 Strain to Failure for Composites in Tensile Test	78
Figure 5.15 Compressive Stress Strain Curve for Pure Nickel	79
Figure 5.16 Compressive Stress Strain Curve for 10% Composite	80
Figure 5.17 Compressive Stress Strain Curve for 25% Composite	81
Figure 5.18 Micrograph of Pure Nickel Fracture Surface	83
Figure 5.19. Close-up of Particles on Nickel Fracture Surface	83
Figure 5.20. Micrograph of 5% Composite Fracture Surface	84
Figure 5.21. Micrograph of 10% Composite Fracture Surface	84
Figure 5.22. Image of 15% Composite Fracture Surface	85
Figure 5.23. Close-up of Ductile Fracture in 20% Composite	85
Figure 5.24. Micrograph of 25% Composite Fracture Surface	86
Figure 5.25. Fracture Surface of 100% Zirconia Sample	86
Figure 5.26 EDX of Fracture Surface of Nickel Sample away from Particles	88
Figure 5.27 EDX of Particle on Fracture Surface of Nickel Sample	89
Figure 5.28 Damage in Necked Region of Tensile Sample	90
Figure 5.29. Image of Sectioned Nickel Sample Immediately Behind Fracture Surface	91
Figure 5.30. Image of Sectioned Nickel Sample Several Millimeters From Fracture Surface	91
Figure 5.31 Ultrasonic Measurement of Young's Modulus	93
Figure 5.32 Vickers Microhardness Measurements	94

Figure 6.1 Modeling of Plasticity in Pure Nickel	108
Figure 6.2 Illustration of Deep Piercing with $H = 5\sigma_y$	110
Figure 6.3 Yield Stress of Composites Determined Through Hardness and Compression Tests	110
Figure 6.4 Model of 5% Zirconia Composite Based on Ravichandran (1994)	117
Figure 6.5. Model of 10% Zirconia Composite Based on Ravichandran (1994)	118
Figure 6.6. Model of 15% Zirconia Composite Based on Ravichandran (1994)	119

CHAPTER 1

INTRODUCTION

The objective of fabricating composite materials is to produce a mixture that has more desirable properties than any of the starting materials. For example, glass fibres and epoxy resins are combined to make a material that is more fracture resistant than glass (Kelly and MacMillan, 1989), but much stiffer and stronger than the epoxy resins. Ceramic particles can be incorporated into a metal to produce a stiff, light composite material that is more brittle than a metal, but much less brittle than a pure ceramic.

Particles and fibres are two examples of the traditional reinforcement morphologies in composite materials. A particle will in general provide isotropic reinforcement, but is limited in potential because of its small area of surface contact with the matrix of the composite. A fibre can provide excellent reinforcing properties in one orientation relative to the axis of the fibre, but typically will not improve, and may actually reduce the level of performance in other orientations.

One potential solution to this problem with the reinforcing phase is to create two fully interpenetrating networks of each phase to produce an interpenetrating phase composite (IPC). This would result in large phase regions that would provide better reinforcement than isolated particles, but the network

structure would provide isotropic reinforcement that is not available in a simple fibre composite. Even a laminated fibre composite can only successfully reinforce biaxially, while in principle an IPC would be able to reinforce triaxially.

The ultimate goal of the overall research into IPCs is to develop an understanding of the properties of IPC materials, in order to generate a model system to investigate plasticity models and fracture behaviour. For this reason, nickel and fully stabilized zirconia were selected as the composite components. They are well matched in thermal expansion and in Young's Modulus which will facilitate the development of a model.

The secondary objective of the research is to investigate the properties of functionally gradient materials (FGMs) based on IPCs. An FGM is a composite in which the volume fraction of the reinforcing phase is deliberately adjusted in different regions of a sample. For example, an FGM that is completely ceramic on the inner surface and is blended through a number of steps into a pure metal on the outer surface could be used in a component such as an engine cylinder. In principle, this would produce a high temperature, wear resistant inner surface, yet enable the component to be welded into position.

A tape casting technique was used to prepare the IPCs to facilitate the preparation of step graded samples. Using tape cast materials, it should be possible to produce the gradient materials by simply using tapes with different compositions in the lamination and hot pressing stages.

In this phase of the research the mechanical properties of IPCs with zirconia volume fractions near the percolation threshold of zirconia were investigated in order to understand the effect of percolation on the properties of metal matrix composites.

CHAPTER 2

LITERATURE REVIEW

The techniques used to fabricate IPCs are described briefly, followed by an overview of the resulting microstructure obtained. Some elements of percolation theory and the expected benefits to the mechanical properties are also discussed. A summary of the nature and development of damage in regions of ductile fracture conclude the literature review.

2.1 Tape Casting

Colloidal processing has been used to prepare ceramic materials with excellent homogeneity, resulting in superior properties in the final products (Lange, 1989). The technique allows for high levels of purity and presents numerous opportunities to eliminate large particles or agglomerates that could hinder the final densification processes. One processing technique using colloidal suspensions is the tape casting technique, on which a number of reviews have been written (Mistler et al., 1978). In tape casting, a powder is dispersed in a solvent and polymerizable binders and plasticizers are added (Williams, 1976). The viscosity of the slurry is dependent on a number of factors, including the powder particle size and morphology (Velamakanni and Lange, 1991), the solids loading,

and the relative amounts of dispersant, plasticizers and binders. Flexibility and green density of the final tape are affected by the ratio of plasticizers and binders. As the solvent evaporates, the binder polymerizes into a network that holds the powder particles in place. The plasticizers modify the network to ensure that the tape is flexible enough to handle in further processing.

Typical mixtures of materials for organic tapes can be found in the review by Williams (1976). Each of the components of the mixture is selected for a number of properties that facilitate the casting process. The solvent must be able to dissolve the plasticizers, binders, and the dispersant while being unreactive with the powders used. The viscosity of the solvent should be low, but the vapour pressure should be high to facilitate the drying process.

The binders and plasticizers must be selected as a system rather than as individual components. They must be able to form the network at relatively low concentrations and must not impede either the activity of the dispersant or the solvent. In addition, they must form a system that is stable under ambient conditions to enable storage after processing.

The dispersant is a very important component of the system, as it allows the powder particles to deflocculate and hence reduces the viscosity of the suspension (Cannon et al., 1989a). Two mechanisms have been proposed for dispersal: steric hindrance and charge repulsion. In steric hindrance, the dispersant is adsorbed on to the surface of the particle and because of its physical presence prevents the particles from coming into contact with each other. This is generally

the mechanism of action for dispersants with large molecular weights (Cannon et al., 1989b). The charge repulsion mechanism generates a surface charge of uniform polarity on the particles and hence leads to electrostatic repulsion.

Except for the solvent, all of the components in the tape casting system must also have acceptable burnout characteristics and must not leave residual ash or impurities in the final product. The suitability of different components can be modified by selection of the burnout atmosphere and temperature profile.

The tape casting slurry is formulated to be a shear thinning fluid, so that the viscosity will drop when it is subjected to a shearing force. In the doctor blade technique of tape casting, the slurry is passed under a sharp blade which generates the required shearing force. As the slurry passes under the blade, it thins and forms the tape. The viscosity increases after the shearing force is removed, ensuring that the tape remains in place on the substrate.

The procedure for slurry preparation is illustrated in flow sheet form in Figure 2.1. The powder, dispersant, and solvent are mixed together and ball milled for 24 hours to break up any soft agglomerates that may be present. The binders and plasticizers are then added and milled for up to 24 hours to ensure adequate mixing. Prolonged or insufficient milling at this stage can lead to poor green densities in the tapes (Mistler et al., 1978). The slurry is then degassed immediately before casting in order to eliminate trapped gases that would form bubbles and disrupt the homogeneity of the tape. After being poured into the

casting reservoir, the tape caster (Fig 2.2) is pulled across a substrate such as a glass plate and the tape is formed.

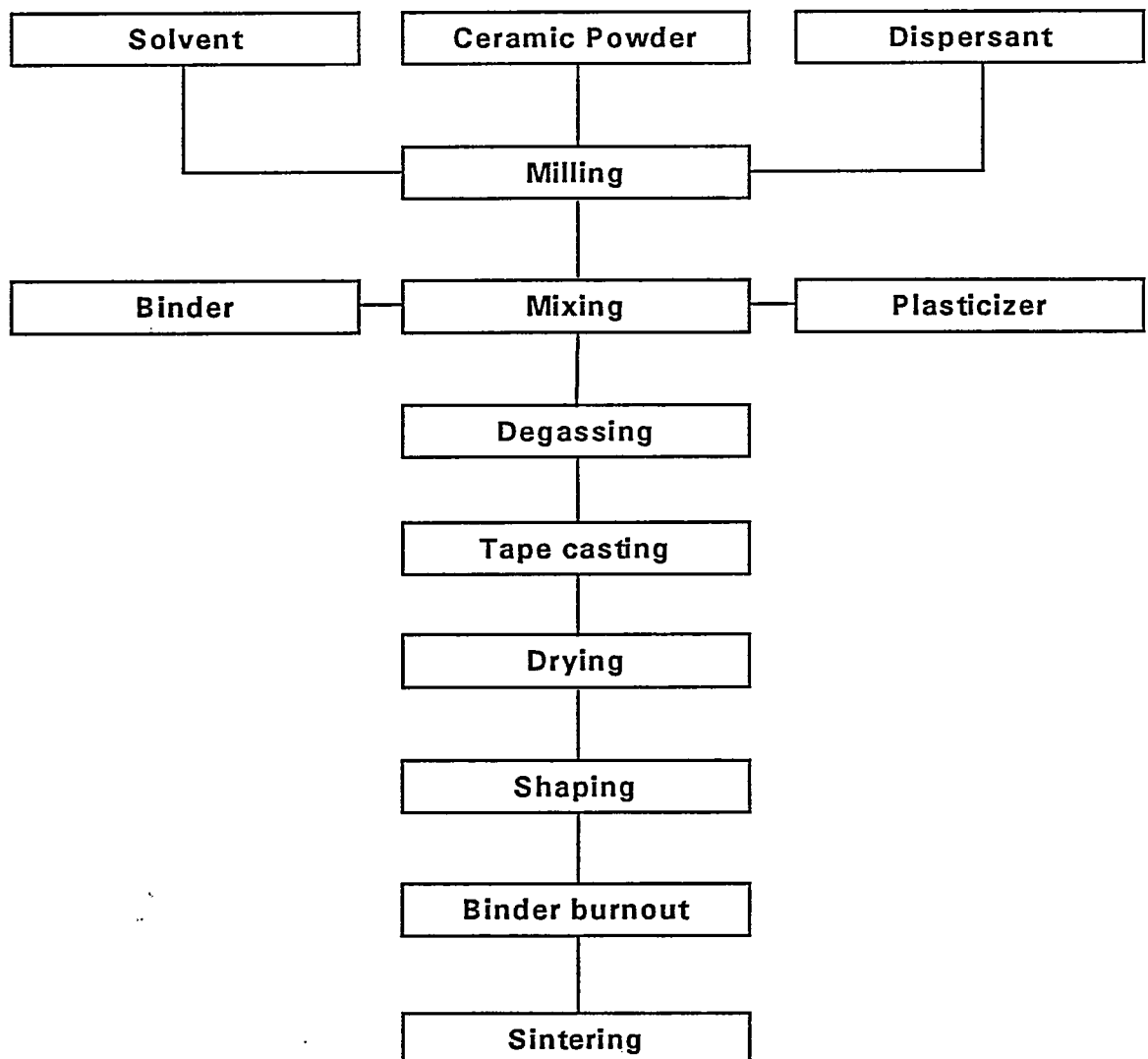


Figure 2.1 Slurry Preparation Flowsheet (Roosen, 1988)

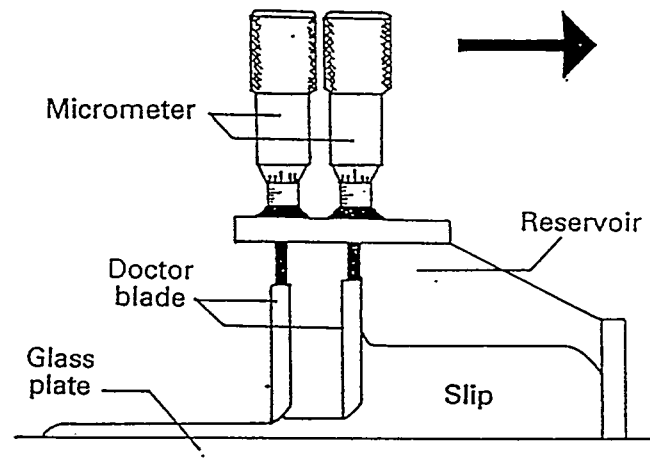


Figure 2.2 Tape Casting Apparatus

The solvent is allowed to evaporate, after which the tape can be removed from the substrate and handled for further processing.

2.2 Powder Consolidation

Once the tape has been cast and the organic materials have been removed, the material must be consolidated to full density. A number of techniques can be used for this process. Many reviews on the densification of ceramic materials and composites have been written. (See, for example, Stuijts, 1976; Wu, 1986; and Richerson, 1992). The two techniques that are discussed here in detail are pressureless sintering, as it forms the basis on which all other techniques are built,

and hot pressing, as it was the technique used to consolidate the materials in this research project.

2.2.1 Sintering

When a powder is heated, diffusion will occur in order to reduce the surface area to volume ratio of the material. The driving force for this diffusion is the vapour pressure or the vacancy concentrations near a curved surface, relative to those found at a plane surface. In the case of vapour transport diffusion between two particles, the point of contact between particles has a small radius of curvature pointed away from the contact point, producing a low vapour pressure. In contrast, the surfaces of the particles have a larger radius of curvature pointed towards the inside of the particles, producing a higher vapour pressure. This leads to a pressure differential that draws matter to the point of contact, joining the two particles but not reducing the volume. This form of mass transport will tend to round off particles and reduce jagged edges but does not lead to densification of the material.

In a similar fashion, the concentration of vacancies beneath a curved surface is modified, and a migration of vacancies away from the point of contact leads to a flux of atoms into the growing neck, joining the two particles. If the source of the atoms moving to the neck is the bulk of one of the particles, then the two particles will be drawn together. This is the mechanism by which densification occurs during sintering.

2.2.2 Hot Pressing

Isostatic pressing involves heating the sample and applying pressure using an inert gas, which is typically argon. For isostatic pressing to be effective, the porosity must be of a closed form because the pressure differential between the outside atmosphere and the trapped gas in the closed pore is used to drive the densification. The pressure exerted by the gas acts as a driving force for the shrinkage of pores and the migration of excess vacancies to the surface of the material.

In uniaxial pressing a set of pistons and a die are used to apply pressure to the powder during heating. Unlike isostatic pressing, the force is acting directly on the particles, not on the porosity of the sample, so it is effective on systems with open porosity. There are a number of mechanisms of action, the most important being particle sliding, increased chemical potential leading to more rapid diffusion, and dislocation activation.

Both uniaxial and isostatic pressing have advantages over conventional sintering since they allow densification to occur at a lower temperature in a shorter time period. The result of the lower temperature is a finer grain size in the final product since there is less opportunity for grain growth to occur. These techniques have also been effective in densifying materials, such as boron carbide and silicon carbide, that are otherwise very difficult to sinter (Kingery et al., 1976).

2.3 Interpenetrating Phase Composites

An IPC is a material composed of two or more phases which are fully continuous throughout the bulk of the substance (Clarke, 1992). This means that a path can be traced between any two points in an IPC along an unbroken pathway composed of a single phase. This property leads to a number of potential applications for these materials.

For example, in the semiconductor industry it is desirable to have chip substrates with a low dielectric constant but high thermal conductivity. An IPC such as alumina with 10% of aluminum could suit the purpose. IPC materials show excellent resistance to grain growth at high temperatures (French, 1992 and 1990) because each phase can only experience grain growth until it encounters the other phase.

The mechanical properties of IPC materials offer the possibility of interesting applications, specifically the potential for exhibiting R-curve behaviour during fracture (Prielipp et al., 1995; Rodel et al., 1995). The presence of a metal reinforcing phase within the ceramic matrix presents the opportunity for crack bridging to occur behind the crack tip. Ligament formation shields the crack tip and can lead to crack arrest within a specimen. This is a result of the effective fracture toughness increasing as the crack grows, as illustrated in Figure 2.3.

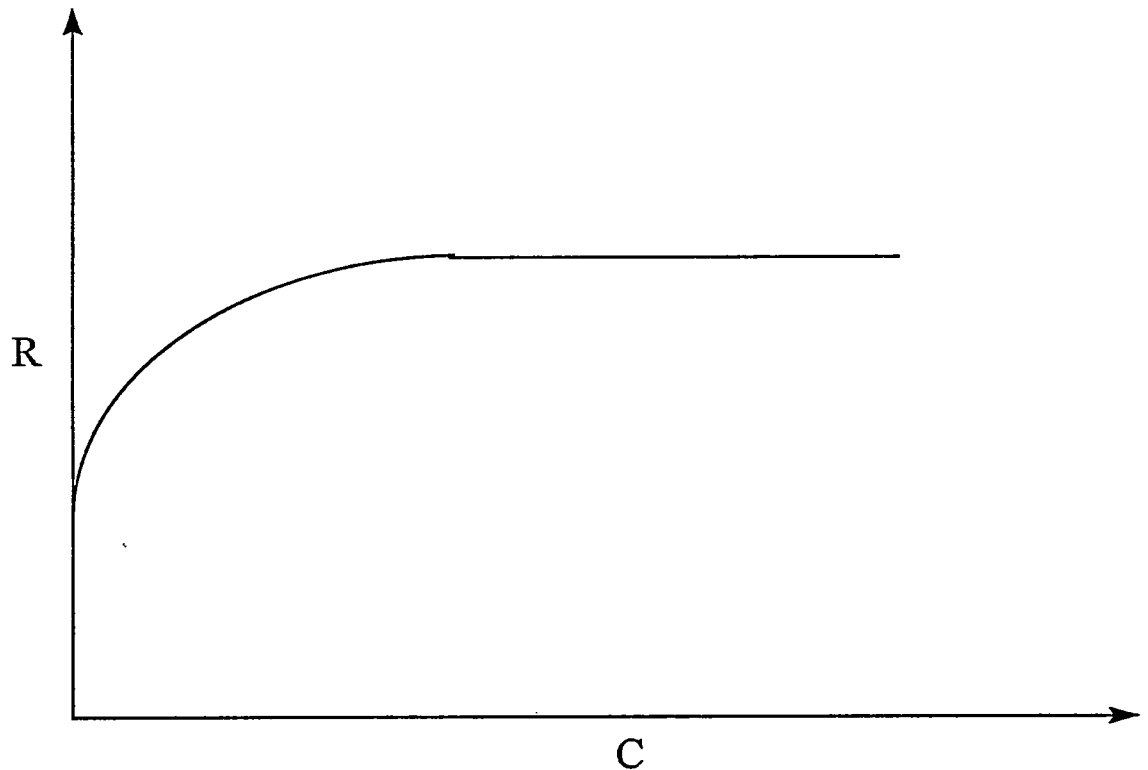


Figure 2.3 Illustration of R-curve Behaviour Showing Rising Fracture Toughness as a Function of Crack Length

A number of different techniques can be used to produce IPC materials. The most common are liquid metal infiltration of a ceramic preform (Prielipp et al., 1995), directional metal oxidation (DIMOX) (Pickard et al., 1992), solid state decomposition reactions (Henager and Brimhall, 1993), and cosintering (Sarafinchan, 1995). Each technique has benefits and problems.

2.3.1 Liquid Metal Infiltration

Liquid metal infiltration of a porous ceramic preform is a simple technique in concept, but can be challenging to do in practice. The ceramic preform is generated first using standard techniques, but it is not sintered to density; rather it is left with open connected channels of porosity. Different techniques can be used to modify the nature of the porosity in order to tailor the final microstructure. The liquid metal is then infiltrated using either natural capillary forces or gas pressure. If the ceramic and metal form a wetting system, the former technique can be used; if not, the latter is required. Difficulties can arise if closed porosity is present in the preform, or if gas bubbles become trapped behind an uneven liquid metal front. Both of these situations will lead to residual porosity in the final product. The nature of the interface between metal and ceramic depends on the wetting of the two materials and on the presence of possible reactive products or new phases formed during the processing. These can be used to tailor the strength of the interface which can have beneficial effects on the mechanical properties (Knechtel et al., 1991).

2.3.2 Directional Metal Oxidation

The DIMOX process involves the slow oxidation of a molten metal in a surface reaction. As the oxide layer is formed, small channels remain behind that allow the molten metal to wick up to the surface to continue the reaction. If the

temperature and the reaction kinetics are controlled properly, the reaction will proceed smoothly until all the metal has been drawn into the growing oxide to fuel the surface reaction. At this point the reaction is halted and the temperature lowered to solidify the residual metal in the channels. The resulting microstructure is an IPC. An alternate technique uses a porous silicon carbide preform to act as a further reinforcing phase for the system. In all cases the reaction must be well controlled, and the only composites that can be made involve a metal and its oxide. The process has been developed commercially by the Lanxide corporation (Newkirk et al., 1986) and is not available for general use in industry.

2.3.3 Solid State Decomposition

Solid state decomposition reactions involve an in situ oxidation reduction reaction that results in the desired products. An example of this process is the production of NiAl/Al₂O₃ composites from starting powders of NiO and NiAl (Henager and Brimhall, 1993). The reaction takes place during firing and results in a final product that is a mixture of NiAl, Ni₃Al, Ni, and Al₂O₃. The advantage of this procedure is the relative ease of processing, as simple milling of the powders to ensure adequate mixing is all that is required prior to hot pressing. The disadvantage is the mix of end products that results, although this can be adjusted by altering the ratios of precursor powders. In addition, this technique can only be used on a limited number of systems because it is entirely dependent on the transformation being thermodynamically favourable.

2.3.4 Cosintering

The final technique, and the one that was used to prepare the materials in this project, is cosintering. For this technique to work, the metal and ceramic powders must be able to sinter well under the same processing conditions. Both materials must have limited solubility in each other, and there should be no adverse reactions at the processing temperature. The powders must be well mixed to ensure homogeneity of the final product and then processed to produce the final sample for sintering or hot pressing. The sample is then consolidated and the two components sinter simultaneously to form interpenetrating networks. In order for interpenetrating networks to form, the phases should not coat each other or isolated particles will result. In addition, a minimum volume fraction of the reinforcing phase is required to ensure that a percolating network is formed throughout (Nan, 1993).

Many of the properties of IPC materials can be discussed in the language of percolation theory which gives a mathematical treatment of the nature of clusters within a sample (Stauffer and Ahonary, 1994).

2.4 Percolation Theory

In a three dimensional mixture of particles, there is a critical volume fraction above which particles of the same phase will be in contact with each other. This threshold depends on the nature of the lattice, the ratio of the particle sizes and the geometry of the particles. The basic theory can be illustrated by observing the size of clusters in a two dimensional lattice (Stauffer and Ahonary, 1994). Two types of percolation, bond and site percolation, can be postulated. In site percolation, a lattice of some form (square, honeycomb, etc.) is assumed, and sites on the lattice are randomly assigned to be either full or empty. Adjacent sites that are both full are considered to belong to the same cluster, and it is found that the average size of the clusters increase with the fraction of filled sites until a divergent point is reached and an infinite cluster is formed. This point is known as the percolation threshold. Above this point, there will always be an infinite cluster if the sites are filled in a random fashion.

Bond percolation works in a somewhat different manner, in that all of the sites in the lattice are assumed to be filled at the start, but not all sites are connected. In this scenario, each bond between adjacent sites has a certain probability of being present. If the bond is present, then the two particles it joins are considered to be in the same cluster, and the analysis proceeds as with site percolation.

Bond and site percolation do not have the same percolation thresholds on the same lattices. Table 2.1 shows calculated thresholds for a number of different two and three dimensional lattices.

Table 2.1 Site and Bond Percolation Thresholds for Different Lattices
(Stauffer and Ahonary, 1994)

Lattice	Site	Bond
Honeycomb	0.6962	0.65271
Square	0.59275	0.500
Triangular	0.500	0.34729
Diamond	0.428	0.388
Simple Cubic	0.3117	0.2492
BCC	0.245	0.1785
FCC	0.198	0.119

Figure 2.4 illustrates the concept of an infinite cluster for site percolation with an occupation probability of 60%. Note that this is just above the percolation threshold for site percolation on a square lattice.

The mathematical treatment of three dimensional lattices is much more complex, however the general principles discussed above still apply. In a random IPC with roughly equal sized regions of each phase, the material will exhibit bond percolation with a percolation threshold that is roughly an average of all the possible three dimensional lattice percolation thresholds. The exact value cannot be calculated analytically, but numerical solutions predict percolation thresholds of 15-17% (Nan, 1993). As mentioned earlier, a number of factors can influence the

exact value of the percolation threshold in a particular composite. Two of the most important are aspect ratio and particle size ratio.

High aspect ratios lead to an increased possibility of percolation because each particle has a much larger excluded volume. Excluded volume is that volume around a particle that the center of a similar particle could not be within unless there is overlap. An illustration of the excluded area of a number of two dimensional figures is shown in Figure 2.5.

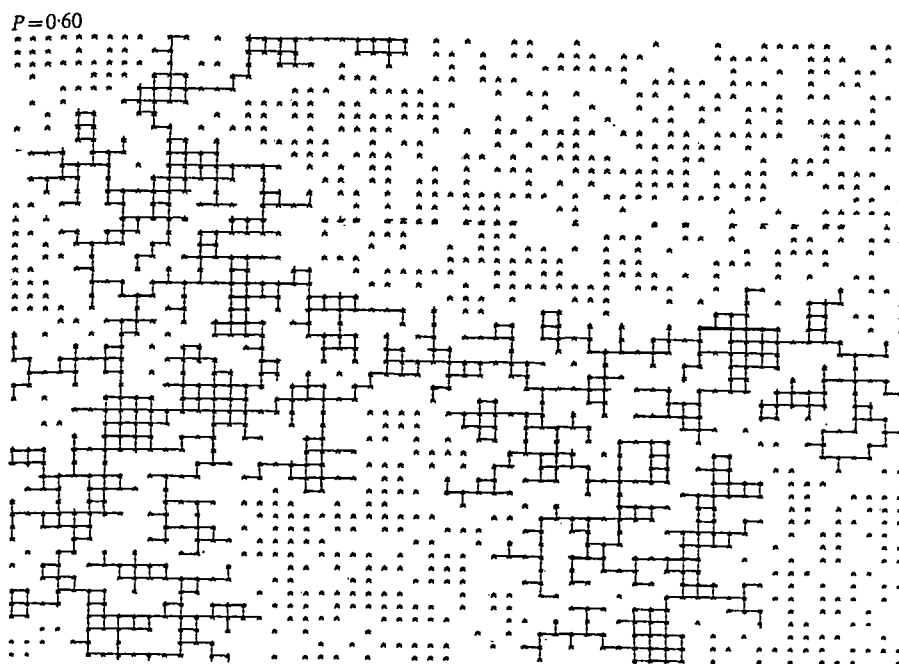


Figure 2.4 Square Lattice with the Probability of Each Site Being Occupied Being 0.6 Illustrating the Presence of an Infinite Cluster

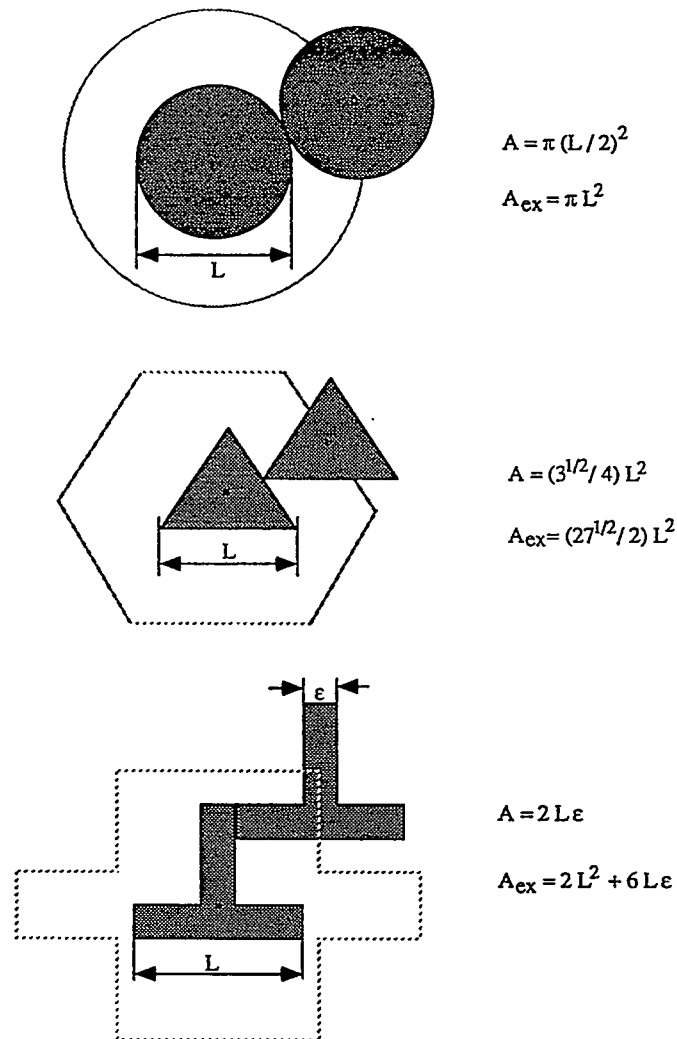


Figure 2.5 Illustration of Excluded Volume Around 2D Objects
(Nan, 1993)

The result of a large excluded volume is an increased probability of contact, and hence a lower threshold for bond percolation.

The size ratio of the starting particles is also important because of the possibility of small particles filling the gaps between large particles. If the smaller particles are the minor phase in the composite material, they can fill in the spaces

between abutting large particles of the major phase. This leads to a non-random distribution, and a higher probability of forming a connecting network, and hence a lower percolation threshold. Conversely, if the small particles are the major phase in the composite, it is highly unlikely that the minor phase will be able to form a network because the large particles could be fully coated by the smaller particles and will thus have fewer possibilities for forming bonds. This would lead to a relatively high percolation threshold for the large particle phase. The net result of a difference in size of the particles in the two phases would be a lower percolation threshold for the small particle phase, and a higher percolation threshold for the large particle phase.

Figure 2.6 illustrates a theoretical calculation of percolation threshold in a composite as the relative particle size ratio increases.

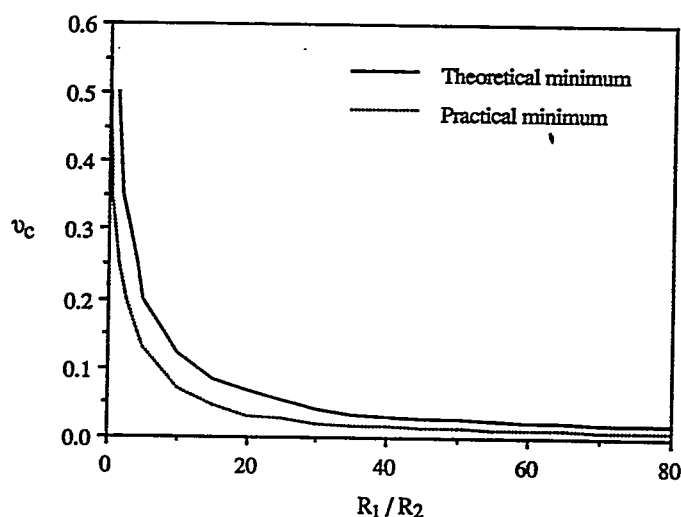


Figure 2.6 Percolation Threshold Dependence on Particle Size Ratio (Nan, 1993)

2.5 Mechanical Properties

There is relatively little information available in the literature on the mechanical properties of IPC materials. Most of the work published in this field has been done in a small number of labs, and only one laboratory has published work on a number of different types of composites with different volume fractions of reinforcing phases, and different processing techniques. No other research group appears to have explored the cosintering technique as no published papers have been found. The available data on the mechanical properties of IPCs are analyzed, and a number of theoretical predictions about IPC mechanical behaviour are discussed.

The initial part of the discussion deals with the properties of metals and ceramics in general. This is followed by a survey of models used to analyze conventional particulate and fibre reinforced composites. The difficulties these models may have in predicting the behaviour of IPCs, and current research and attempts to model IPCs are then reviewed.

2.5.1 Metals and Ceramics

Compared to metals, ceramic materials are characterized by high intrinsic or theoretical strength, high stiffness, low thermal expansion coefficients, and low fracture toughness (Kingery et al., 1976). Much of this behaviour can be understood by considering the nature of the bonding between atoms in metals and

ceramics. In a metal, bonding takes place through the delocalization of electrons throughout the crystal lattice and, as a result, is non-directional. In a ceramic, both covalent directional bonding, and ionic non-directional bonding occur. The result is a bonding force that is intrinsically higher in a ceramic than in a metal and leads to the higher modulus of elasticity and the lower coefficient of thermal expansion (CTE). A metal such as pure copper has a Young's modulus (E) of roughly 125 GPa and a CTE of $17.2 \times 10^{-6} / ^\circ\text{C}$, while alumina has a modulus of roughly 360 GPa and a CTE of $8.5 \times 10^{-6} / ^\circ\text{C}$ (C. M. S., 1994).

The deformation and fracture properties of metals and ceramics show even greater divergence. The theoretical strength of a material is of the order of $E/15$ (Ashby and Jones, 1991). However, in a pure metal the yield strength when there is an onset of plasticity is of the order of $E/1000$, and the ultimate tensile strength about $E/300$. Ceramics on the other hand exhibit plasticity only under special conditions. They can show nearly theoretical strength in compression but, in tension, show a wide range of strengths depending upon the nature of the microstructure. The primary cause of reduced strength in metals is the presence of dislocations and the interactions of dislocations within the microstructure, whereas in ceramics, the properties are strongly influenced by the presence of flaws.

A crack in any material acts as a stress concentration. In ceramics there are limited opportunities to relieve this stress through plastic deformation. As a result a large flaw can amplify a small applied stress to a level in excess of the material

strength and hence lead to failure. One model for the stress amplification of a crack was proposed by Griffith and gives the stress at a crack tip as:

$$\sigma_A = 2\sigma\sqrt{\frac{a}{\rho}} \quad [2.1]$$

where σ is the applied stress, a is the crack length and ρ is the radius of the crack tip (Anderson, 1991).

In ceramic materials, the lack of plasticity can lead to very sharp crack tips, and hence lead to a very high stress concentration. Metals typically do not experience these difficulties because crack tip plasticity is able to relieve the stress concentrations by blunting the crack tip.

The ability of a material to resist cracking can be summarized in a material parameter known as the fracture toughness, K_{IC} . The classic Griffith equation (1920) for the strength of a material is:

$$\sigma_f = \frac{K_{IC}}{Y\sqrt{\pi c}} \quad [2.2]$$

where σ_f is the fracture strength, Y is a parameter that characterizes the shape of the flaw, and c is the length of the critical flaw in the material.

This critical flaw can be either a crack or pore in the material, or in the case of a fully dense ceramic, will be the roughly the same as the grain size because of crystallographic effects (Tuan et al., 1994). If grains with different orientations relative to the applied stress have anisotropic elastic properties, stress concentrations can open up cracks at grain boundaries and triple junctions.

2.5.1.1 Ductile Fracture in Metals

The process of ductile fracture follows three steps (Le Roy et al., 1981). Voids nucleate on second phase particles within the metal, the voids then grow and finally link up to cause fracture. The three steps are distinct and each will only occur under specific conditions.

It is generally assumed that some threshold strain is required for the nucleation of the voids to occur (Argon et al., 1975). This nucleation strain will provide the stress for either the fracture of the particle matrix interface, or fracture of the second phase particle itself. The stress required for this is difficult to model because it is a local stress condition that depends on the shape and size of the particle as well as on the nature of the surrounding matrix. Experimental evidence (Le Roy et al., 1981) however, indicates that there are often two populations of second phase particles present within any material.

The first population comprises particles that will nucleate a void at zero strain. These particles may have particularly weak interfaces, or may be elongated along the tensile axis and thus experience more load transfer which will lead to early failure. The voids from these particles will be present throughout the elongation of the sample.

The second population comprises particles that require a nucleation strain of some kind in order to produce a void. These particles will produce additional

voids throughout the elongation of the sample as new particles meet the local stress conditions to cause interfacial or particle fracture.

After nucleation, the void will grow as additional strain is imposed on the material. The rate of growth will depend on the strain rate applied to the specimen and on the stress state (Rice and Tracey, 1969).

Upon reaching some critical size, the voids will link and form larger voids. When this occurs across an entire plane in a sample, the sample has fractured in a ductile manner. The exact condition for this linkage to occur depends on the geometry and distribution of voids, and hence on the distribution of second phase particles within the material. It has been postulated that the condition for linkage to occur is when the longest axis of the void, usually parallel to the tensile axis, is of the order of the planar nearest neighbour void spacing (Le Roy et al., 1981).

The nucleation strain can be calculated by plotting the volume fraction of voids against the local strain within a sample and extrapolating back to zero strain. This usually would involve the sample developing a neck, and hence having different areas with different local strains. Development of a neck complicates analysis because the stress state within a necked region can include a significant hydrostatic component that can modify the nature of the damage processes. In general, a compressive hydrostatic stress component can suppress damage by reducing the stress at the particle matrix interface and hence delaying the void nucleation; and reducing the growth rate. A tensile stress component can enhance the development of damage in the opposite way.

2.5.2 Behaviour of Metals and Ceramics in Composites

Metals and ceramics within a composite material have the same basic characteristics as the individual materials. However, differences arise as a result of the presence of two or more phases. Thermal expansion mismatch, strain induced dislocations, different elastic moduli and the effects of constraint all influence the properties of the materials within a composite.

2.5.2.1 Thermal Expansion Mismatch

If a composite comprised of two phases with different thermal expansion coefficients is cooled from the fabrication temperature, each of the phases will attempt to contract by differing amounts. If the interface does not fracture, both materials will strain by the same amount. Assuming that plastic deformation does not occur, this will lead to a residual stress in the composite. Typically, because a metal has a higher CTE than a ceramic, the stress will be tensile in the metal and compressive in the ceramic (Fig 2.7).

2.5.2.2 Strain Induced Dislocations

If the stresses in the metal phase exceed the yield strength of the material, the metal will strain plastically and move and generate dislocations. This can lead to work hardening of the metal. Equation 2.3 shows the increase in shear stress

(τ) required to move a dislocation through a uniformly spaced forest of dislocations with density ρ :

$$\tau = \alpha Gb\sqrt{\rho} \quad [2.3]$$

where, α is a constant between 0.5 and 1, depending on the specifics of the model, G is the shear modulus, and b is the Burgers vector of the dislocation.

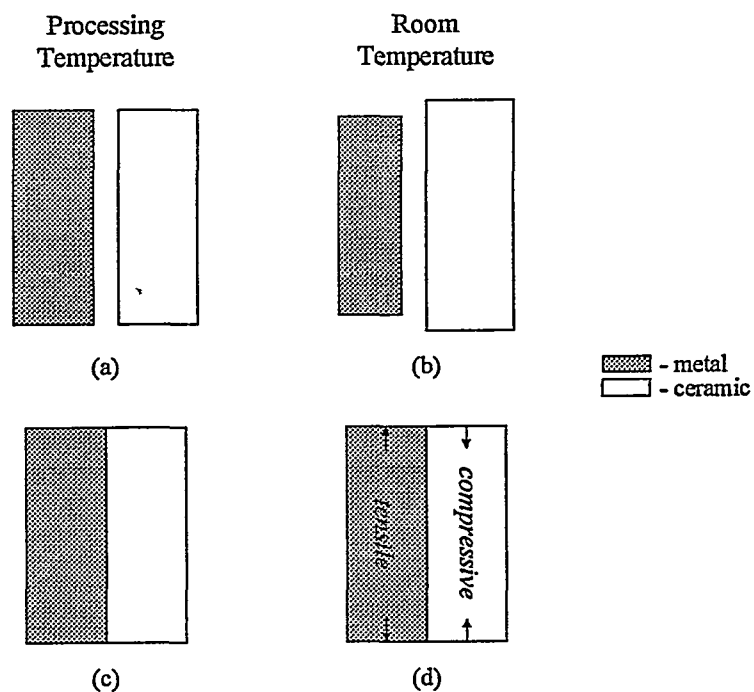


Figure 2.7 Stresses in Metal and Ceramic Portions of Composite

The density of dislocations in a particulate reinforced metal matrix composite has been modeled by Miller and Humphries (1990) by assuming that all of the residual stress is relieved by plastic flow:

$$\rho = 12(\Delta T)(\Delta CTE) \frac{V_p}{bd} \quad [2.4]$$

where V_p is the volume fraction of ceramic particles, d is the diameter of the particles, ΔT is the difference between the processing temperature and room temperature, and ΔCTE is the difference in coefficient of thermal expansion of the two materials.

Equation 2.4 gives an estimate of the number of dislocation lines intersecting a plane of unit area within the sample. Since plasticity in the matrix would in actuality only occur until the residual stress is approximately equal to the yield stress, this estimate will provide an upper limit for the dislocation density.

2.5.2.3 Elastic Moduli

The presence of materials with different elastic moduli within the same composite material can lead to non-uniform stresses in a sample. If a uniform stress is applied to a metal sample and a ceramic sample, the ceramic sample will exhibit a much smaller strain as a result of its higher tensile modulus. The corollary of this is that a much higher stress is required to strain a ceramic to the same extent as a metal. The net result in a metal-ceramic composite is that much more of an applied load is borne by the ceramic phase. The Voigt model (Clyne

and Withers, 1993) for elastic stiffness predicts that the overall elastic modulus of a composite, E_{3C} , is:

$$E_{3C} = (1-f)E_M + fE_I \quad [2.5]$$

where f is the volume fraction of ceramic, and E_M and E_I are the Young's moduli of the metal and the ceramic respectively. Thus the strain of the composite for an applied stress of σ_a would be:

$$\varepsilon = \sigma_a/E_{3C} \quad [2.6]$$

where ε is the strain of the whole composite.

Working back to find the stresses in the individual components yields:

$$\sigma_M = \sigma_a \frac{E_M}{(1-f)E_M + fE_I} \quad [2.7a]$$

and

$$\sigma_I = \sigma_a \frac{E_I}{(1-f)E_M + fE_I} \quad [2.7b]$$

This indicates that the material with the highest modulus will be under more stress.

2.5.2.4 Constraint

The final effect discussed is that of constraint. Essentially, constraint means that each phase is surrounded by regions of a distinctly different phase with different properties. Therefore, during processing, grains in one phase can only grow until they reach a size that is comparable with the mean phase intercept length. For a composite with a very fine scale microstructure, this can lead to a

material with very small grains, which in turn can lead to improved material properties. In a ceramic for example, the tensile strength is critically dependent on the maximum flaw size in the specimen. In a fully dense material, the maximum flaw size is comparable to the grain size, hence a finer grain size results in a stronger material. In a metal, the grain size of the material has a strengthening effect described by the Hall-Petch equation (Hull and Bacon, 1992):

$$\sigma_y = \sigma_o + k_y d^{-n} \quad [2.9]$$

where σ_y is the yield strength, σ_o is a constant stress arising from intrinsic lattice resistance, k_y is a material constant, n is approximately 0.5, and d is the average grain size. Back stresses from dislocation pile-ups at grain boundaries can shut down dislocation sources, preventing the generation of new dislocations. Smaller grains allow pileups to form more rapidly and consequently the production of new dislocations stops sooner.

Another issue related to composites is the effect of constraint on the stress state of the metal. Ashby et al. (1989) found that a highly constrained metal wire can have a flow stress higher than an unconstrained wire by as much as an order of magnitude. The ductility of the constrained metal was dramatically decreased however, and the overall benefit of the reinforcement was less than for a metal phase that was only weakly bonded to the ceramic matrix. The reason proposed for the changes in the behaviour of the metal was the increasing triaxial nature of the stress state as the metal was increasingly constrained. This finding has serious

implications for IPC materials where, for purposes of fracture resistance, it may be preferable to have a composite exhibiting weak metal-ceramic interfaces than to have one with very strong interfaces.

Knechtel et al. (1994) investigated the flexural strength and fracture toughness of aluminum/alumina composites which have strong interfaces, and aluminum copper composites which have weak interfaces. The copper composites showed slightly lower fracture toughness (6.2 vs. 7.4 MPa \sqrt{m}), and somewhat lower flexural strength (303 MPa vs. 506 MPa). These results indicate that a weak interface has little impact on the fracture toughness, but has deleterious effects on the overall flexural strength.

2.5.3 Metal Ceramic Interfaces

The free energy per unit area of an interface, γ , is the fundamental thermodynamic property of an interface. The work of adhesion, W_{ad} , which is the work that must be done to separate an interface, can be calculated from the Dupre equation as:

$$W_{ad} = \gamma_m + \gamma_c - \gamma \quad [2.10]$$

where γ_m and γ_c are the surface energies of the metal and the ceramic respectively. Much of the attractive force at the interface arises through coulombic image forces generated within the metal by ions near the ceramic surface (Finnis et al., 1990).

This is balanced by a repulsive force between the ions at the surface resulting from overlap of their electron shells.

Another possible interaction at an interface is the formation of a new phase at the interface, possibly either an intermetallic or an oxide. In this case, there are usually two interfaces, one between the new phase and the metal, and one between the new phase and the ceramic. The interfacial properties will tend to be dominated by the weaker of these two interfaces (Ruhle, 1996).

2.5.4 Metal Ceramic Composites

The behaviour of a composite can be examined on a number of different microstructural scales. Atomistic effects and the interactions of individual dislocations within the material fall under the realm of micromechanics. At the other end of the spectrum, macromechanical models have been developed that assign average material properties without considering the individual processes that generate the properties. This enables analysis of larger scale structures, such as fibre reinforcements, to be done without becoming mired in details.

The characteristics of a micromechanical model are that the strengthening effect is a scale dependent phenomenon, the reinforcing phase does not bear load, and the reinforcement acts as a barrier to dislocation motion. The Orowan strengthening mechanism is an example of such a process (Meyers and Chawla, 1984). It predicts that the additional shear stress required to bow a dislocation out to a semicircle between two hard reinforcing particles (Fig 2.8) is:

$$\Delta\sigma = \frac{Gb}{l} \quad [2.11]$$

where G is the shear modulus, b is the Burgers vector of the dislocation and l is the particle spacing of the reinforcing phase.

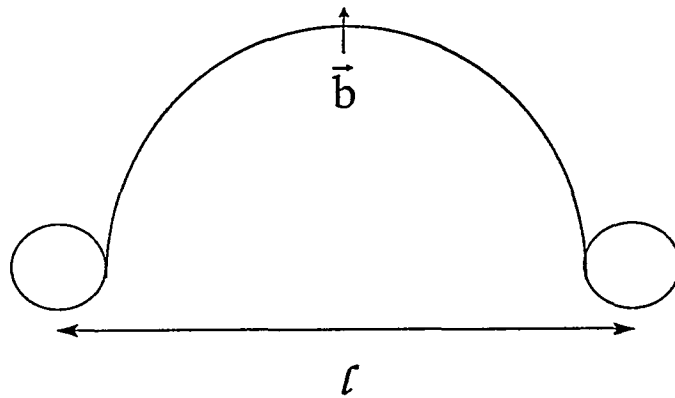


Figure 2.8 Critical Condition for Orowan Strengthening

As the spacing of the particles becomes finer, the shear stress increases, which shows the scale dependence of the model. As the size of the particle is unimportant in this treatment, the model also indicates that, for the same volume fraction, a large number of small particles will provide greater strengthening than a few large ones.

In macromechanical models, effects like Orowan strengthening are incorporated into average material properties for different phases within the composite. The properties of the composite are then determined by the distributions of stresses and strains within the material, which are further determined by the component material properties as well as geometrical considerations. Very simplistic models derived from the rule of mixtures indicate that stresses and strains are partitioned between phases simply in accordance with their volume fractions (Clyne and Withers, 1993). Two situations arise from this so called slab model. The situation illustrated in Figure 2.9a shows a parallel arrangement where each phase will be subject to the same strain. This is the Voigt model of a composite and leads to a partitioning of stress between the two phases. This is summarized in equation 2.12.

$$\sigma_c = \sum f_i \sigma_i \quad [2.12]$$

In Figure 2.9b, the phases are in series with each other, and each phase is assumed to experience the same stress. This leads to strain partitioning where the compliant layer will deform to a much greater extent than the stiff layer. This behaviour can be summarized by equation 2.13

$$\frac{1}{\varepsilon_c} = \sum \frac{1}{f_i \varepsilon_i} \quad [2.13]$$

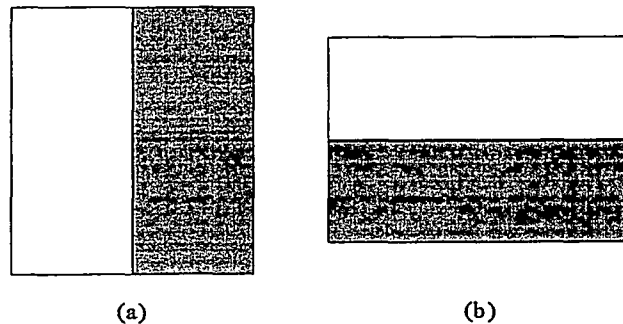


Figure 2.9 a and b. Parallel and Series Representations of Phases in a Composite Material

More sophisticated models of composite behaviour have been developed to model the effects of metal phases subjected to loads higher than their yield strength, and to determine the stress and strain fields around the ends of fibres (Fukada and Chow, 1981). The modeling done in this field is mostly numerical since analytical solutions can only be developed for highly simplified cases (Fig 2.10).

2.5.5 Interpenetrating Phase Composites

A brief discussion of some models of IPC deformation will be followed by a summary of the data available in the current literature on the mechanical properties of IPCs.

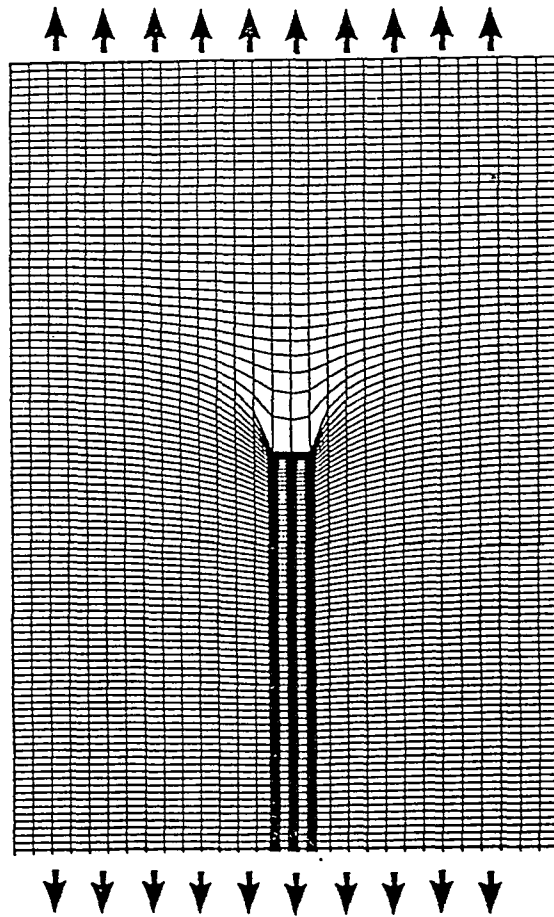


Figure 2.10 Finite Difference Model of Discontinuous Fibre with Imposed Far Field Matrix Strain (Clyne and Withers, 1993)

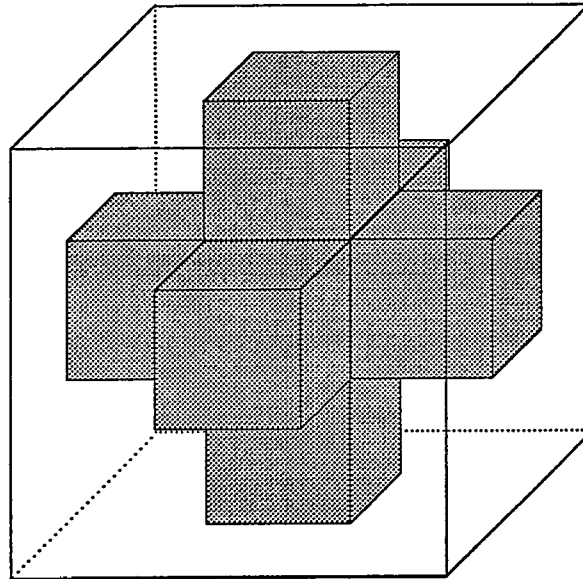


Figure 2.11 Unit Cell in Ravichandran Model (Ravichandran, 1994)

2.5.5.1 Modeling of IPCs

Very little has been done in the way of modeling the deformation behaviour of IPC materials. One simple model developed by Ravichandran (1994) treats the composites as comprising a number of identical unit cells and has had some success in predicting the behaviour of IPCs when compared with finite element models. The model considers unit cells such as the one illustrated in Figure 2.11.

A prediction of the stress strain behaviour is accomplished by looking at the net effect of an applied stress on the various series and parallel elements within the unit cell. The equation:

$$\varepsilon_c = (1 - \alpha) \left(\frac{\sigma_3}{\kappa_m} \right)^{1/\eta_m} + \alpha \left(\frac{\sigma_3}{\kappa_f} \right)^{1/\eta_f} \quad [2.14]$$

where $\alpha = x/y$ and x and y are the side lengths of the small cubes and the large cubes respectively, κ and η are defined by the equation:

$$\sigma = \kappa (\varepsilon)^\eta \quad [2.15]$$

representing the plastic portion of the deformation, and the subscripts m and f refer to the matrix and the reinforcement respectively. The volume fraction of the reinforcing phase is related to the quantity α by the following expression:

$$V_f = \alpha^2 (3 - 2\alpha) \quad [2.16]$$

The quantity σ_3 is related to the applied stress in the composite through the equation:

$$\sigma_c = 2\sigma_3\alpha(1 - \alpha) + \kappa_f [A]^{\eta_f} \alpha^2 + \kappa_m [A]^{\eta_m} (1 - \alpha)^2 \quad [2.17]$$

where A is defined by the equation:

$$A = \left[(1 - \alpha) \left(\frac{\sigma_3}{\kappa_m} \right)^{1/\eta_m} + \alpha \left(\frac{\sigma_3}{\kappa_f} \right)^{1/\eta_f} \right] \quad [2.18]$$

The model has also been expanded to deal with the effect of constraint in the material. The predictions match well with FEM data in general, and also correspond closely with experimental data (Figs 2.12 and 2.13). Note that in these

figures, the references to Eqns. 25 and 26 correspond to the Equations 2.17 and 2.18 in this text.

The most rigorous technique typically utilized for the analysis of metal matrix composite materials, the Self Consistent Effective Medium Approach is not particularly applicable to IPCs for a number of reasons. Firstly, it treats stresses and strains within each component as uniform, whereas FEM analysis indicates that this is not in fact the case. Secondly, the reinforcing material is always considered as a particle to be incorporated into the matrix, and this does not account for the connectivity seen in an IPC.

A model has also been proposed by Duxbury et al. (1987) that considers the fracture behaviour of a percolating network in terms of a set of resistors or fuses. The model investigates the nature of load shedding and stress concentration resulting from crack growth in a material using an electrical analog.

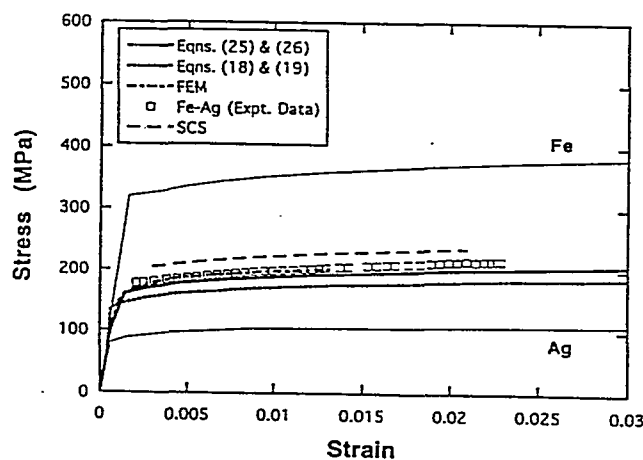


Figure 2.12 Stress Strain Behaviour and Predictions for Silver Iron System (Ravichandran, 1994)

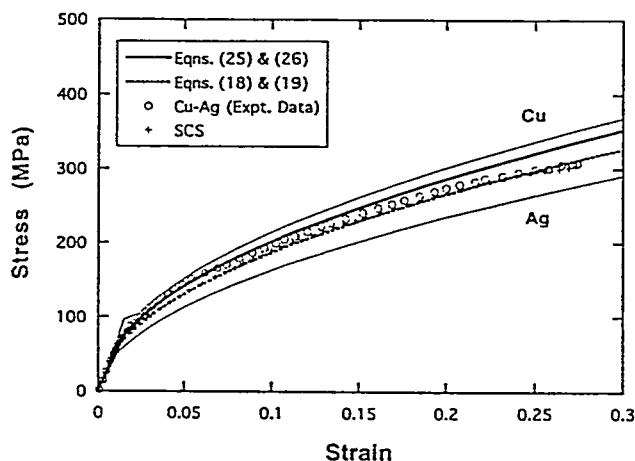


Figure 2.13 Stress Strain Behaviour and Predictions for Copper Silver System (Ravichandran, 1994)

2.5.5.2 Experimental Data on IPCs

Information that has been gathered on the properties of aluminum/alumina composites (Prielipp et al., 1995; Knechtel et al., 1994; Skirl et al., 1997) illustrates some of the trends in the mechanical properties of IPCs. The strength and fracture toughness of the composite materials were both found to increase as the volume fraction of aluminum was increased. This is illustrated in Figure 2.14 which shows the properties of the materials for volume fractions up to 40% aluminum.

This is noteworthy because, typically, any adjustment to the microstructure that increases the strength of a material decreases the fracture toughness and vice

versa. The scale of the reinforcing phase also has an effect on the material strength as determined by Prielipp et al (1995). They found that there was an optimum size of approximately 0.5 μm for the metal reinforcing phase in order to give the highest strength. The fracture toughness was found to increase with increasing ligament size up to the largest ligaments tested, approximately 1 μm in diameter. The reduction in strength was explained by the loss of constraint in the metal phase as the ligament size was increased. The same trends were observed in composites that were infiltrated with copper instead of aluminum (Knechtel et al., 1994).

Investigators have concentrated to this point on composites with the ceramic as the major phase and have not investigated metal rich compositions.

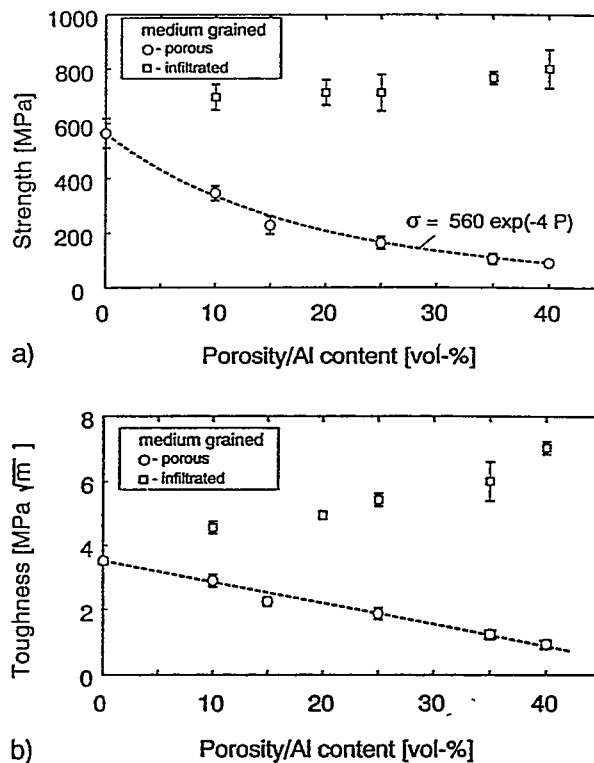


Figure 2.14 Strength and Toughness Variation with Volume Fraction of Aluminum in Composite (Prielipp et al., 1995)

CHAPTER 3

PROCESSING

The processing techniques used to prepare the materials for this research were developed primarily by Sarafinchan and are discussed at length in his M. Eng. thesis (1995). The main features of the processing are outlined in the following sections, and include specifications of the raw materials and the processing regimes used to prepare the final composites. Difficulties that were encountered during the preparation of the materials, and the steps taken to overcome them are also discussed.

The samples used in these experiments were produced from powders by tape casting followed by lamination, burnout, reduction and finally hot pressing. Each stage in the process is described in further detail.

3.1 Raw Materials

Each of the composites was fabricated from a blend of nickel and yttria stabilized zirconia powders. These materials were selected for their purity and availability at the desired particle size ranges. Samples with zirconia volume fractions of 0%, 5%, 10%, 15%, 20%, 25% and 100% were prepared for investigation.

INCO type 123 nickel powder with a median particle size of 6.80 μm and a standard deviation of 5.4 μm was used. Type 123 powder is fabricated using a nickel carbonyl decomposition process which is described by Bale and Chapman (1986). The zirconia powder was TOSOH type TZ8Y with an average particle size of 0.18 μm and a specific surface area of 15.7 m^2/g . The HORIBA Particle Size Distribution Analyzer and the Quantachrome Autosorb-1 instruments in the Ontario Centre for Materials Research (OCMR) powder processing laboratory at McMaster University were used to determine the particle sizes and surface areas of the powders.

Table 3.1 Powder Compositions

INCO 123 NICKEL POWDER		TZ8Y POWDER	
Element	wt%	Element	wt%
Ni	99.3	Y ₂ O ₃	13.26
S	<1 ppm	Al ₂ O ₃	<0.005
C	0.08	SiO ₂	0.006
Al	0.09	Fe ₂ O ₃	<0.002
Si	0.02	Na ₂ O	0.057
Cl	0.006	ZrO ₂	86.67
Cu	0.22		
Mn	0.03		
Fe	< 50 ppm		
Co	0.09		

The powder compositions were analyzed in the geology department at McMaster University by x-ray fluorescence. The results, given in Table 3.1, show

the presence of the yttria stabilizer in the zirconia powder and that the most abundant impurity in the nickel powder was copper.

In previous studies (Sarafinchan, 1995), Sherritt ONF grade nickel powder was used. This material was found to produce unusually high strength and low ductility in the final samples. The decision to switch to INCO type 123 nickel powder was made primarily to avoid these problems. The purity of the type 123 material is higher than the ONF, although the particle size is somewhat larger. The zirconia powder used was the same as that used by Sarafinchan (1995) as no difficulties had been encountered with it in previous experiments.

3.2 Tape Casting and Lamination

A slurry for tape casting was prepared by first mixing the required volume fractions of the 123 and TZ8Y powders with the dispersant and solvent and then milling them with zirconia milling media. This was followed by the addition of plasticizers and binders and further milling.

All of the slurry preparation was carried out in polyethelene bottles. The solvent used was an azeotropic mixture of ethanol (EtOH) and trichloroethylene (TCE) with a volume ratio of 28 EtOH to 72 TCE. Emphos PS-21A, a low molecular weight phosphate ester, was used as the dispersant. The milling material was TOSOHO YTZ High Wear Resistant Zirconia Grinding Media, 5 mm in diameter. The initial milling was carried out for approximately 24 hours to disperse the powders and break up soft agglomerates.

After completion of the first milling stage, plasticizers and binders were added to the slurry. The plasticizers used were polyethylene glycol and dioctyl phthalate, and the binder used was polyvinyl butryal. The second stage of milling was carried out for approximately six hours to ensure a uniform dispersal of the plasticizers and binder within the slurry.

Immediately prior to tape casting, the slurry was vacuum degassed for approximately two minutes to remove dissolved air and reduce the possibility of bubble formation within the tape. The slurry was then poured into the reservoir of the tape caster and the tape was cast at a rate of approximately 1-2 cm/s. The heights of the first and second doctor blades were set at 400 μm and 350 μm respectively. The tape was then allowed to dry for at least three hours. If the tape was left for more than 24 hours, however, it was very difficult to remove from the glass. After the tapes were removed from the glass, they could be handled with relative ease and could be stored for several weeks before further processing.

The volume fractions of each chemical in the slurry are included in Table 3.2. The required ratios of slurry components were determined by Sarafinchan (1995) for both zirconia and ONF nickel powder. Initial experiments found the same ratios to be suitable for the type 123 nickel powder used in this work.

The first attempts at producing zirconia tapes resulted in tapes that were very brittle and that cracked while drying. To eliminate this problem, the levels of plasticizers were increased slightly and the slurry was milled more thoroughly

Table 3.2 Compositions of Slurries

Percent Zirconia	Slurry Component grams per 10 cm ³ of powder						
	Nickel	Zirconia	Solvent	Phosphate Esters	Polyvinyl butryl	Polyethylene Glycol	Diocetyl Pthalate
0	89.0	0	58.4	0.47	3.9	2.36	2.02
5	84.6	3.0	57.8	0.49	3.85	2.4	2.07
10	80.1	6.0	57.2	0.50	3.8	2.43	2.11
15	75.6	9.0	56.6	0.52	3.73	2.47	2.14
20	71.2	12.0	56.0	0.54	3.67	2.51	2.17
25	66.8	15.0	55.4	0.57	3.75	2.53	2.21
100	0	60.0	46.5	0.70	2.90	3.13	2.79

Some of the composite tapes displayed segregation of the nickel and zirconia. The smaller zirconia particles tended to sediment more slowly than the large nickel particles, which resulted in a zirconia rich top surface and a nickel rich bottom surface in the dry tape. This problem could usually be avoided by producing the tape as quickly as possible after the milling stage was complete. The 25 percent zirconia tape showed the worst segregation, and despite a number of attempts the difficulties were not entirely resolved. This segregation can be seen in the layered pattern in the micrograph of Figure 5.6b.

Typical final tape thicknesses are summarized in Table 3.3. The tapes tended to get thinner as the zirconia content increased, with the pure zirconia tape

being significantly thinner than any other grade as a result of greater shrinkage during the drying process. This influenced the number of tapes required for later sample preparation.

Table 3.3 Typical Thickness of Dried Tapes

Composition (% ZrO ₂)	Thickness (μm)
0	270±10
5	280±10
10	260±10
15	260±10
20	240±10
25	230±10
100	120±20

3.2.1 Lamination

Samples of each composition were prepared by punching discs 2.54 cm or 5.08 cm in diameter from the tape and laminating them by pressing them together in a hot metal die. Approximately 30 such discs were used to prepare each of the composite samples and the pure nickel samples. The final thickness of the laminate ranged from 7-9 mm. As the pure zirconia tapes exhibited greater shrinkage while drying, it was necessary to use approximately 50 discs to generate a sample 5-7 mm thick.

The tapes were pressed for at least 30 minutes at a pressure of 40 MPa in a die that had been pre-warmed to 130°C. The hydraulic press was outside the furnace, therefore the temperature of the die dropped gradually throughout the lamination process.

Figure 3.1 shows the arrangement of the die components. The die and pistons were made of steel. The die had a brass insert with an inside diameter of 5.08 cm. A teflon spacer was inserted between each piston and the sample, and a single disc of tracing paper was placed between the teflon spacer and the sample. The spacers and tracing paper were inserted to ensure that the sample did not adhere to the faces of the pistons and thus prevented damage to the laminate when it was removed from the die.

Throughout the lamination procedure, the die was connected to a vacuum pump that removed any organic liquids squeezed out of the sample.

3.3 Organic Burnout and Reduction

After the samples had been laminated, they were prepared for hot pressing by removing the organic materials and oxide coating. The burnout was carried out in an air furnace within a fume hood that collected the organic byproducts. The samples were placed on a bed of coarse alumina to avoid contamination and to help maintain a uniform temperature throughout. During this stage of processing the mass of the sample decreased by roughly 5%.

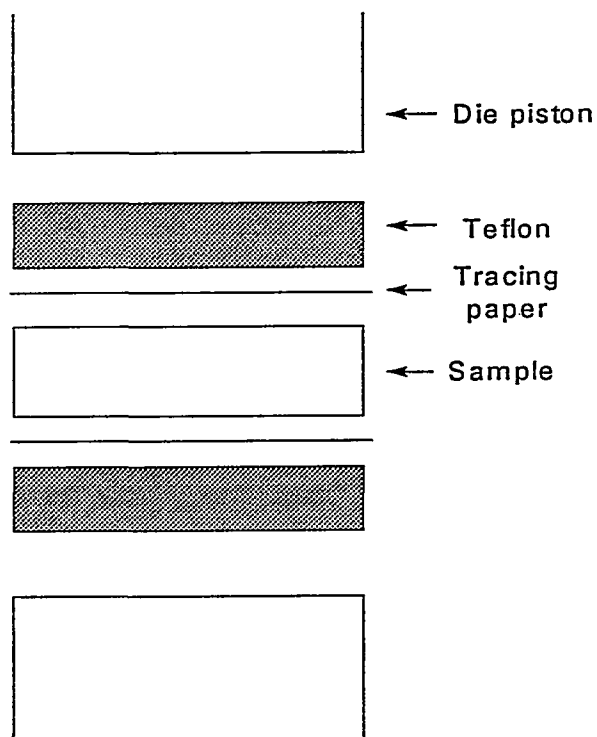


Figure 3.1 Illustration of Lamination Components

The organic materials had to be removed in air, because thermal decomposition would lead to residual carbon and phosphorus in the final product that would inhibit sintering kinetics and degrade the final properties of the material.

The burnout also required careful control to avoid excessive gas evolution that could form pores or cracks within the laminate. This was done by reducing the heating rate near the points of maximum gas evolution as determined by thermogravimetric analysis (TGA). The TGA curve for a 25% composite is shown in Figure 3.2. TGA analysis was conducted on the Netzsch Thermowaage STA

409 at the Brockhouse Institute for Materials Research. The exact temperature profile used for the burnout procedure is shown in Figure 3.3. For the pure zirconia the procedure was modified slightly by raising the final temperature plateau to 600°C. This was done because the pure zirconia required a higher sintering temperature in order to achieve enough mechanical strength to be handled.

The burnout process was also used to lightly sinter the material to give it some strength to allow it to be loaded into the hot pressing die. Excessive sintering had to be avoided, however, as it would have reduced the driving force during hot pressing and inhibited densification.

After the burnout was complete, the nickel powder had a surface film of nickel oxide. Several samples prepared did not achieve full density and it was discovered that the particles had a substantial nickel oxide film. To eliminate this problem, a reduction procedure was devised to reduce the nickel oxide back to nickel metal. The samples were placed inside a sealed tube furnace that could be either evacuated or could have a gas flow through it. The tube was sealed and then evacuated. It was then back filled with a gas comprising a mixture of 5% hydrogen in 95% argon. This procedure was repeated, and then the sample was

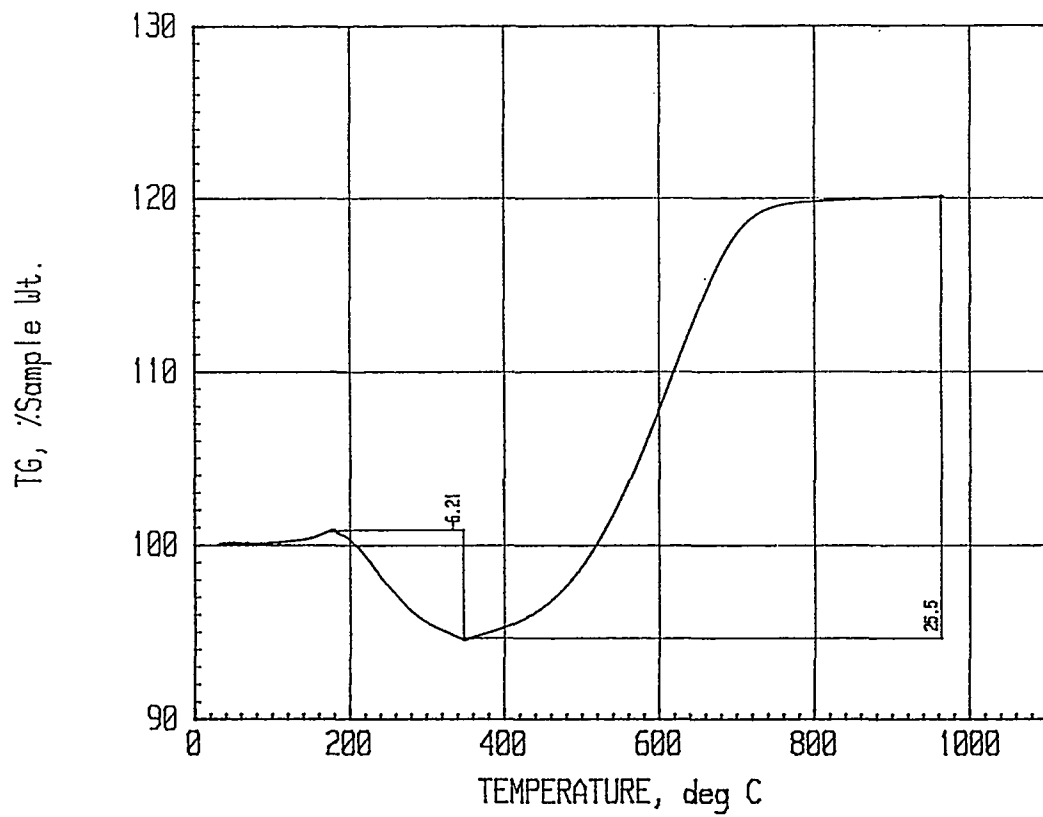


Figure 3.2 Thermogravimetric Analysis Curve for Burnout of 25% Composite in Air

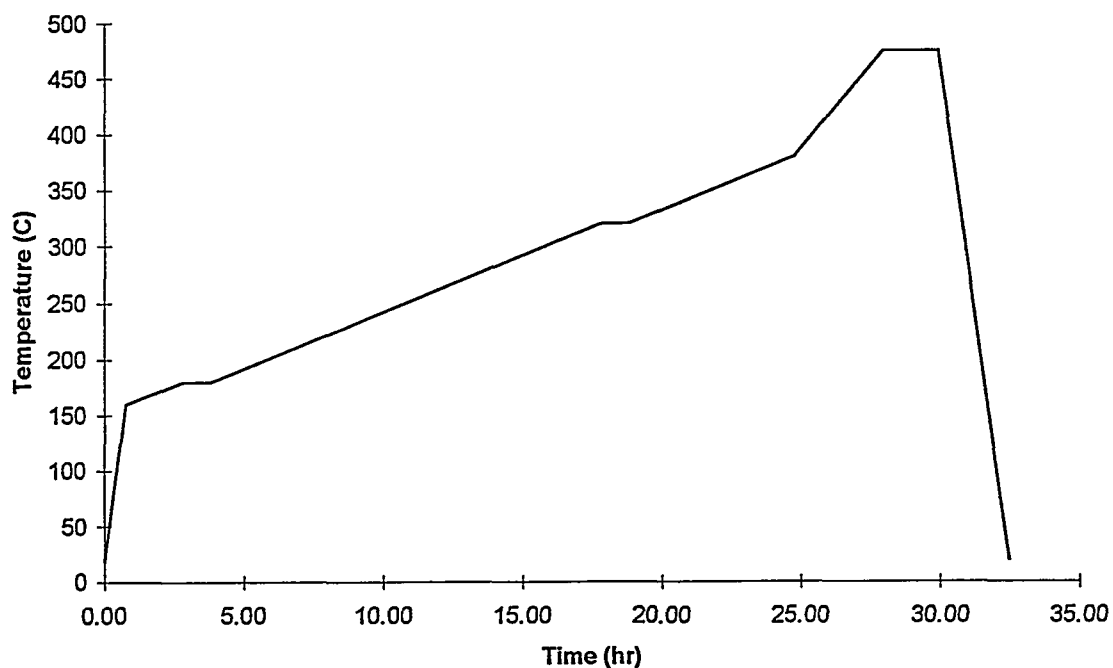


Figure 3.3 Burnout Profile for Laminated Discs

heated to 500°C and held in the flowing gas (5 L/min) for 12 to 18 hours. This procedure was found to reduce the nickel oxide film and allow densification to >98% of theoretical density. During the reduction process, the mass of the samples was reduced by an additional 5-8%. A TGA curve of the reduction of a burned out nickel sample is shown in Figure 3.4.

The burnout and reduction procedure was not carried out in one step for two reasons. Firstly, it was felt that controlling the partial pressures would be too difficult a task because of the nature of the experimental setup. Secondly, the

procedure was required to remove as much carbon and phosphorous as possible which was accomplished best by a burnout in the presence of oxygen. A CO₂/CO gas mixture was not selected as a reducing agent because under some conditions, the extremely toxic gas, nickel carbonyl, can form (INCO, 1996).

3.4 Hot pressing

The final step in the production of the nickel-zirconia composites was hot pressing to full density. This was carried out in the Electrofuel 50 ton hot press at the McMaster University OCMR Powder Processing Laboratory. The samples were loaded into a cylindrical die made from grade AQ26 graphite. A coating of boron nitride was applied to the inside of the die and to the contact surfaces of the pistons to act as both a lubricant and as a diffusion barrier to prevent carbon from infiltrating the sample. In addition, a thin sheet of graphite paper coated in boron nitride was inserted between the sample and the piston to help prevent bonding between them.

Each sample was pressed in a vacuum at 40 MPa for three hours. The pure nickel samples were pressed at 950°C in order to minimize grain growth, the composites were pressed at 1250°C, and the pure zirconia was pressed at 1300°C to ensure sintering of the zirconia. Densities were then measured using both the Archimedes fluid displacement method, and geometrically. By following these procedures all samples except the 5% composite attained densities greater than 98% of theoretical. The 5% composite reached a density of only 93.5% of

theoretical, which may explain the lower than expected strength in this grade of material.

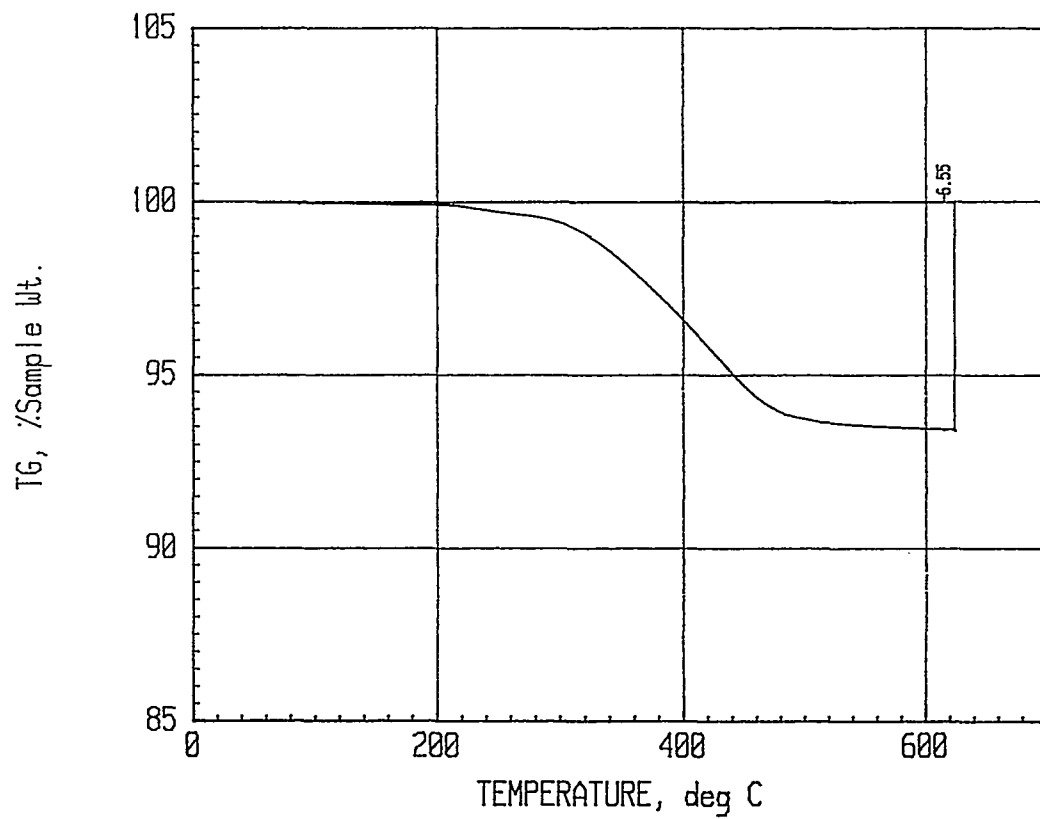


Figure 3.4 TGA curve of Nickel Sample in Reducing Atmosphere

CHAPTER 4

EXPERIMENTAL PROCEDURE

4.1 Tensile and Four Point Bend Specimen Preparation

Two inch diameter discs of each composite grade were prepared and sent to BOMAS Machine Specialties Ltd. for machining into tensile or four point bend specimens. The pure nickel samples were machined into samples with a gauge length of 22 mm with nominal dimensions of 2 mm \times 3.5 mm. All of the composite grades and the pure zirconia were machined into rectangular bars with nominal dimensions of 22 mm \times 2 mm \times 1.5 mm, with the lamination planes parallel to the 22 \times 2 mm face. After preliminary testing, it was determined that the 5%, 10% and 15% composite grades were too ductile for analysis by four point bend techniques, so tensile specimens were prepared from the bend bars with a gauge length of 14 mm and dimensions of 1.5 mm by 1.5 mm.

All of the tensile specimens were tested using the MTS model 810 mechanical testing system at McMaster University. Strain rates of 0.05 mm/s were used with the machine recording the applied load. Errors of ± 10 Newtons for the applied load were typical, and the system resolution was 0.007 mm. Four point bend tests were carried out on the Lloyds 6000R mechanical testing system using

the four point bend mechanism shown in Figure 4.1. A 1 kN load cell with an error of ± 5 N was used for these tests.

Assuming that there is no yielding within the sample, the formula for the strength of a beam in four point flexure is:

$$S = \frac{3PL}{4wd^2} \quad [4.1]$$

where P is the load at failure, L is the length of the outer span on the four point test rig, w is the width of the sample and d is the depth or thickness. For the samples tested in these experiments, $L = 20$ mm, $w = 2$ mm, and $d = 1.5$ mm.

The strain at the tensile surface ε can be calculated from the equation:

$$\varepsilon = \frac{6d}{(L-a)(L+2a)} Y \quad [4.2]$$

where a is the inner span length (10 mm) and Y is the load cell dilation.

Strain rates of 0.085 mm/s and 0.005 mm/s respectively were used during the four point bend tests and tensile tests.

4.2 Compression Tests

Samples of each grade of composite, including the pure materials, were prepared by cutting small specimens from unused four point bend bars, or leftover material. The samples were cut to the approximate dimensions of 2 mm \times 2 mm \times 1.5 mm. The samples were pressed with the 1.5 mm dimension being the compression axis. The testing was carried out on the same Lloyds 6000R

mechanical testing system as was used for the flexure tests. A strain rate of 0.005 mm/s was used in all tests.

Conventionally it is the true stress and true strain that are plotted for a compression test instead of the engineering stress and strain. These values can be calculated from the following equations (Ashby and Jones, 1991):

$$\varepsilon = \ln\left(\frac{l}{l_0}\right) \quad [4.3]$$

and

$$\sigma = \frac{Fl}{Al_0} \quad [4.4]$$

where l is the current length of the specimen, l_0 is the original length, F is the applied force, and A is the cross sectional area.

4.3 Microstructural Analysis

Samples were polished using standard metallographic techniques and optical images of the phase morphology were obtained. Images of polished sections both parallel and transverse to the pressing direction were obtained.

Some of the samples were subsequently etched using a 2% nital solution to reveal the presence of grain boundaries within the nickel phase. Images of the etched surfaces were obtained and the nickel grain size was determined manually using the linear intercept technique (Wurst and Nelson, 1972).

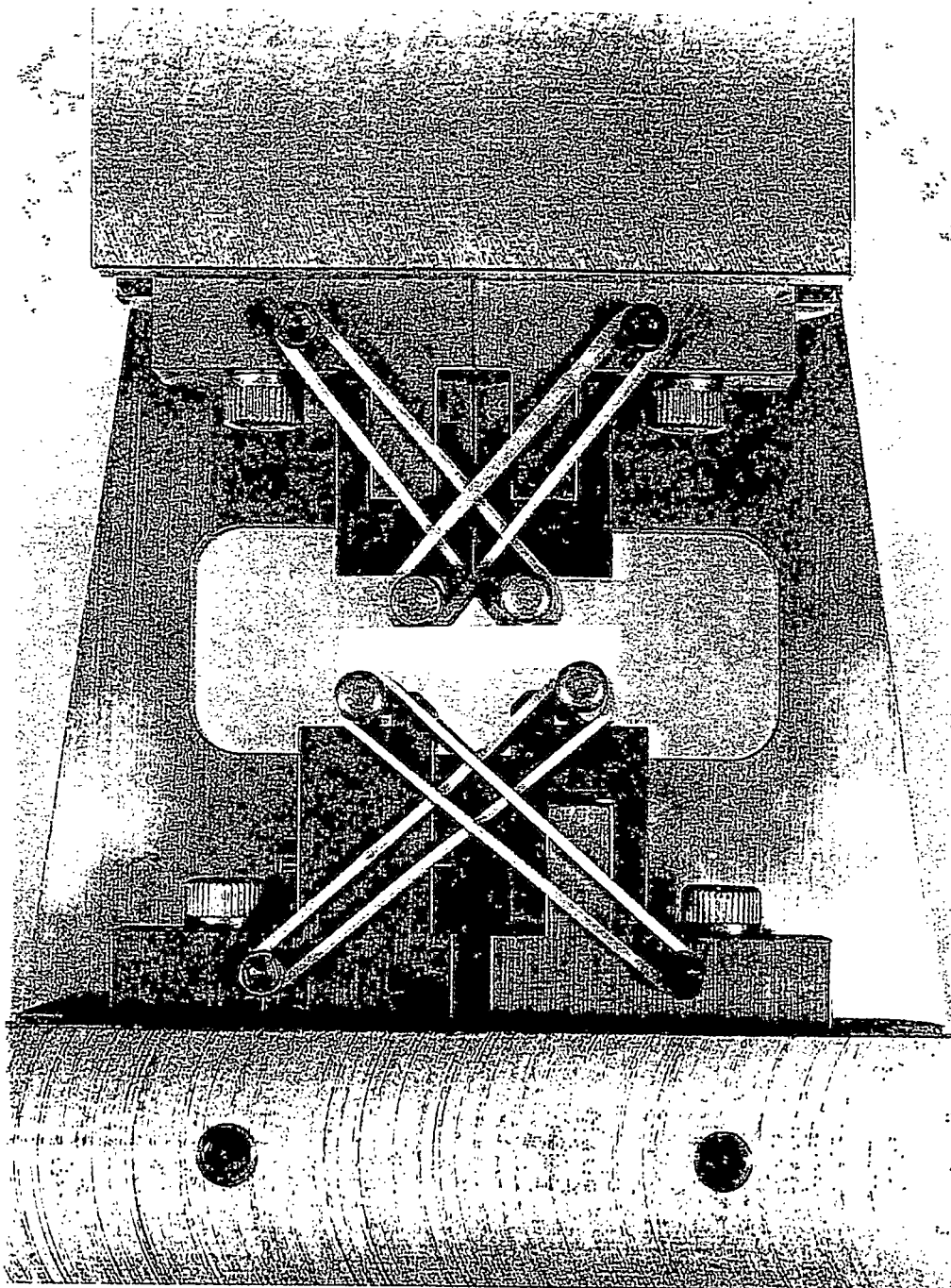


Figure 4.1 Four Point Bend Test Rig

4.4 Young's Modulus

The Young's modulus was determined using ultrasonic techniques. Sound waves are produced in the sample using an ultrasonic transducer and the time for an echo to return is measured. From this information, the Young's modulus and shear modulus of the material can be calculated. Flat polished samples with parallel faces were used for the measurements.

4.5 Hardness Testing

Polished samples were tested using a Shimadzu Microhardness tester to determine the Vickers microhardness. The samples were all tested using a 200 g load. In all of the samples except the pure zirconia, the indentation size was much larger than the size of the individual phase regions.

The hardness of a ductile material may be related to the yield stress through the equation (Ashby and Jones, 1991):

$$H = 3\sigma_y \quad [4.5]$$

4.6 Fractography

Analysis of the fracture surfaces was carried out on the Philips Electroscan Environmental Scanning Electron Microscope (ESEM) in the McMaster University Health Sciences Department. The fracture surfaces were examined to determine the nature of the damage that had led to fracture and also to identify any

unusual features in the fractured samples. In some cases, EDX analysis was carried out to identify the nature of different objects observed on the fracture surface.

One nickel sample that showed approximately 30% strain to failure and necking was sectioned along the tensile axis in order to estimate the levels of damage at different locations. The sample was sectioned using an Acutome 2 high speed saw and the surface was ground and polished carefully using standard metallographic techniques. The sample was then mounted in the Phillips Electroscan ESEM at McMaster and a number of images were obtained from various locations behind the fracture surface. The ESEM stage is motor driven and gives positional readouts in microns. The location of the fracture surface was also recorded allowing all photographs to be positionally located relative to the fracture surface. The magnification was not changed throughout the entire procedure, and two photographs were obtained for each distance behind the fracture surface. The photographs were then analyzed on a LECO 2001 image analyzer that calculated the area fraction of voids.

4.7 Carbon Analysis

The weight fraction of carbon in the nickel samples was monitored at different stages of the processing. Samples were tested using a LECO CS-444 carbon analyzer, which melts the sample in an oxygen environment and then measures the quantity of carbon dioxide produced using a calibrated photocell.

The test for carbon is destructive, so different samples were used from different stages of the processing.

CHAPTER 5

RESULTS

Analyses of the composite materials microstructures were carried out using optical micrography. Flexure data was obtained for composite grades from 15% to 100% zirconia, and tensile data for composite grades from 0% to 20% zirconia. Compression tests were conducted on samples of each material. Vickers hardness data were obtained for all composite grades. Fracture surface analysis was performed to determine the nature of the damage processes at work and to attempt to identify the cause of fracture in the composites.

5.1 Microstructure

Polished samples were prepared in order to characterize the microstructure of the composites. The samples were examined to determine the morphology in the transverse and parallel directions (Fig 5.1). Optical micrographs of the parallel and transverse surfaces are presented in Figures 5.2 through 5.6.

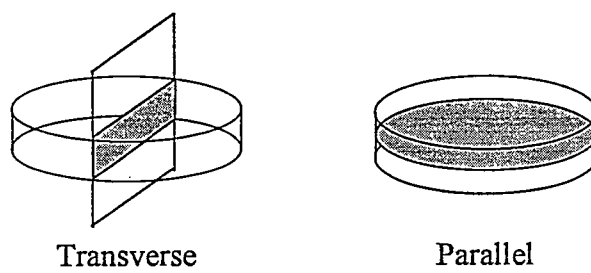
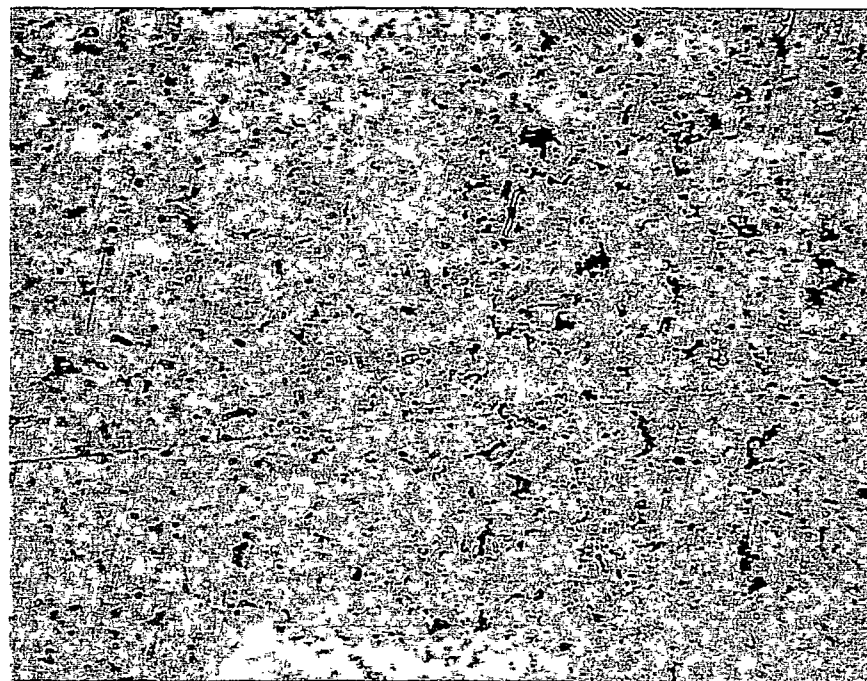


Figure 5.1 Transverse and Parallel Orientations in Samples

a)



b)

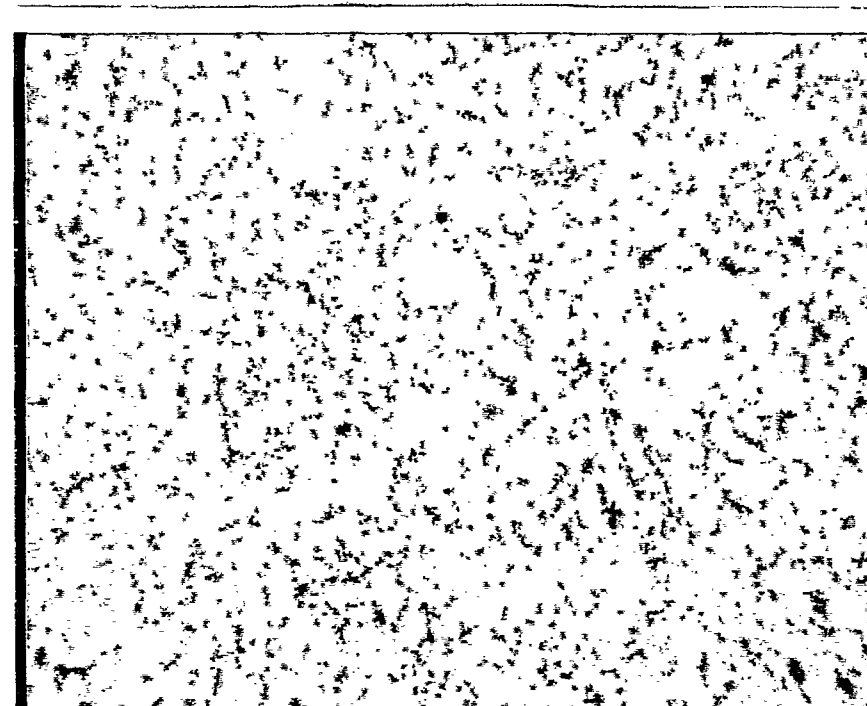


Figure 5.2 (a) Parallel and (b) Transverse Optical Micrographs of 5% Zirconia Composite (800 \times magnification)

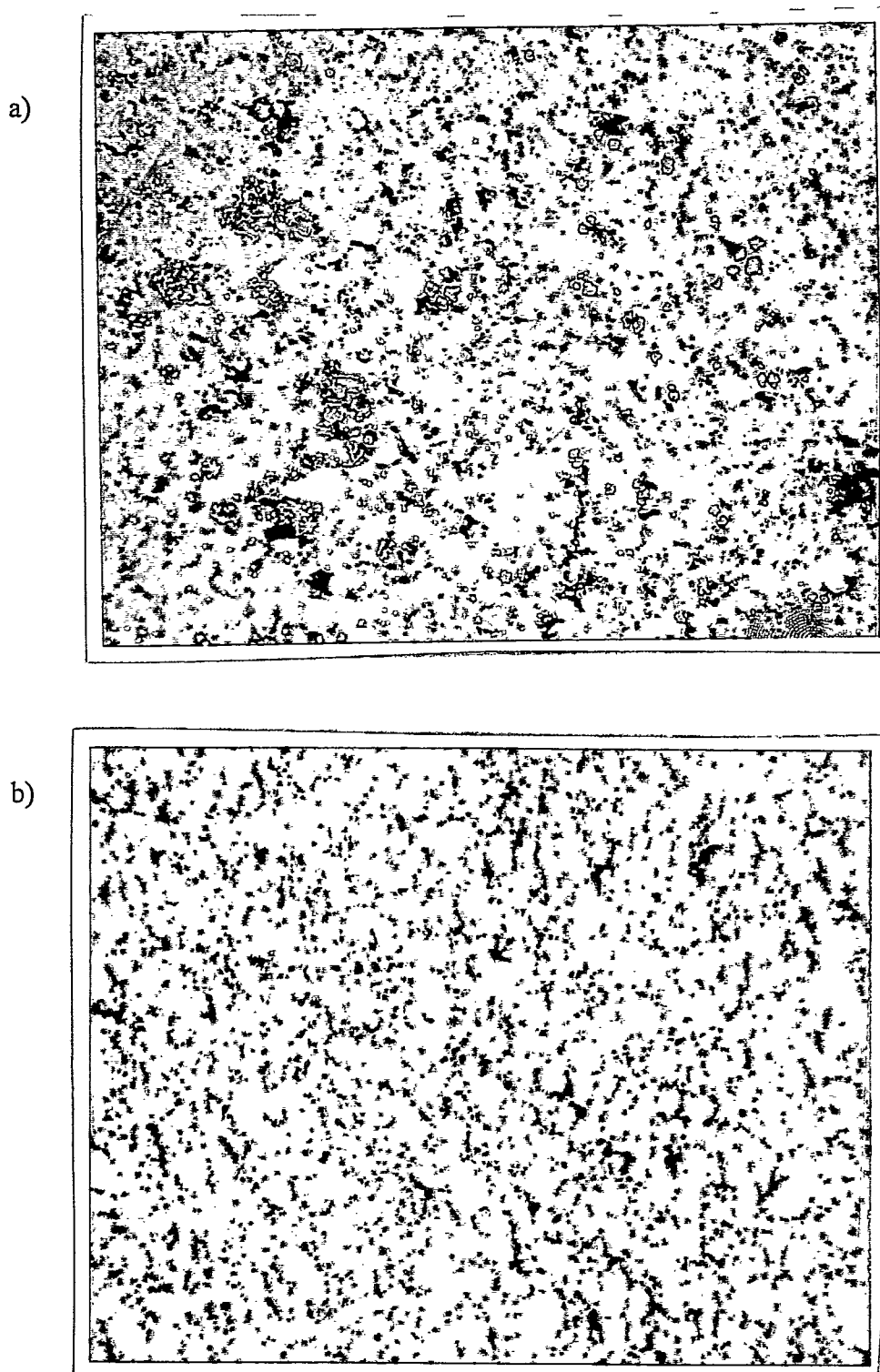


Figure 5.3 (a) Parallel and (b) Transverse Optical Micrographs of 10% Zirconia Composite (800 \times magnification).

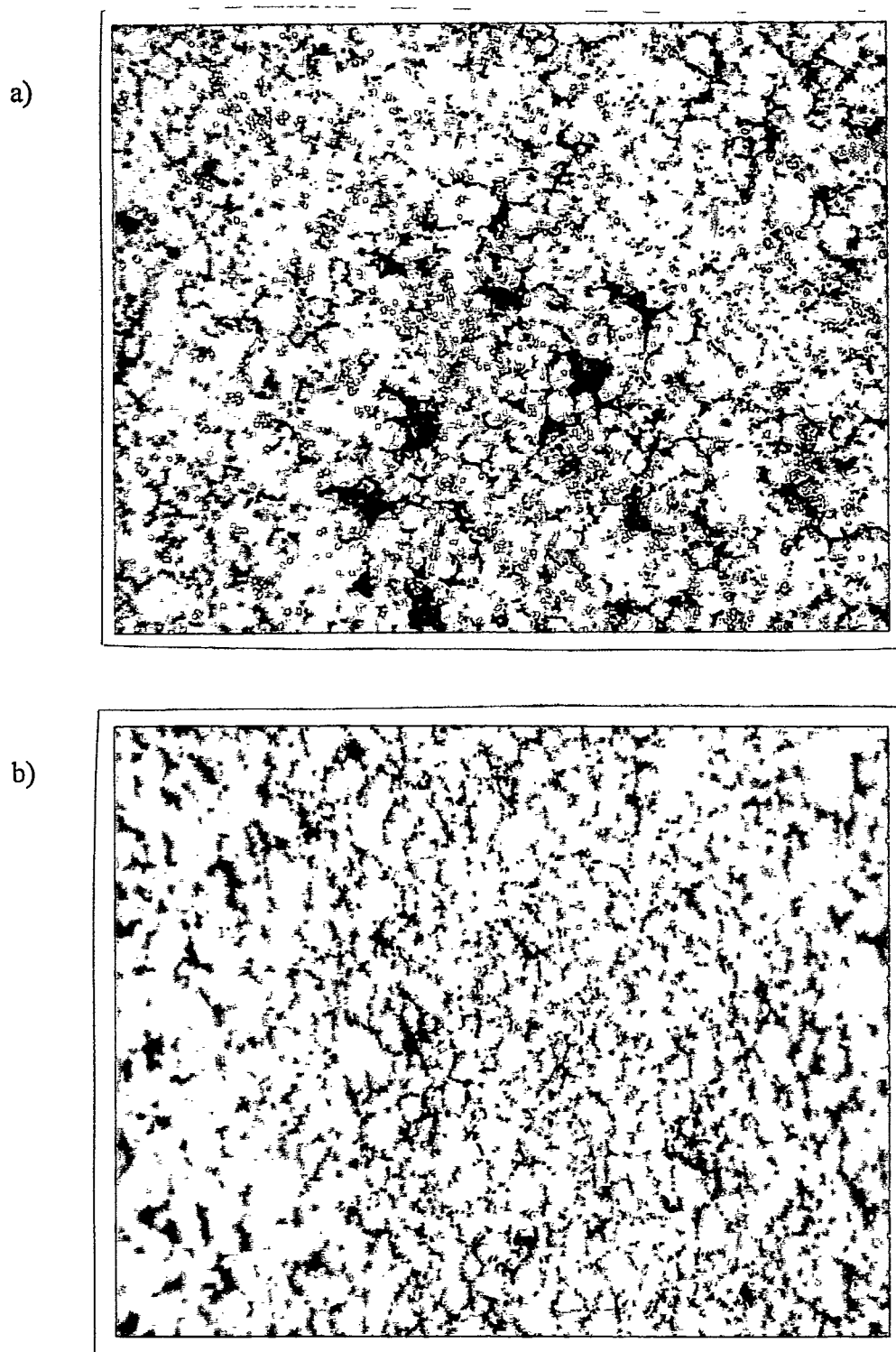
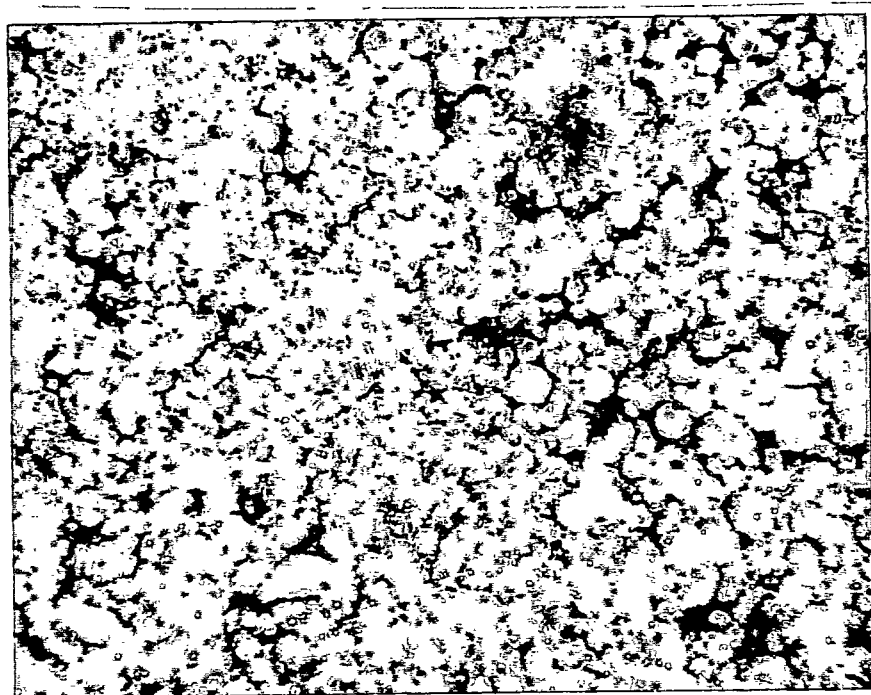


Figure 5.4 (a) Parallel and (b) Transverse Optical Micrographs of 15% Zirconia Composite (800 \times magnification)

a)



b)

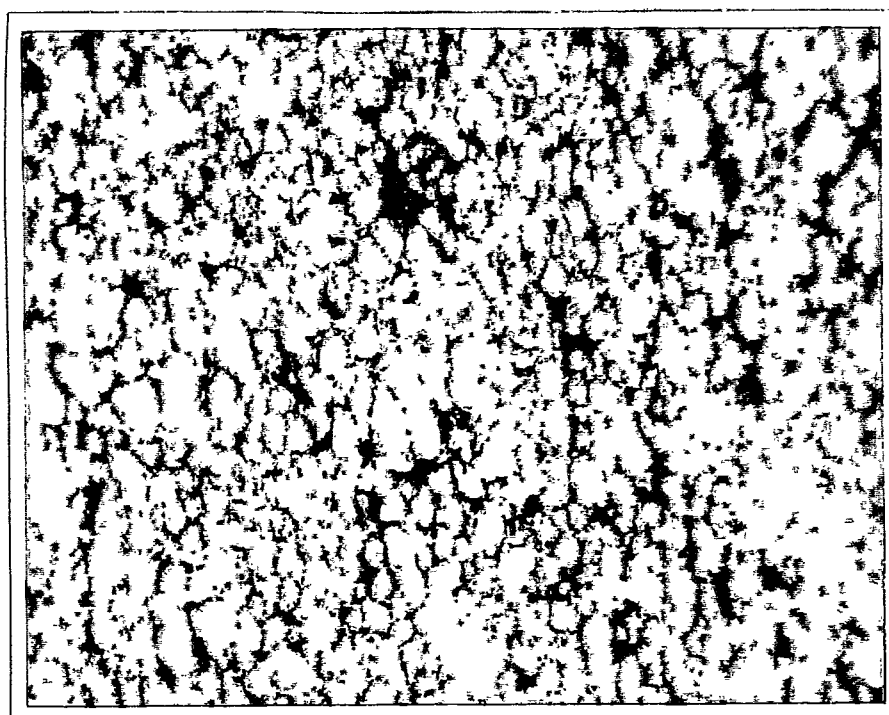


Figure 5.5 (a) Parallel and (b) Transverse Optical Micrographs of 20% Zirconia Composite (800 \times magnification)

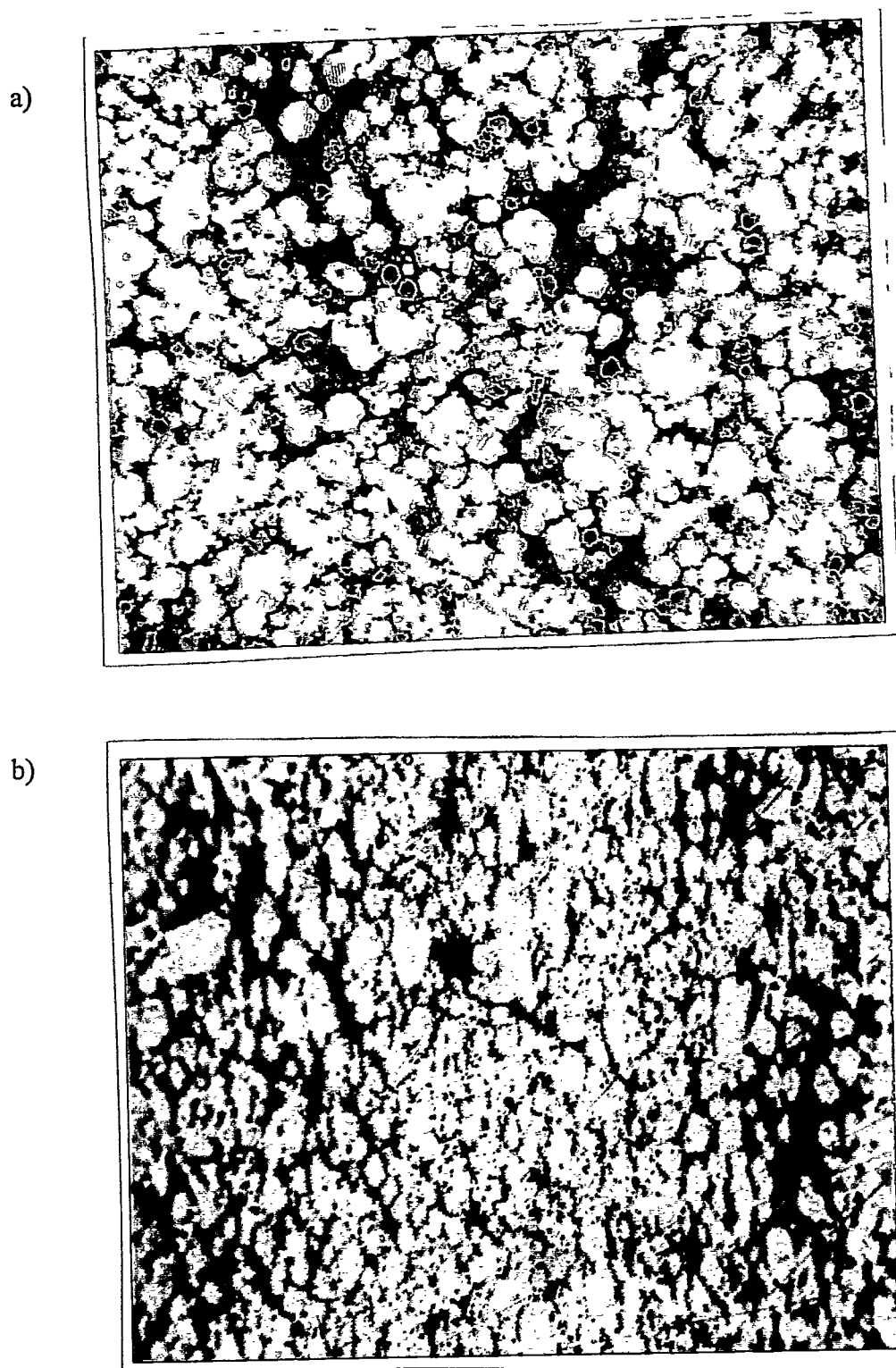


Figure 5.6 (a) Parallel and (b) Transverse Optical Micrographs of 25% Zirconia Composite (800 \times magnification)

In all of the optical micrographs presented, the zirconia phase appears as the dark region, and the nickel phase appears as the light region.

In Figures 5.2a and 5.2b, small clusters of zirconia are seen in a well dispersed morphology. The largest dark regions here are the residual pores.

Figures 5.3a and 5.3b show the 10% composite which has larger zirconia regions, but no connected lattice. This is because the micrograph is a two dimensional slice through a three dimensional network. The microstructure is again well dispersed.

Figures 5.4a and 5.4b show the presence of large (10-15 μm) regions of zirconia in the 15% composite and the outlines of many nickel grains are apparent.

The 20% material, shown in Figures 5.5a and 5.5b, displays 20 μm regions of zirconia and some apparent inhomogeneity. Many of the nickel grains in these micrographs are entirely surrounded by zirconia.

Figures 5.6a and 5.6b both show very large regions of pure zirconia at least 30 μm in size. The banded structure in Figure 5.6b is a result of differential settling of the zirconia and nickel during tape casting. In Figure 5.6a, the morphology of thin ligaments connecting nickel grains is apparent.

The densities of the samples determined using the Archimedes method are summarized in Table 5.1.

Table 5.1 Densities of Composites

Sample	Apparent Density (g/cc)	Percentage of Theoretical
0%	8.77	98.5%
5%	8.19	93.5%
10%	8.45	98.1%
15%	8.39	99.2%
20%	8.15	98%
25%	8.07	98.7%
100%	5.89	98.2%

The etched samples were analyzed using the linear intercept technique to find the average nickel grain size for each sample. A representative micrograph of an etched surface is shown in Figure 5.7.

The nickel grain size for each of the composites is summarized in Table 5.2 along with the zirconia grain size for the pure zirconia sample. The grain sizes tend to decrease somewhat as the zirconia volume fraction increases, but this could simply be experimental scatter.

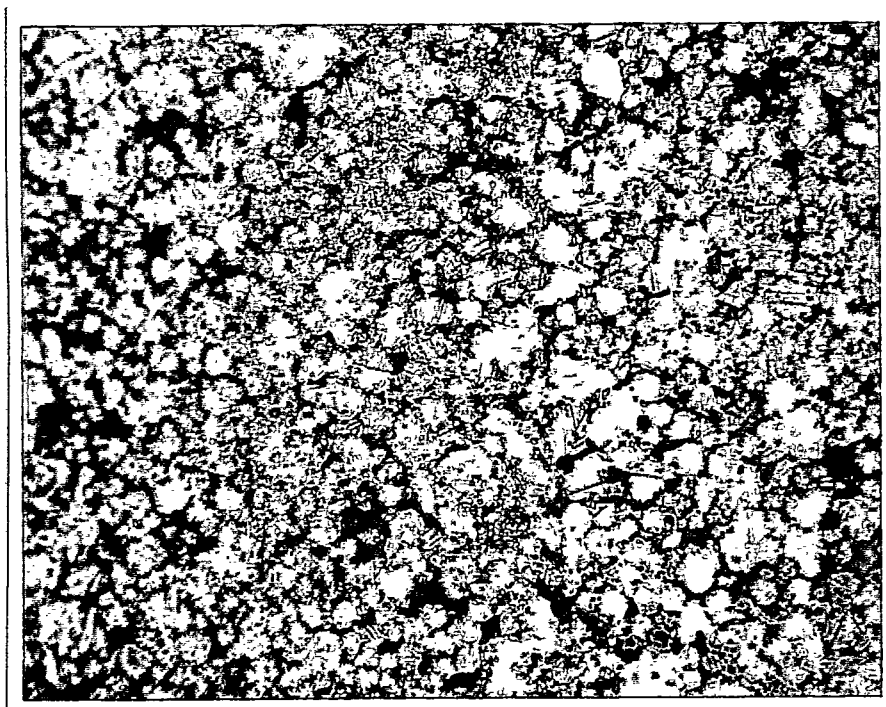


Figure 5.7 Optical Micrograph of Etched Surface of 15% Composite

Table 5.2 Grain Size of Materials

Composite Grade (% ZrO ₂)	Grain Size (μm)
0	9.85 \pm 0.8
5	10.6 \pm 0.6
10	9.6 \pm 0.6
15	9.2 \pm 0.5
20	8.4 \pm 0.6
25	8.9 \pm 0.5
100	0.6 \pm 0.2

5.2 Deformation Behaviour

Four point bend tests were carried out on the composite grades from 15% to 100% zirconia. The flexural strengths determined are shown in Figure 5.8. The interpretation of the data is only valid in the absence of plastic deformation during testing, and therefore only the data points for the 25% and 100% zirconia materials are meaningful. The data for the other grades are included for interest.

Representative stress-strain curves for the 25% and 100% materials of the composite grades are included as Figures 5.9 and 5.10. The stress was calculated at the tensile surface of the specimen.

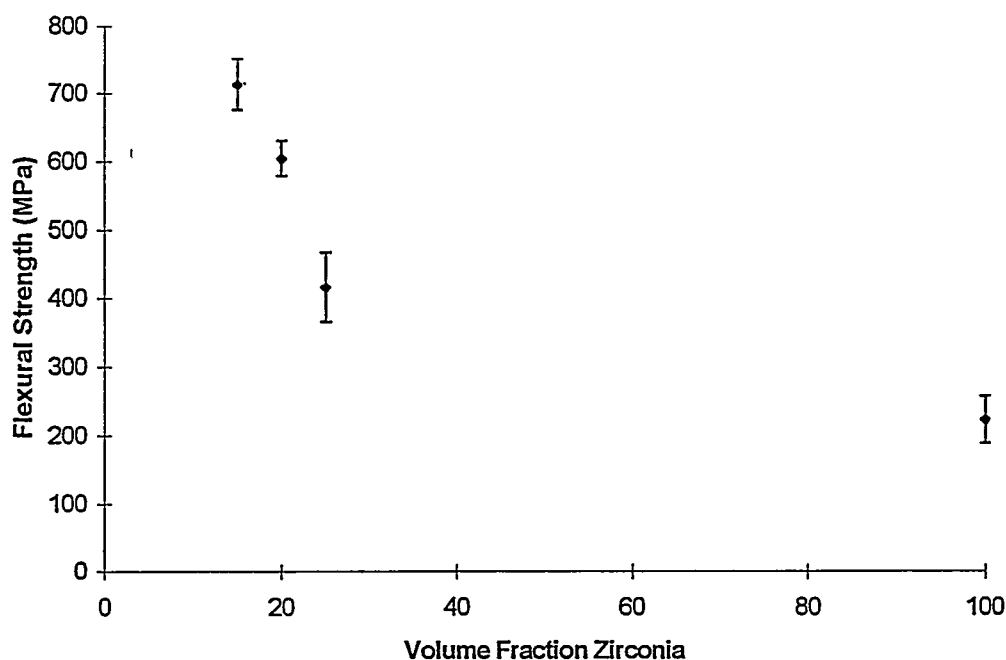


Figure 5.8 Flexural Strengths Determined Using Four Point Bend Test

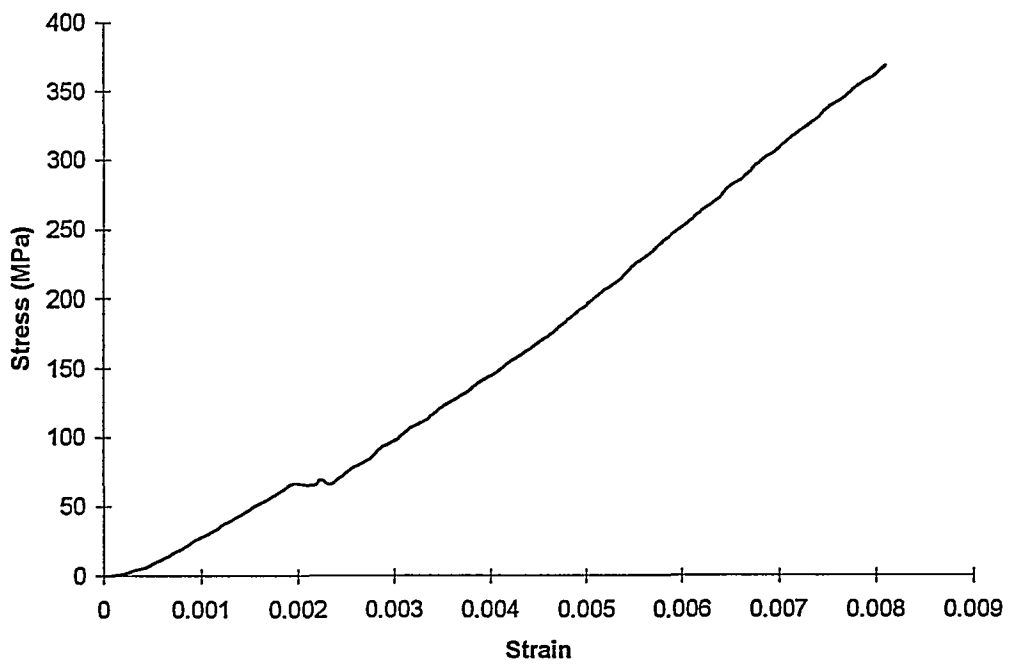


Figure 5.9 Stress Strain Curve for 25% Composite Undergoing Four Point Bending

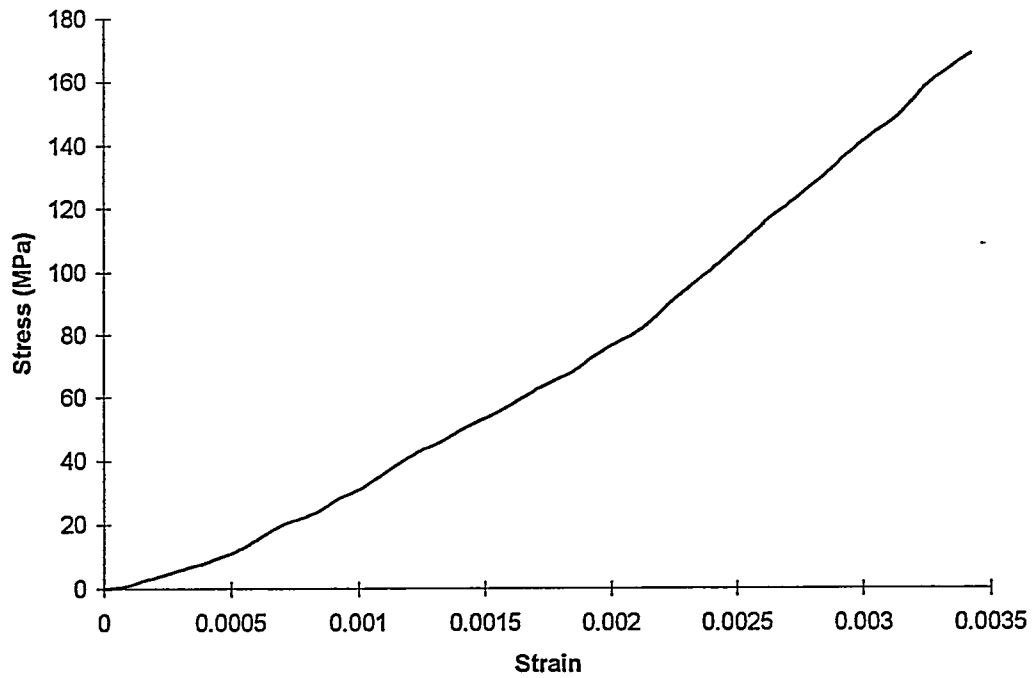


Figure 5.10 Stress Strain Curve for 100% Zirconia Sample Undergoing Four Point Bending

Tensile tests were carried out on composite grades from 0% to 20% zirconia. The tensile strengths determined are summarized in Figure 5.11.

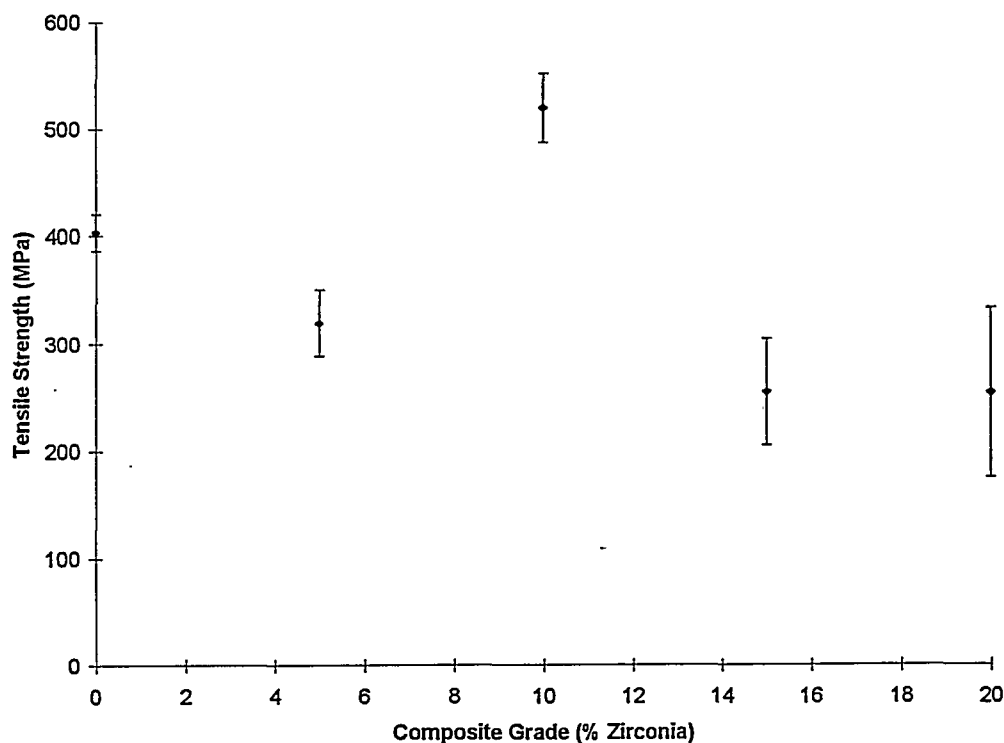


Figure 5.11 Tensile Strength of Composites

A stress strain curve for one of the pure nickel samples is included as Figure 5.12, and one for a 10% sample is included as Figure 5.13. The stress strain curve for the nickel sample was used to calculate the strain hardening parameters. The 10% sample is interesting because it shows significant ductility, and a higher work hardening rate than the pure material.

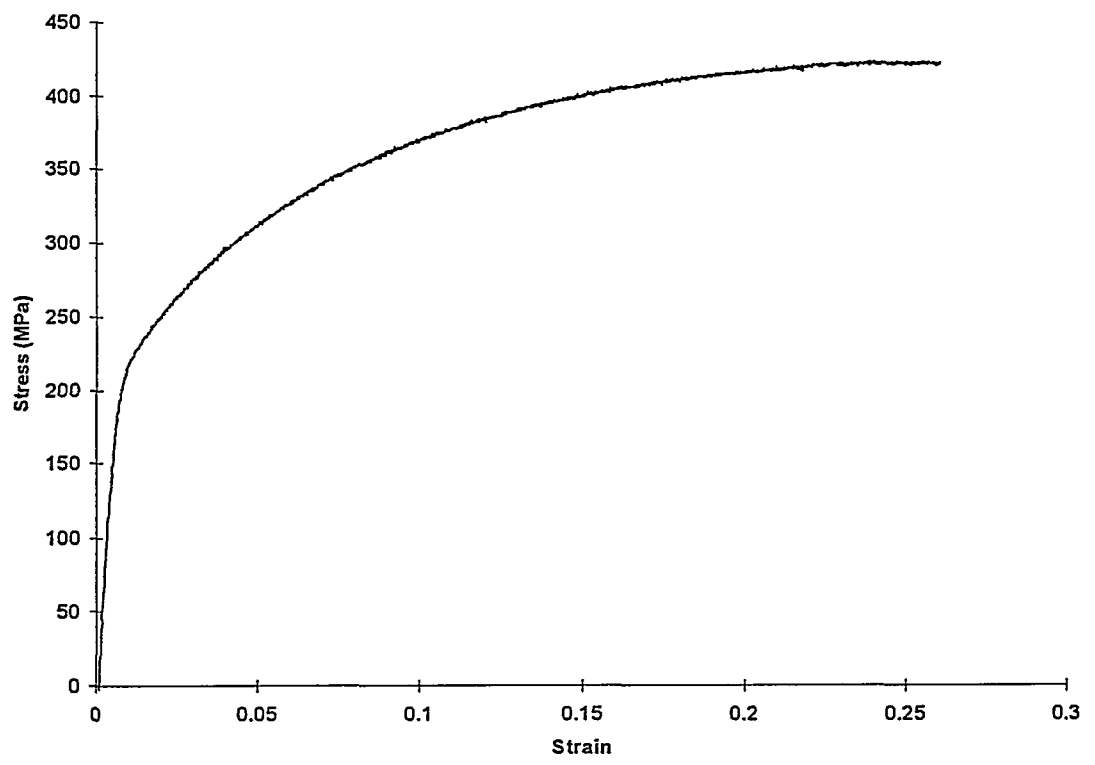


Figure 5.12 Stress Strain Curve of Pure Nickel Sample

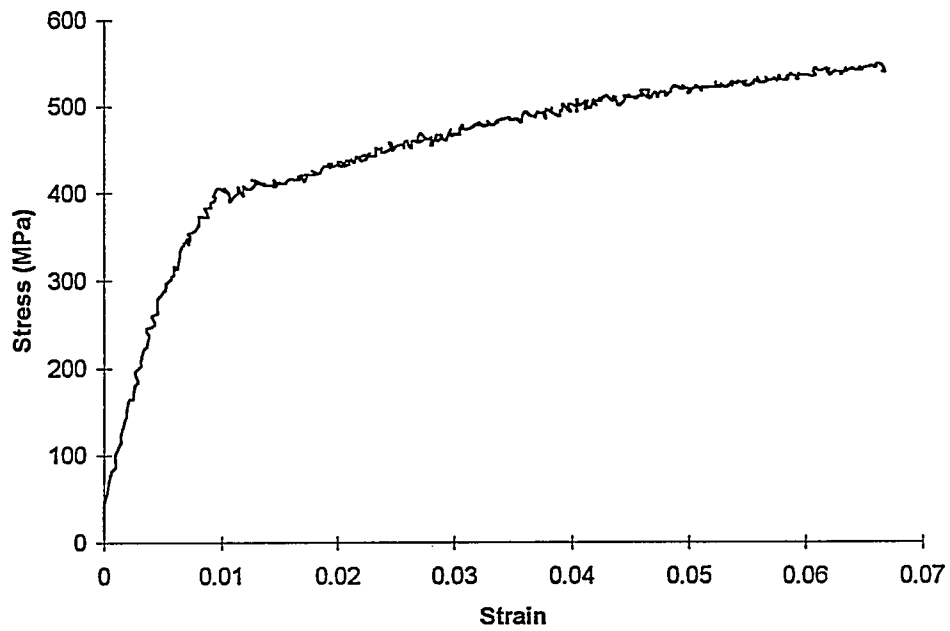


Figure 5.13 Stress Strain Curve of 10% Zirconia Sample

The strain to failure of the composite grades were recorded, and are illustrated in Figure 5.14. This shows the behaviour typical of a dispersion strengthened alloy.

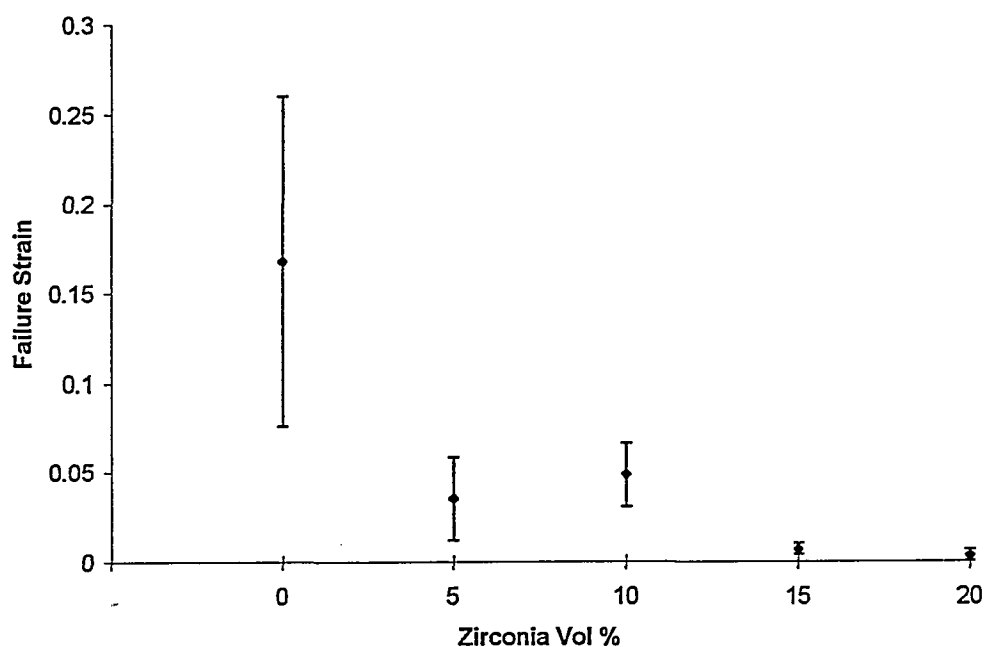


Figure 5.14 Strain to Failure for Composites in Tensile Test

Compression tests were carried out to determine the yield strengths of the composites while suppressing fracture. A true stress / true strain curve for the pure nickel is included as Figure 5.15, one for the 10% composite as Figure 5.16, and for the 25% composite as Figure 5.17.

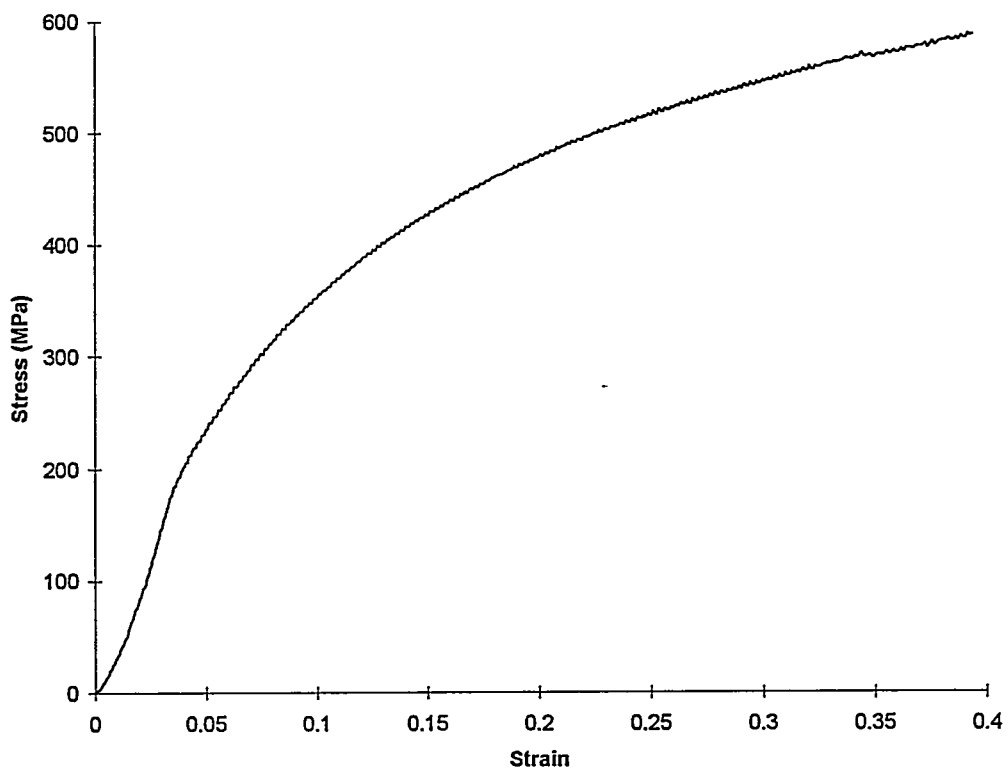


Figure 5.15 Compressive Stress Strain Curve for Pure Nickel

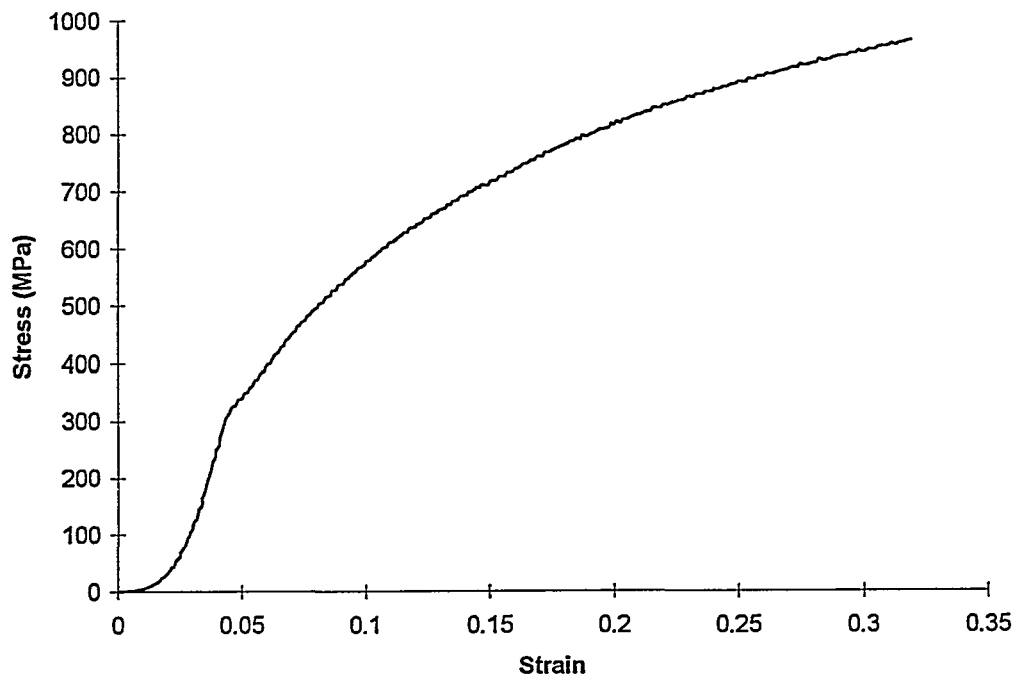


Figure 5.16 Compressive Stress Strain Curve for 10% Composite

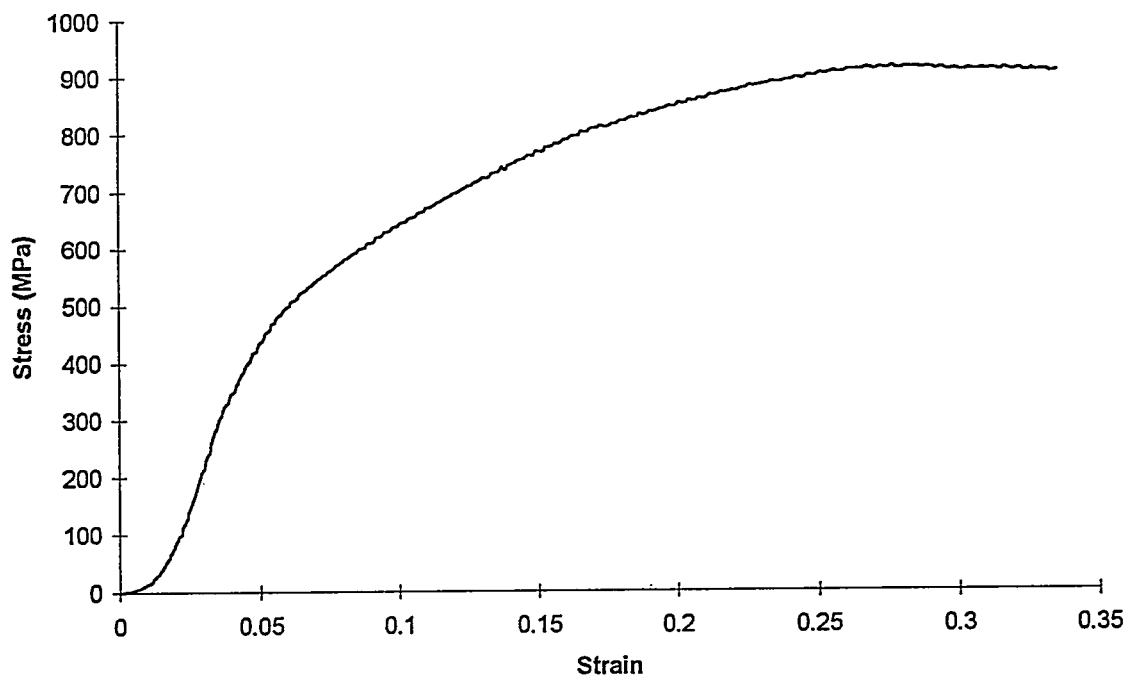


Figure 5.17 Compressive Stress Strain Curve for 25% Composite

These figures illustrate the increasing yield strength of the materials in compression.

5.3 Fractography

Images of the fracture surfaces for some of the materials are shown in Figures 5.18 to 5.25. The fractures of the pure nickel and the 5% zirconia composite are primarily ductile, while there is much more brittle failure of zirconia on the fracture surface for higher volume fractions of zirconia. High magnification images were used to try to ascertain the mode of failure in the sample, and low magnification images are presented to give a general impression of the nature of the fracture surface. The electron atomic mass contrast between nickel and zirconia is low, making it difficult to distinguish between the two phases. In general, the zirconia is the slightly lighter and smoother phase. The nickel is characterized by sharp points and cup-like structures.

Figures 5.20 and 5.21 show the 5% and 10% fracture surfaces. The 5% material has 5 μm to 6 μm pockets, whereas the 10% material has clusters of 1 μm to 2 μm pockets surrounded by zirconia. Figure 5.22 shows the development of a full network of zirconia. Figure 5.23 shows a close-up of a fractured ligament between two nickel grains. Note that the interface around the ligament appears to have fractured. Figure 5.24 clearly shows the presence of nickel grains that have been pulled out of the zirconia network. Figure 5.25 shows the intergranular fracture surface of the pure zirconia material.

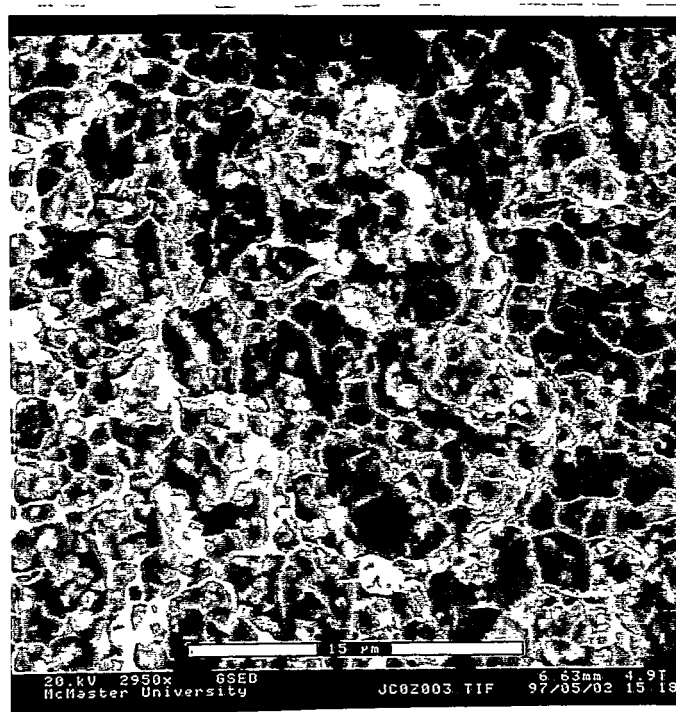


Figure 5.18 Micrograph of Pure Nickel Fracture Surface



Figure 5.19. Close-up of Particles on Nickel Fracture Surface

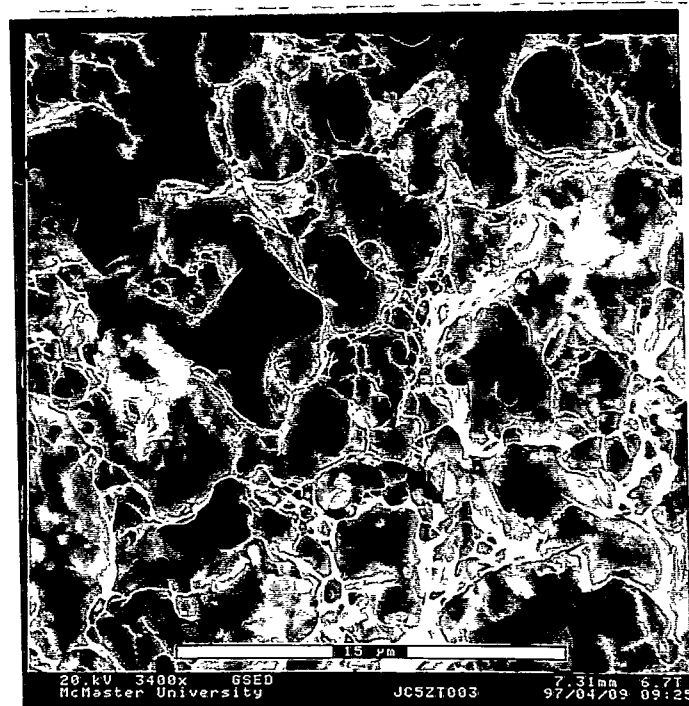


Figure 5.20. Micrograph of 5% Composite Fracture Surface



Figure 5.21. Micrograph of 10% Composite Fracture Surface

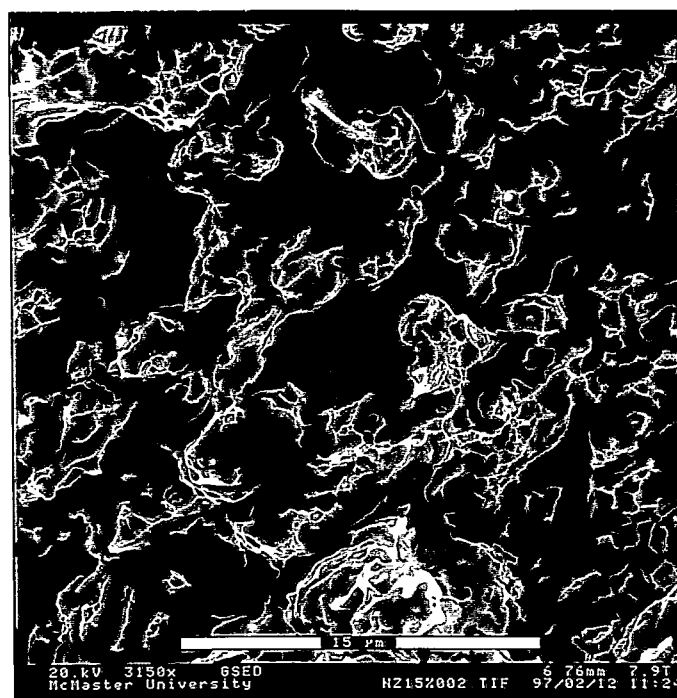


Figure 5.22. Image of 15% Composite Fracture Surface

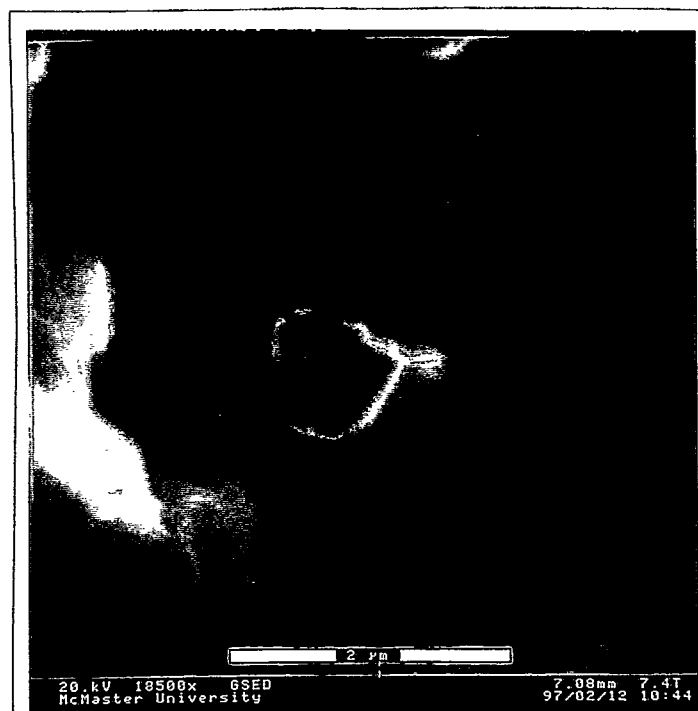


Figure 5.23. Close-up of Ductile Fracture in 20% Composite

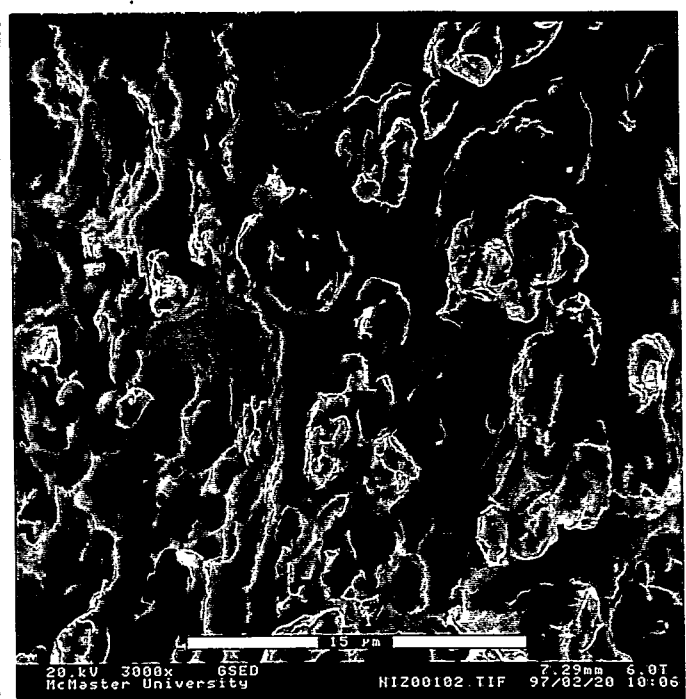


Figure 5.24. Micrograph of 25% Composite Fracture Surface

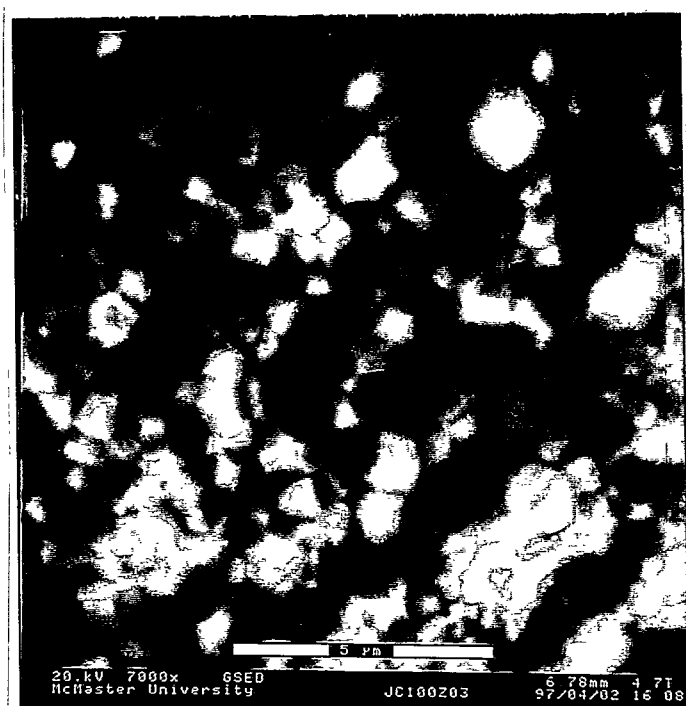


Figure 5.25. Fracture Surface of 100% Zirconia Sample

Particles were observed on the fracture surface of the pure nickel sample that showed 30% strain to failure; these are shown in Figure 5.19. These particles were investigated using the EDX system on the ESEM. The EDX spectra obtained (Fig 5.26 and 5.27) showed an increase in the carbon signal of the particles relative to the bulk of the sample. This indicates that the particles are nickel carbides.

This sample was also sectioned and the area fraction of voids was measured at different distances behind the fracture surface within the necked region. The cross sectional area of each point was also measured and converted into a local strain measurement. The results of this analysis are presented in Figure 5.28. Micrographs of the sectioned surface are shown in Figures 5.29 and 5.30. The image in Figure 5.29 is from a region immediately behind the fracture surface, while the image in Figure 5.30 is from a region several millimeters from the fracture surface.

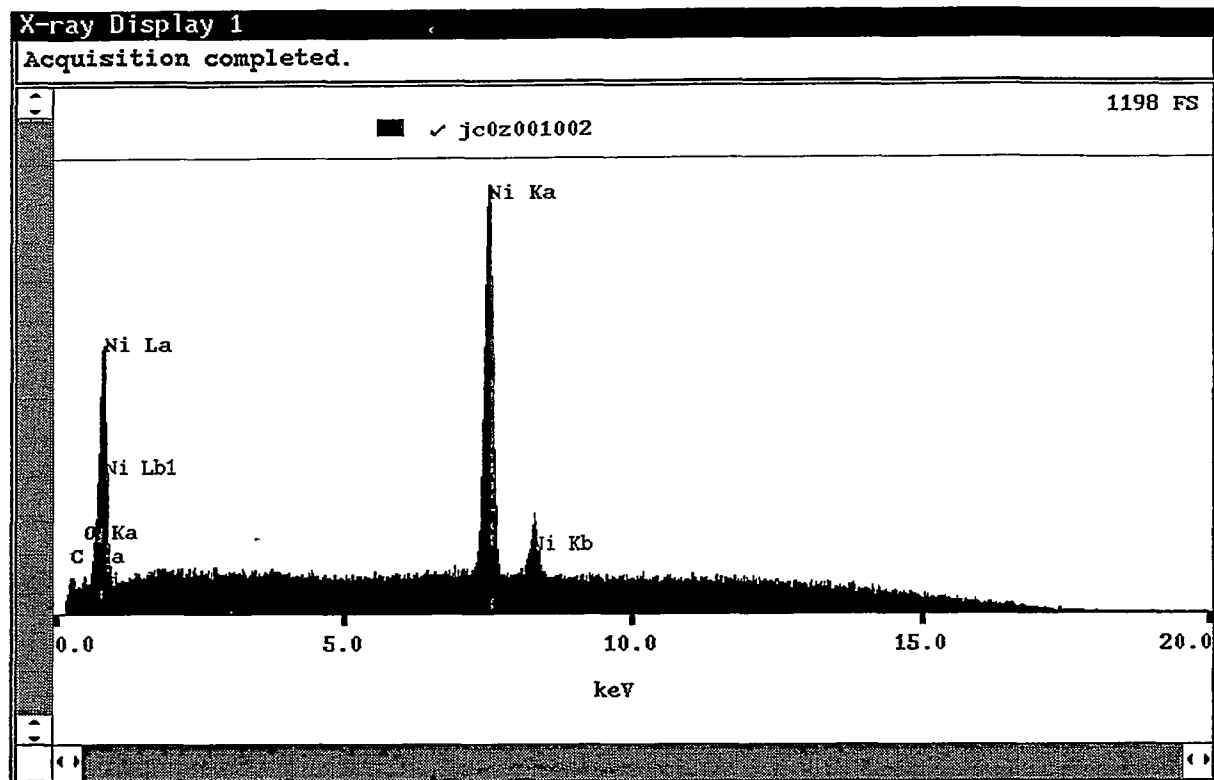


Figure 5.26 EDX of Fracture Surface of Nickel Sample away from Particles

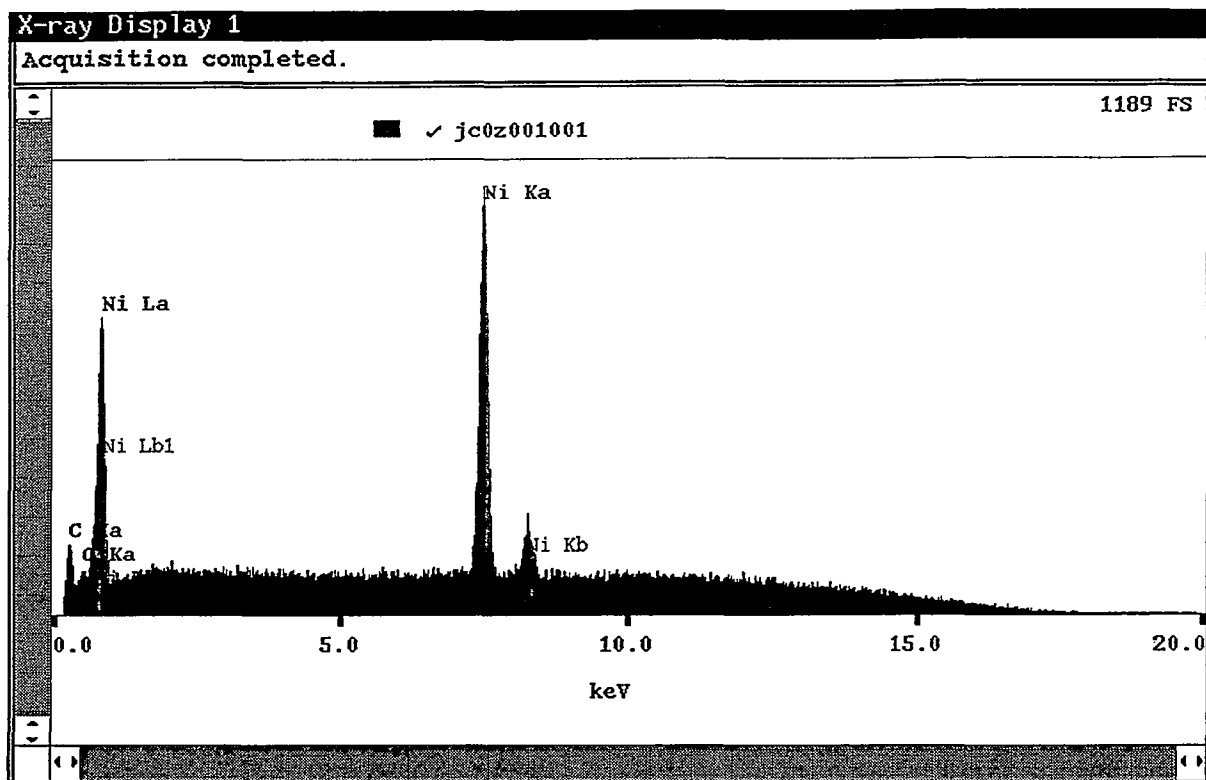


Figure 5.27 EDX of Particle on Fracture Surface of Nickel Sample

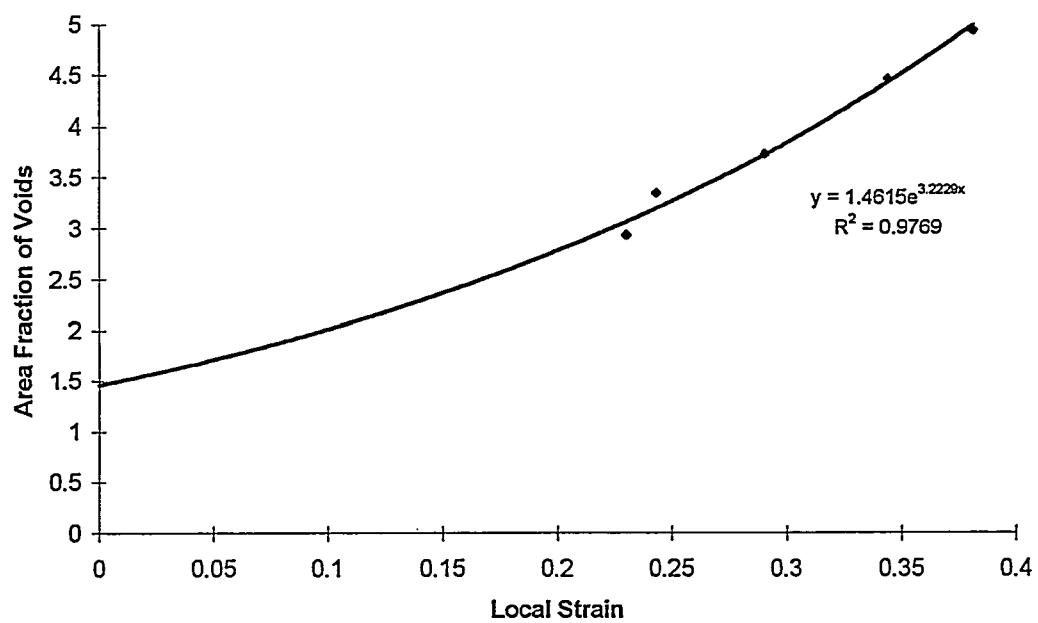


Figure 5.28 Damage in Necked Region of Tensile Sample

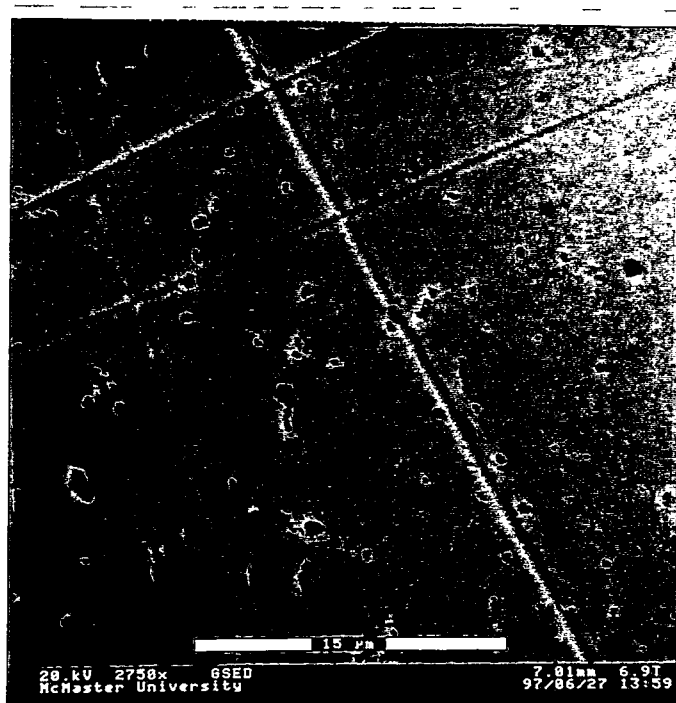


Figure 5.29. Image of Sectioned Nickel Sample Immediately Behind Fracture Surface

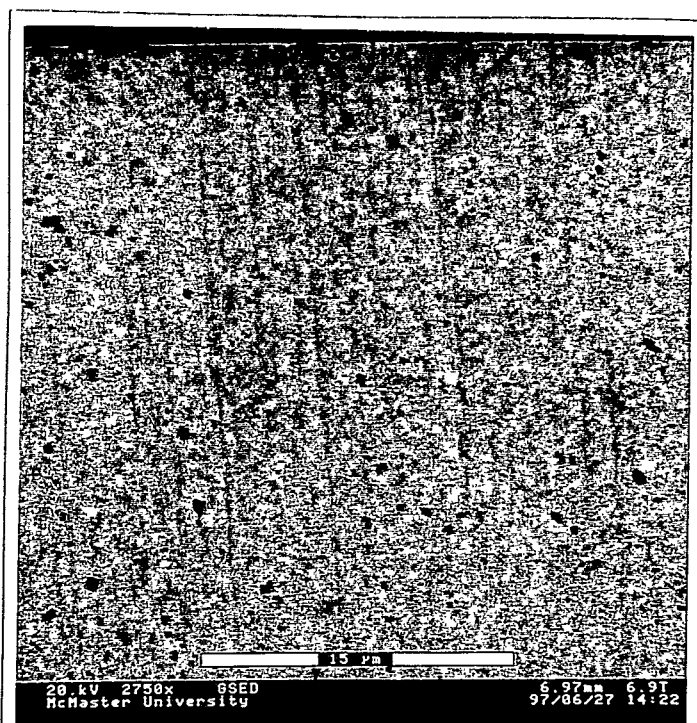


Figure 5.30. Image of Sectioned Nickel Sample Several Millimeters From Fracture Surface

5.4 Young's Modulus Measurements

The ultrasonic measurements of the Young's modulus indicate that there is a linear relationship that increases with the volume fraction of zirconia. The moduli for the pure nickel and pure zirconia are 212 GPa and 237 GPa respectively. The data are summarized in Figure 5.31.

5.5 Hardness testing

Vickers microhardness measurements of the materials was carried out and the results are presented in Figure 5.32. The values for the composites follow a linear relationship.

5.6 Carbon Analysis

The carbon levels in the nickel samples were measured at three points during processing. The raw powder was measured, samples were measured after burnout, and again after hot pressing. The levels at these points are summarized in Table 5.3.

Table 5.3 Carbon Levels Throughout Processing

Stage of Processing	Bulk Carbon Level (wt %)
Raw Powder	0.077
After Burnout	0.044
Final Product	0.025

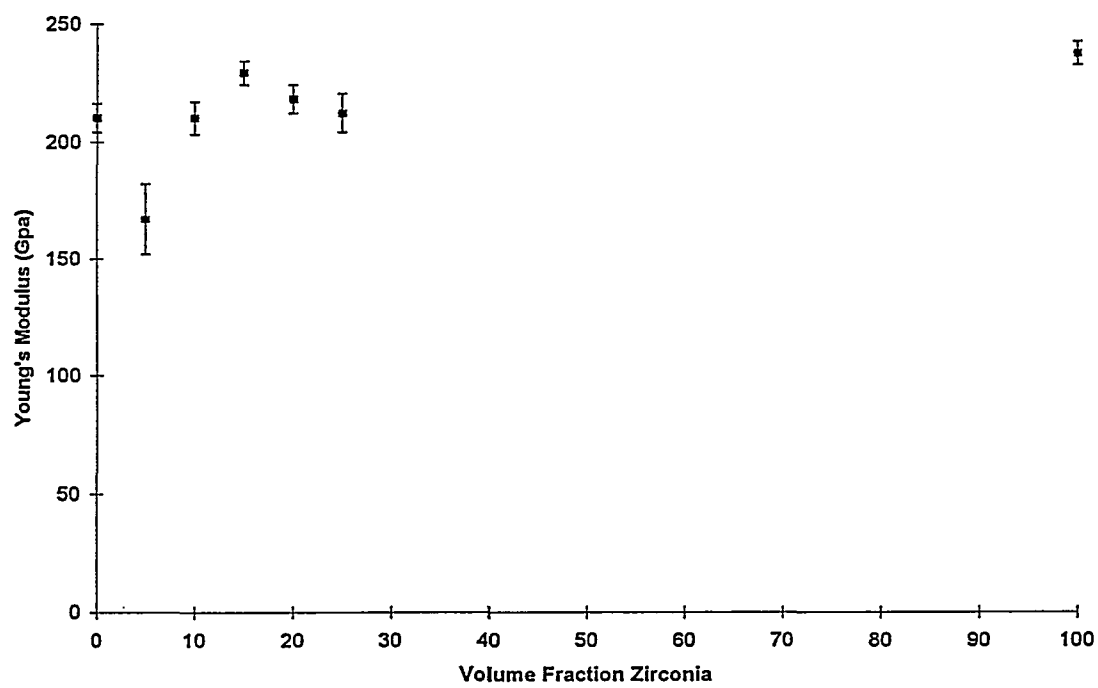


Figure 5.31 Ultrasonic Measurement of Young's Modulus

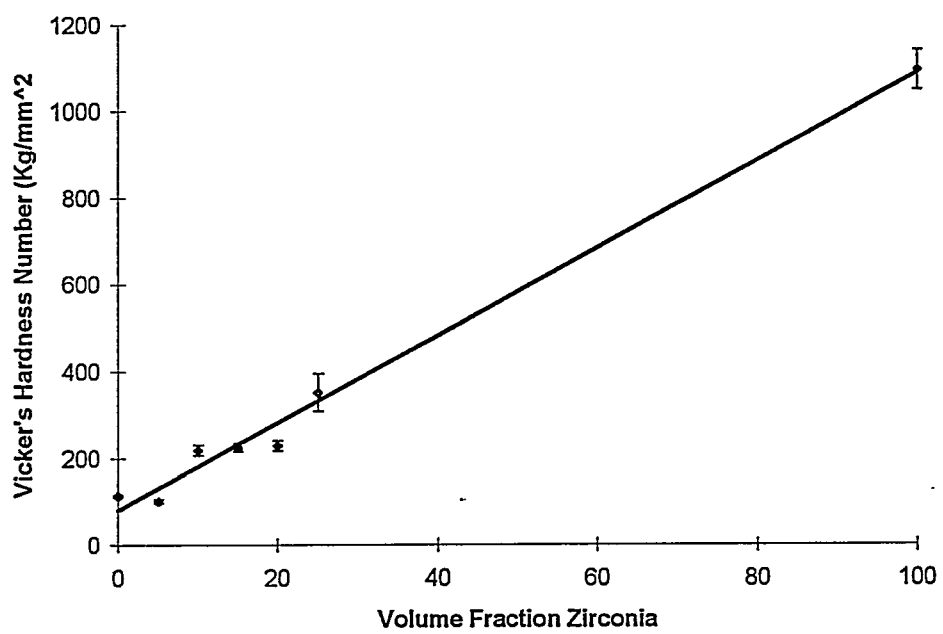


Figure 5.32 Vickers Microhardness Measurements

CHAPTER 6

DISCUSSION

This chapter begins with an analysis of the processing of the composites and the characteristics of the resulting microstructures. This is followed by a discussion of the mechanical behaviour of the materials including the strength, hardness and fracture behaviour.

6.1 Processing

In this section various aspects of the processing are discussed. The raw materials, tape casting, lamination, burnout and reduction, and hot pressing are covered.

6.1.1 Raw Materials

The raw nickel and zirconia powders were selected for purity and powder characteristics and both appear to have been appropriate choices. Difficulties with brittle, strong nickel encountered while using ONF nickel (Sarafinchan, 1995) appear to have been resolved by the selection of the INCO 123 nickel powder. EDX analysis of fracture surfaces did not reveal the presence of any unusual elements that might have weakened the composite.

An ideal system for testing the properties of IPCs would have particle sizes much closer to each other than they were in the materials used in this study, but as very pure metal powders in the sub micron size range are not available, an ideal system cannot be achieved.

One option that was not explored in this research was the reduction of very fine nickel oxide powder. However, this would have resulted in problems during the hot pressing stage because of the formation of hard agglomerates during the reduction process. It would also be very difficult to handle submicron nickel powders as they would be pyrophoric and would need to be stored and used in an inert atmosphere.

The size of the zirconia powder cannot be increased because of the concurrent reduction in driving force for sintering.

Possibilities for fabrication of the composites through an infiltration process are also limited as systems with weak interfaces tend not to wet each other and thus are difficult to infiltrate.

6.1.2 Tape Casting Process

The tape casting process has a number of inherent difficulties that create challenges for creating uniform, well dispersed composite tapes. The nature of the polymerization reaction that occurs to form the tape requires the use of fresh reagents, especially as the effectiveness of the plasticizers appears to decrease with age (Clayton, 1997). Difficulties also arise from the necessity to co-process two

powders with a particle size ratio of twenty to one. The quantities of binder required to form a tape with the nickel particles are rather different than those required for the zirconia particles. As it was not practical to optimize the formulation for each grade of composite, a weighted average of the two formulations was used. This is not the ideal situation.

This problem with a large difference in particle sizes was most notable with the 25% zirconia composites, as there was marked separation with nickel sinking to the bottom of the tape. Addition of extra binder tended to alleviate the problem, but the tape used to make the final product still showed segregation which is evident in the microstructure seen in Figure 5.6 (b).

The pure zirconia tapes displayed significantly more shrinkage than the nickel containing tapes. In addition, the zirconia tapes were much less ductile than both the nickel and composite tapes and were more prone to cracking during the drying process. It is believed that the semi-circular cracks which occasionally appeared within the zirconia tapes were caused by the presence of hard agglomerates in the zirconia powder.

6.1.3 Lamination, Burnout and Reduction

The lamination procedure was effective. However, there may have been fewer problems with cracking in later processing if the die could have been maintained at a constant temperature throughout the lamination process. It may be

possible to accomplish this using a thermal blanket which could be wrapped around the die while it is inside the press.

The burnout procedure used was effective in removing the organic material from the samples and the gas evolution rates were low enough to avoid significant cracking. The formation of the oxide layer was detrimental to the densification of the final product. The oxide layer was successfully reduced in twelve hours by a flowing mixture of 5% H₂ in argon at a temperature of 500°C. Insufficient reduction left an oxide film on the nickel and prevented pressing to full density. Therefore, the burnout and reduction cycles were modified several times. If the final burnout temperature was too low, samples had limited mechanical strength and contained residual carbon. However, a high temperature over sintered the material and resulted in the formation of a very thick oxide that required an even longer reduction cycle to eliminate. The use of carbon monoxide as a reducing agent was investigated but discarded to avoid the potential hazards associated with carbon monoxide and the possible formation of nickel carbonyl, a highly toxic gas.

6.1.4 Hot Pressing

The hot press used for consolidation of the final materials had a number of inadequacies that posed problems during processing. The pressure regulators were not capable of maintaining a constant ram pressure and the pressure would decrease as the sample shrank. This necessitated constant monitoring of the pressure to ensure it stayed close to the nominal pressure of 40 MPa. The vacuum

system on the press was capable of reaching a pressure of 2×10^{-4} torr. Ideally this pressure should be several orders of magnitude lower to prevent oxidation of the samples while at high temperature.

It is standard practice to use graphite as the die material but its use can pose difficulties. Carbon is soluble up to 0.5 weight % in nickel (SGTE, 1997) and, as a result, boron nitride must be used as a diffusion barrier throughout the system. In one case this procedure was accidentally omitted and the graphite pistons diffusion bonded to the nickel sample being pressed, ruining both the sample and the pistons. Realistically, the lifetime of each pressing die is only about ten to twelve units before the inside of the die is badly scarred. The useful lifetime of the pistons is much less, and they usually had to be refaced after three or four pressing runs. Unfortunately, other materials, such as alumina, that might be more durable and would avoid exposing the samples to carbon, are prohibitively expensive.

6.2 Microstructure

The size and scale of the microstructure were controlled primarily by the nickel phase. The final size of the nickel grains was limited mainly by the presence of the zirconia phase which inhibited further grain growth. In the 5% material, the grain size was slightly larger ($10.6 \mu\text{m}$) than the other composites which ranged from $8.4 \mu\text{m}$ to $9.6 \mu\text{m}$, although this value is not outside of experimental uncertainty. This composite grade also showed some very large grains

characteristic of secondary grain growth. The small, unconnected pockets of zirconia in the 5% material would restrict grain growth less than the percolating lattice in the 10% and above grades. It is also possible that zirconia particles were engulfed within grains of nickel and could therefore act as nucleation sites for damage within the nickel.

It is not clear why the 5% material did not achieve full density under the same processing conditions as the other composites. Samples from two different tapes were prepared and both failed to reach full density.

The relative size difference between the starting powders was evident in the microstructures that developed in the composites. In the composites with higher zirconia volume fractions, the optical microstructures (Figs. 5.5 (a) and 5.6 (a)) clearly show the presence of individual nickel grains surrounded by a network of zirconia. The nickel appears to be connected primarily at points where two powder particles were in contact prior to sintering. This is also apparent in the images of the fractured samples where the nickel grains appear to be surrounded by a continuous lattice of zirconia, and there are ductile areas of cup cone fracture in holes in the zirconia network where nickel grains were connected (Fig 5.23). From a standpoint of fracture resistance, this is not the ideal microstructure as the work by Prielipp et al. (1995) shows that a larger ligament diameter leads to a higher toughness.

The scale of these ductile fracture regions was of the order of 2-3 μm , which is significantly larger than the ligaments in the Al/Al₂O₃ composites studied

by Prielipp et al. (1995). The fracture regions are however surrounded by zirconia and are therefore constrained. The micrographs indicate that the nickel has pulled away from the surrounding zirconia, and that the interfaces are weak. According to Ashby et al. (1989), this mode of fracture should lead to more ductility within the ligament and a higher overall contribution to the work of fracture compared to a system with strong interfaces.

6.2.1 Percolation Threshold

It appears that the percolation threshold for zirconia in the composites studied lies below 10% volume fraction of zirconia. The 5% material displays either individual discrete particles of zirconia on the fracture surface or small regions that do not appear to be connected (Fig 5.20), but this could be a result of the residual porosity. In the 10% material on the other hand, there appears to be connected regions of the zirconia throughout the composite. The fracture surface is more characteristic of the higher volume fraction composites than of the pure nickel and 5% materials.

This level for the percolation threshold is very reasonable given the particle size ratio between the different components. The typical percolation threshold of 15% to 17% for the minor phase in a three dimensional lattice would be reduced as the ratio of the particle sizes increases. In a two dimensional lattice, a particle size ratio of twenty to one can reduce the percolation threshold from 0.5 to 0.07 (Nan,

1993). Similar calculations have not been performed for general three dimensional lattices.

6.3 Fractography

The SEM images of the fracture surfaces of the different composites help in the understanding of the fracture and deformation mechanisms at work in the materials. The overall nature of the fracture surfaces is discussed along with references to interesting features observed in the micrographs. An analysis of the damage observed in one of the nickel specimens is also provided.

6.3.1 Fracture Mechanisms

The appearances of the fracture surfaces of the different composites fall into two groups. The first group containing the pure nickel samples and the 5% zirconia composites display fracture surfaces characteristic of ductile fracture and the coalescence of voids. The second group, with volume fractions between 10% and 25% zirconia, have fracture surfaces with regions of ductile fracture surrounded by a network of zirconia. The 10% composite still shows areas of ductile fracture 10 μm to 20 μm , but in the 20% and 25% grades the fracture surfaces clearly show regions where nickel grains have been pulled out of the surrounding zirconia shell. These pockets in the zirconia also display small (2 μm to 3 μm) areas of ductile fracture at the points where the nickel grains were in contact, as shown in Figure 5.23.

The ductile areas of the fracture surfaces have a dimpled morphology with many pits, some of which contain particles. Using EDX analysis a number of these particles were identified as nickel carbide particles, and the residual carbon levels in the final product are certainly high enough to allow large numbers of submicron carbides to be present. A simple model of uniform, spherical carbides $0.25\ \mu\text{m}$ in size leads to a particle spacing of only $2.8\ \mu\text{m}$, if it is assumed that all of the carbon in the sample is in the form of nickel carbide. Even if only ten percent of the total carbon present is in the form of nickel carbide, the particle spacing will only rise to $6\ \mu\text{m}$. In the nickel phase, these particles can act as sites for the nucleation of voids as described by Le Roy et al. (1981).

The pure zirconia samples appeared to fracture in a mixed mode with regions of intergranular fracture and regions of transgranular fracture. The zirconia within the composites seem to fracture in the same way, as both modes of fracture appear to be present in the zirconia lattice in Figure 5.23.

6.3.2 Damage in Nickel Sample

Analysis of damage in the nickel sample is useful because it indicates the basic damage mechanisms that will be active within the nickel phase in the composite materials. The mechanisms in the pure nickel will be modified by the added constraint of the zirconia lattice in the percolating composites and by the presence of zirconia particles or clusters in the 5% composite.

Figure 5.28 shows the area fraction of voids present at different levels of local strain. The relationship can be modeled with either a linear relationship, or as an exponential. Both methods give high R^2 values (>0.975). The linear model predicts a y-axis intercept of 0.12% area fraction of voids while the exponential model predicts an intercept of 1.46% area fraction. The intercept for the exponential model corresponds to the level of residual porosity in the material after hot pressing. The exponential model corresponds more closely to the rigorous models developed by Le Roy et. al. (1981) who found that the level of damage increased rapidly very near to the fracture surface.

An electron micrograph of the polished section obtained from an area immediately behind the fracture surface of the tensile specimen is shown in Figure 5.29, and a micrograph of an area several millimeters from the fracture surface is shown in Figure 5.30. Note the presence of linked voids in Figure 5.29, and the relative sizes of the voids in each case. The area fraction of voids in Figure 5.29 is 7.4%, while in Figure 5.30 it is 3.0%.

The analysis is complicated by the tensile hydrostatic stress component in the neck. However, the difference in local strain is only 15% and the radius of curvature of the neck is several centimeters. These factors should minimize the impact of the hydrostatic stress.

6.4 Mechanical Properties

The results of the flexure and tensile tests are discussed individually and the results of the compression and hardness tests are used to analyze the yield stress of the composites. This is followed by an overall analysis of the mechanical properties of the composites. This discussion will also incorporate ideas on how the microstructure of the materials has affected their performance.

6.4.1 Flexural Strength

The interpretation of the results of the flexure test is only valid if it is assumed that there was no plastic deformation within the sample during the test. This criterion was met by both the pure zirconia samples and the 25% zirconia samples. All of the other composite grades displayed some plasticity during the flexure test which prevented the use of the standard formula for determining the flexural strength.

The data for the 25% zirconia composite and the 100% zirconia material showed no plasticity and therefore the results should be valid. The value of 416 ± 51 MPa for the 25% composite is slightly above the level of 325 ± 35 MPa obtained for the same volume fraction composite by Sarafinchan (1995). This may be a result of microplasticity in the nickel. The purer 123 nickel had a higher ductility than that of the ONF nickel and this resulted in strengthening of the composite. The value of 223 ± 34 MPa obtained for the pure zirconia is lower than the 340 ± 60 MPa obtained by Sarafinchan (1995). This was probably a result of using a higher hot pressing temperature (1300°C as opposed to 1250°C) to obtain

full density at the pressure of 40MPa. The additional grain growth experienced by the zirconia would lead to a higher critical flaw size and hence a lower strength. The grain size of the material in this study was found to be roughly 0.6 μm , whereas in the earlier study it was 0.24 μm . Using Griffith's relation (Eqn. 2.2) and assuming that all other factors are the same for both samples, this difference in grain size would lead to a strength of only 214 MPa in the coarse grained material. This is sufficient to explain the discrepancy.

6.4.2 Tensile Strength

Because of the limited number and the small size of the samples, the tensile data are not ideal. Between three to six specimens were used to calculate the strength of each grade of material. The value of 403 ± 17 MPa for the tensile strength of pure nickel is consistent with values found in the literature (Ashby and Jones, 1991). Figure 5.11 shows the tensile strengths decreasing smoothly with the exception of the 10% zirconia material. This grade of composite shows an unusually high tensile strength of 518 ± 32 MPa which is higher than that of the pure material. The reasons for this high tensile strength are unknown, but could be a result of the formation of a percolating network of zirconia. Within the composite, zirconia can act as a skeleton with a high tensile strength because the zirconia phase regions are too thin for cracks to grow to a critical size. This precludes the formation of large cracks that could cause catastrophic failure in the composite. In addition, there will be load transfer to the zirconia network as the

nickel exceeds its yield stress. These two strengthening mechanisms are also active in whisker reinforced materials (Cox, 1952).

The reinforcing effects of the percolating lattice are superior to those of the particulate materials because the zirconia lattice can provide constraint and is much more capable of taking on transferred load than are individual particles.

The strength of the 5% material could not be analyzed in the same manner as the other composites because of porosity within the material. The calculated density of 93.5% of theoretical implies a porosity volume fraction of 6.5%. This porosity is in the form of relatively uniformly distributed clusters of small pores with a cluster diameter of 10 μm to 15 μm . The pores also act as damage nucleation sites and lead to a decreased strain to failure as shown in Figure 5.14. If the volume fraction of porosity is converted into an area fraction for an arbitrary plane normal to the tensile axis, there will be 6.5% less area over which the force is distributed. This first order correction would increase the ultimate tensile strength for this grade of composite to 341 ± 33 MPa.

The errors associated with the data increased as the volume fraction of zirconia rose. This was a result of the influence of the zirconia, which was behaving in a brittle fashion, and a range of critical flaw sizes. It is interesting to note that the tensile strengths observed for the 20% and 25% material, 254 ± 50 MPa and 253 ± 78 MPa respectively, are consistent with the flexural strength of the pure zirconia, 223 ± 34 MPa.

The work hardening behaviour of the pure nickel was characterized in order to obtain parameters for use in modeling of the composites, specifically for use in the model by Ravichandran (1994). The stress strain curve for the most ductile nickel sample was fitted to the expression:

$$\sigma = K\varepsilon^n + \sigma_0 \quad [6.1]$$

where K and n are the fitting parameters and σ_0 is the elastic stress in the material. The fitting parameters K and n were found to be 650 MPa and 0.55 respectively. The value of σ_0 was 195 MPa.

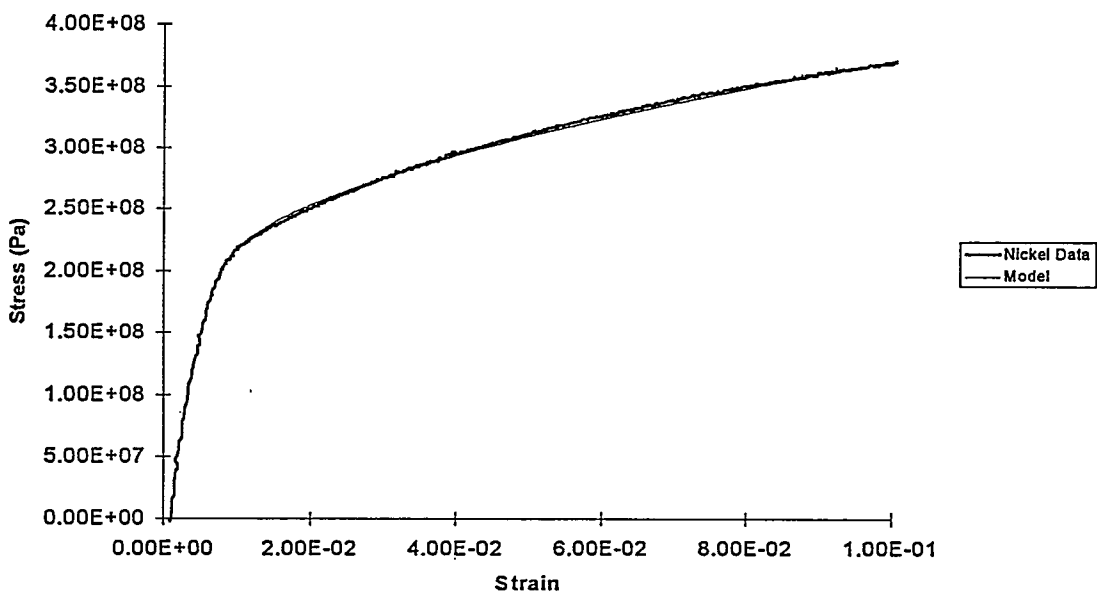


Figure 6.1 Modeling of Plasticity in Pure Nickel

6.4.3 Yield Strength

The compression tests are useful for revealing the onset of plasticity in materials that would fail before yielding in a tensile test. The true stress and true

strain were plotted and a 0.1% offset criterion was used to determine the onset of plasticity. The pure zirconia did not show any plasticity during these tests and failed by crushing.

The yield strength was also evaluated using hardness testing. When compared to the yield stress as determined by compression tests, The hardness data did not fit well with the standard relation:

$$H = 3\sigma_y \quad [6.2]$$

However, the data matched well with the equation:

$$H = 6\sigma_y \quad [6.3]$$

The same result was obtained by Sarafinchan (1995).

This result is unusual, although it may be explained by the effect of constraint during the hardness test. In hardness testing situations where material is forced upwards from the test surface, the hardness / yield stress ratio can become quite large. An example of this is in deep piercing (Fig 6.2) where the ratio is $H = 5\sigma_y$. In the interpenetrating phase materials, the nickel is constrained to flow through the gaps in the zirconia lattice. In effect, the nickel is extruded from one pocket into the next, and some of the material is pushed up through the surface.

The data for the yield stress, as determined in both the compression tests and the hardness tests, are plotted together in Figure 6.3, where the yield stress for the hardness data is plotted as $H / 6$. The values for pure zirconia are omitted because no plasticity was observed during the compression tests. The yield stress for zirconia, as calculated from the hardness values, would be 3.3 GPa.

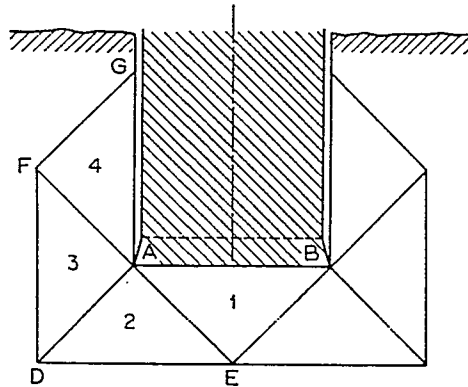


Figure 6.2 Illustration of Deep Piercing with $H = 5\sigma_y$. (Rowe, 1979)

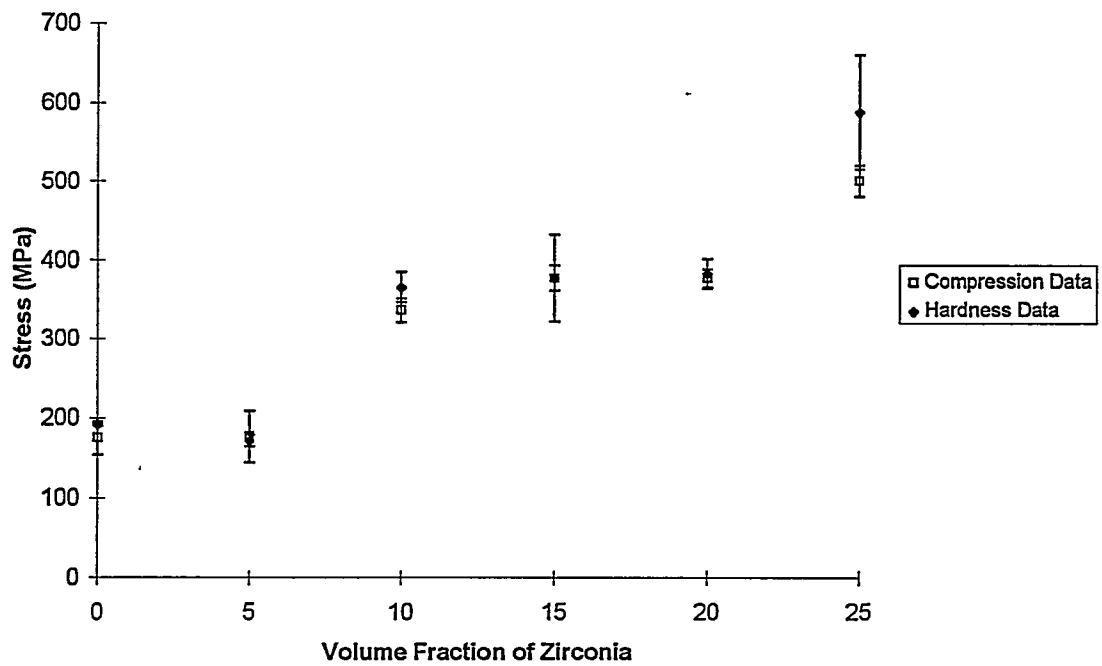


Figure 6.3 Yield Stress of Composites Determined Through Hardness and Compression Tests

These data can be interpreted either as experimental scatter about a straight line, or that the points fall into two distinct groups, with yield points of roughly 175 MPa and 380 MPa. The two materials with the lower yield point are both lacking a fully connected second phase that could provide constraint to plastic deformation in the nickel. All of the materials with higher yield points are above the percolation threshold and are supported by a lattice of zirconia which would prevent bulk plasticity until either it or the nickel-zirconia interfaces fracture. The yield stress of the 5% composite should be higher because of the reinforcing effects of the zirconia particles. However, porosity will result in stress concentrations within the material and will thus produce plasticity at a lower applied stress than would be found in a fully dense material.

More data on materials with different compositions are required to differentiate between a model with a plateau above the percolation threshold, and a simple linear relationship. Valid hardness data for a fully dense 5% composite are also required.

6.4.4 Young's Modulus

The Young's modulus of the composites was found to follow the linear relation:

$$212 + 0.27x \text{ GPa}$$

where x is the volume percentage of zirconia. The values of 212 GPa for pure nickel and 239 GPa for pure zirconia are in agreement with the published data for

these materials (Ashby and Jones, 1991). The apparent Young's modulus of the 5% sample is lower than the actual value because of porosity. Kelly and MacMillan (1986) indicate that the apparent modulus is found by multiplying by a factor $(1-3p)$, where p is the volume fraction of porosity. This would produce a 40 GPa change in the measured value of the 5% composite, bringing it within the expected range.

6.4.5 Microstructural Effects

A number of straightforward microstructural contributions to the properties of the nickel phase can be analyzed without dealing with the composite nature of the materials. The grain size of the nickel phase will have a strengthening effect, as will the presence of nickel carbide particles.

The Hall-Petch equation (Eqn. 2.9) describes the strengthening effect of grain size on a metal. The constant k is typically $0.1 \text{ MPa } \sqrt{\text{m}}$. Using this value, the increase in yield stress of the nickel phase will range from 31 MPa for the 5% material to 35 MPa for the 20% material, a difference of 4 MPa. This is insufficient to account for the 200 MPa difference in yield stress observed in the two groups of materials.

The presence of nickel carbide particles will also produce an Orowan strengthening effect within the nickel phase. A weight fraction of 0.025% carbon corresponds to a 0.12% mole fraction of carbon. If it is assumed that all of the carbon is tied up in the form of nickel carbide, and using a particle radius of

roughly 0.25 μm (Figure 5.19) this gives a particle spacing of roughly 2.8 μm . Assuming a Burger's vector of 2 \AA gives an increase in strength of approximately 5 MPa. This increase would be present in all of the composite grades except the pure zirconia, so would not differentiate the two groups. It is interesting to note that the calculated particle spacing is small enough to ensure that each nickel grain could contain several carbide particles, if there is no carbon in solution. Even relaxing this assumption significantly, and allowing 90% of the carbon to remain in solution would still leave the majority of grains with one or more nickel carbide particles to act as damage nucleation sites.

The properties of the nickel phase cannot explain the difference in yield strength between the 0% and 5% zirconia composites and the higher composite grades. The increase must therefore result from an interaction of the different phases. For the 25% composite, assuming a perfectly homogeneous distribution of zirconia in a nickel matrix (which is not in fact the case), the increase in yield strength due to Orowan effects would be approximately 110 MPa. This is derived from the equation:

$$\Delta\sigma = \frac{Gb}{l}$$

where G is the shear modulus of nickel, 78 GPa, b is the length of a Burger's vector, approximately 2 \AA , and l is the spacing of the particles. With a 25% volume fraction and a particle diameter of 0.18 μm , the particle spacing will be approximately 0.14 μm . This leads to a $\Delta\sigma$ of 109 MPa.

This is the maximum increase possible for this grade of composite, and the other grades would have a smaller increase because of the lower volume fraction of zirconia.

The properties of the composites are also affected by the residual strain present in the materials after cooling from processing temperatures. The residual stress in the nickel increases with increasing volume fraction of zirconia and exceeds the yield stress of pure nickel when the composite has greater than 20% volume fraction of zirconia. This can be derived from the simple equation:

$$\varepsilon_m = (1 - f_m)\Delta T\Delta(CTE) \quad [6.4]$$

where ΔT is the change in temperature, ΔCTE is the difference in thermal expansion coefficients, and f is the volume fraction of zirconia. The residual stress can be found by multiplying the residual strain by the Young's modulus.

Assuming that all of the residual stress is relieved by plasticity, and that the zirconia particles are discrete in order to provide an upper estimate, Miller and Humphries (1990) equation (Eqn 2.4) would predict an increase in dislocation density of 1×10^{14} . This would correspond to an increase in yield strength of 156 MPa. This is insufficient to account for the 550 MPa yield strength in the 25% composite. In addition, the microstructure observed in the composites does not meet the assumptions of the model, and gives a gross overestimate of the strengthening effect. This does, however, explain the difference between the 25% material and the rest of the percolating composites that have not experienced

plasticity in the nickel as a result of cooling. The plateau in the compressive yield strength and hardness data includes those composites with a percolating zirconia lattice, in which the nickel phase has not exceeded the yield stress due to differential thermal expansion.

From these results, it can be concluded that the presence of a percolating zirconia network increases the yield strength by at least 100 MPa.

The best explanation for this effect is the constraint of the metal phase by the presence of the ceramic. Ashby et al. (1989) found that lead wires physically bonded to the inside of a glass tube could show yield strengths approximately six times those found in unconstrained wires. The results were heavily dependent on the nature of the failure and whether interfacial fracture had occurred. However, in all cases the observed yield stress was at least twice as large as that of the unconstrained material. The presence of a percolating zirconia lattice will constrain the nickel and will produce a triaxial stress state. This effect, in combination with the additions from Orowan strengthening and the presence of carbides, can explain the observed yield stress in the composites.

6.5 Modeling Deformation

The stress strain curves of the tensile specimens were modeled using the simplified model of an IPC developed by Ravichandran (1994). The strain hardening exponent and constant were calculated from the pure nickel material. The values obtained were $K = 650$ MPa and $n = 0.55$. These data were combined

with the measured yield points of the specimens as no reasonable way of predicting these values was discovered. The equations 2.14, 2.17 and 2.18 were solved for stress and strain in terms of the parameter σ_3 , and the resulting curves were plotted along with the raw data from the tensile tests. The results are shown in Figures 6.4 through 6.6. The fit for the 5% material was very good, however the work hardening rate of the 10% composite increased above that found in the pure nickel. The 15% material displayed the expected elastic properties, but fractured in tension prior to the onset of plasticity.

The increased rate of work hardening can be explained by the accumulation of dislocation loops around the zirconia lattice arms. In a non-percolating material such as the 5% composite, the dislocation loops left around a particle after the passage of a dislocation can be eliminated through dislocation climb, or the dislocations can cut through the particle. In the percolating material this is not possible, as the lattice arm extends well beyond the glide plane and hence the dislocation loop cannot close. The same effect is observed in continuous fibre composites and is known as source shortening (Pedersen, 1990). It would also be difficult for the dislocation to cut the arm and displace it relative to the rest of a continuous lattice.

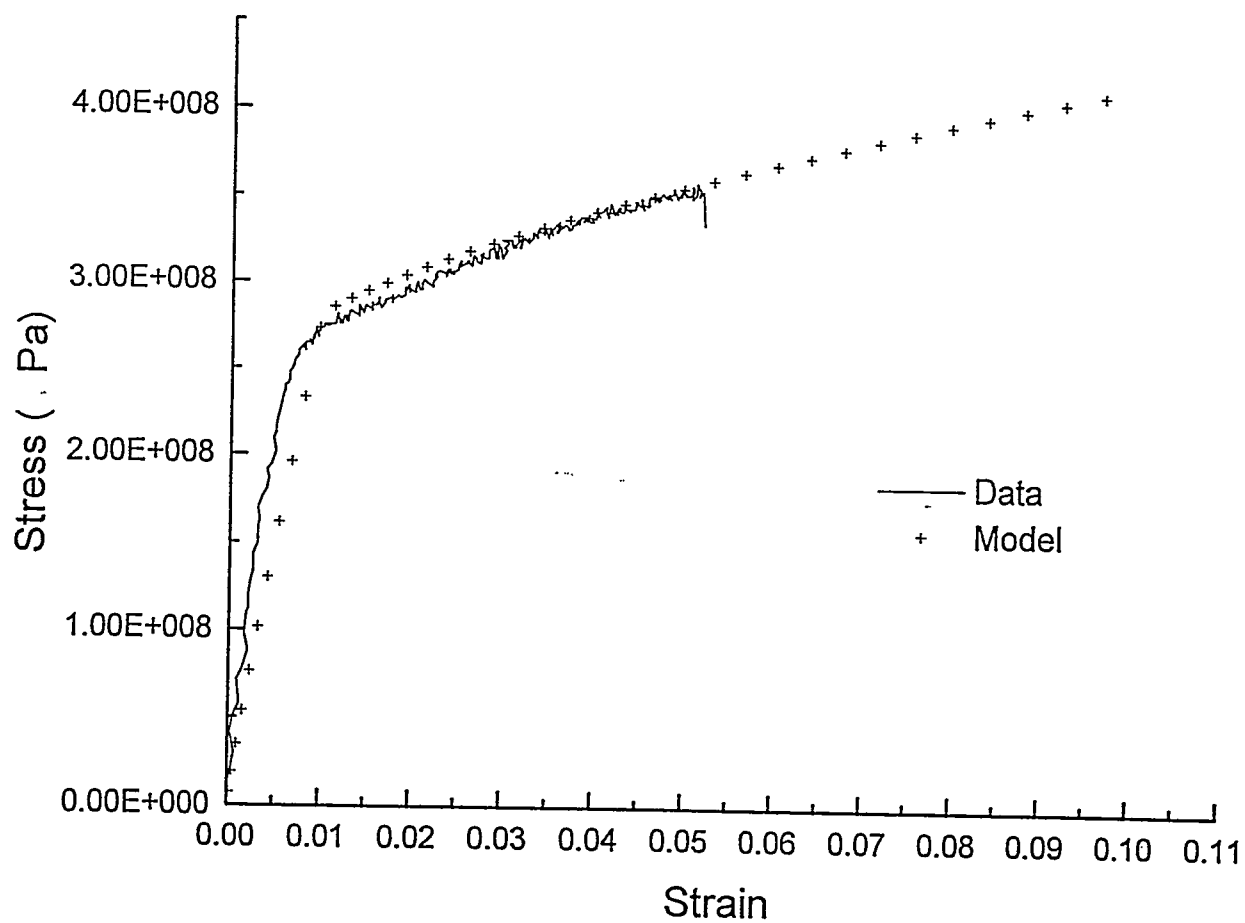


Figure 6.4 Model of 5% Zirconia Composite Based on Ravichandran (1994)

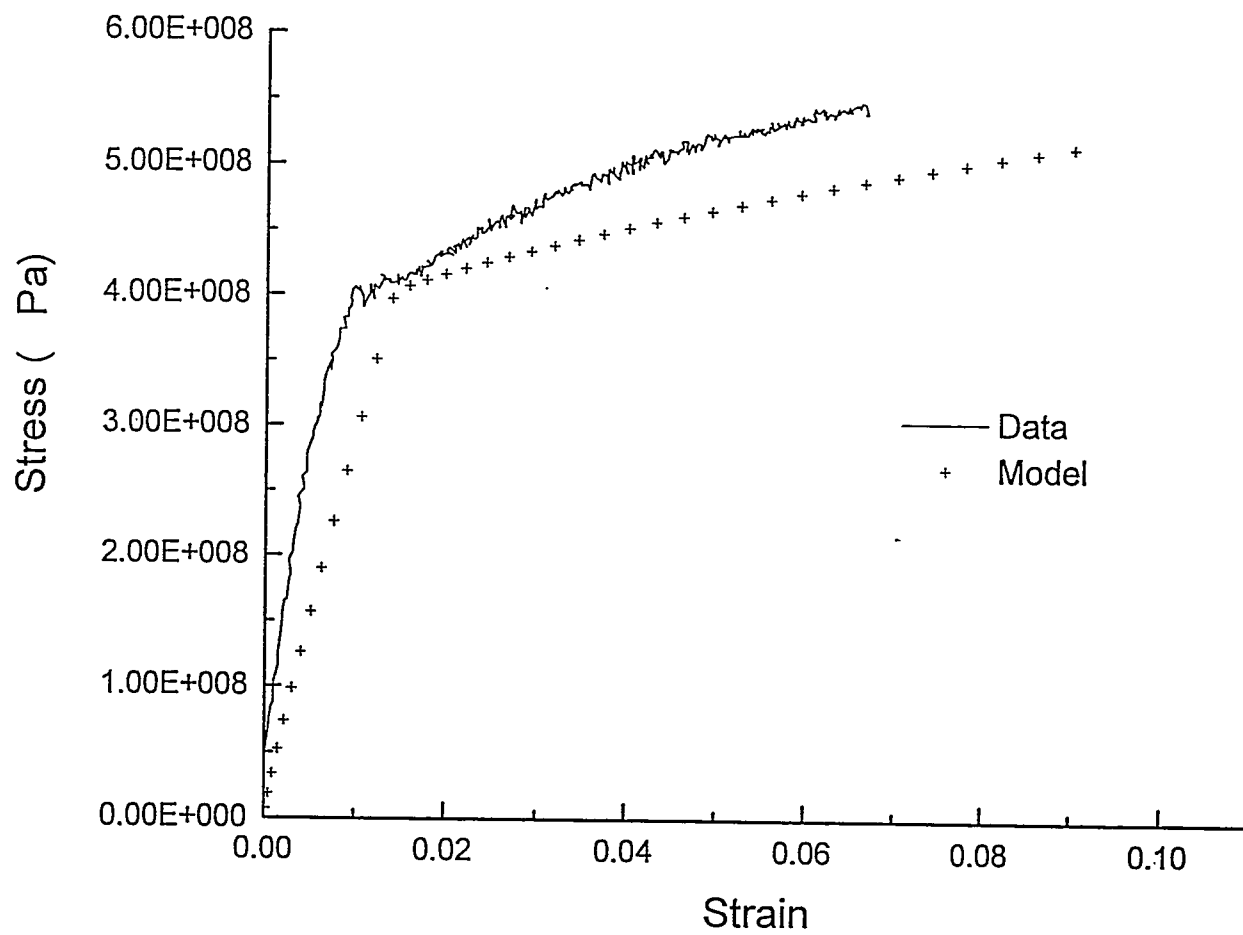


Figure 6.5. Model of 10% Zirconia Composite Based on Ravichandran (1994)

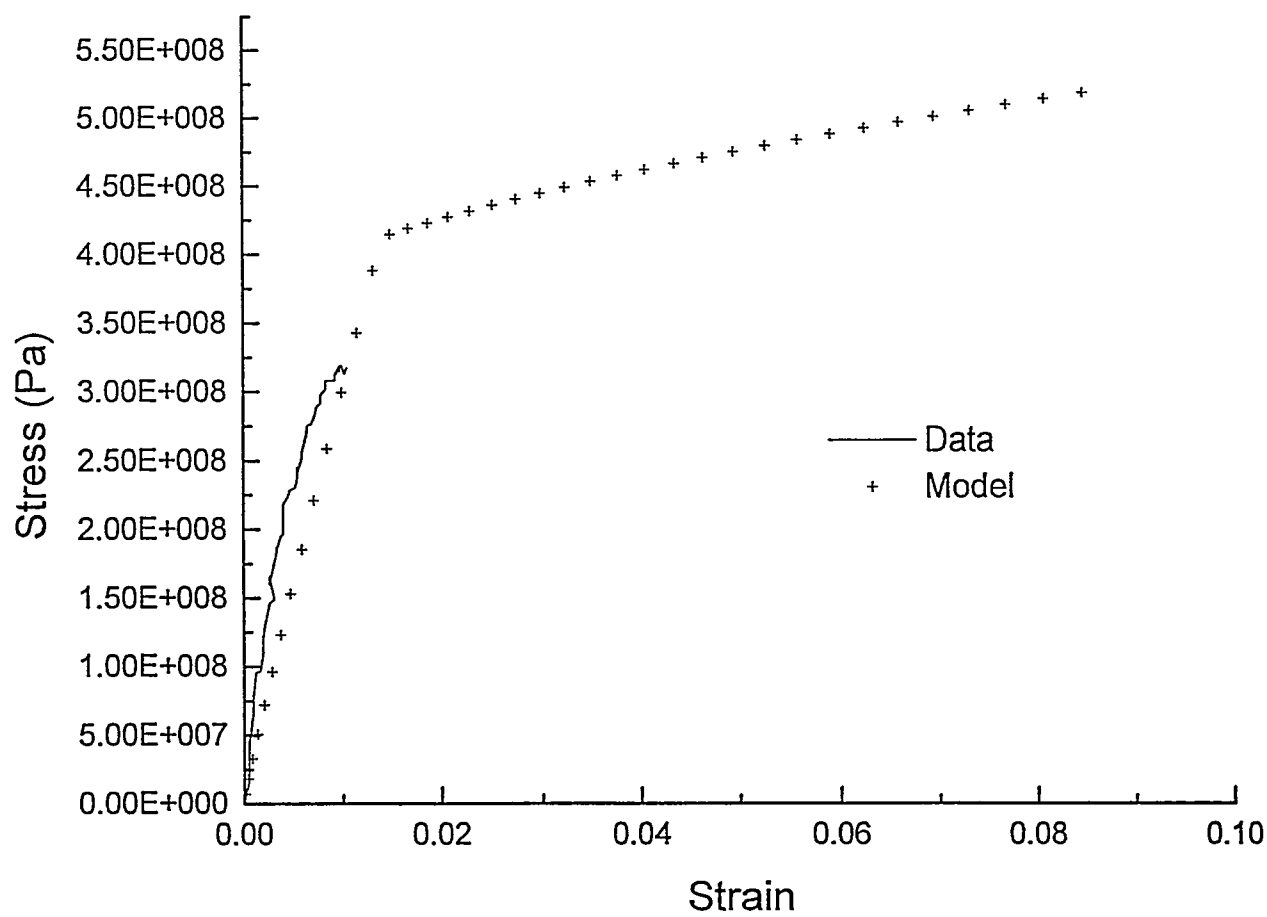


Figure 6.6. Model of 15% Zirconia Composite Based on Ravichandran (1994)

6.6 Summary of Mechanical Properties

In a typical MMC such as aluminum reinforced with silicon carbide the following trends are observed to occur (Clyne and Withers, 1993). The incorporation of reinforcement will increase the yield strength, and the yield strength will increase as the volume fraction of reinforcement increases. This can be the result of forest dislocations produced through differential thermal expansion, or through micromechanical effects such as Orowan strengthening. Load transfer to the reinforcing particles and interfacial fracture and pullout can also lead to strengthening through the increase of fracture toughness.

In addition, the ultimate tensile strength of a material will usually be increased by small amounts of reinforcement, but beyond some optimum level, the strength will decrease and can drop below that of the pure material. The strength is increased by load transfer to the stiffer material and constraint of the metal phase. Eventually, however, the volume fraction of ceramic becomes high enough to allow large critical flaws and fracture of the ceramic, and the subsequent fracture of the metal.

All of these trends are present in the nickel zirconia composites studied. The presence of a constraining lattice increases the yield stress, and increases the rate of work hardening. The ultimate tensile strength increases, and then drops as the phase size of the brittle ceramic component increases.

CHAPTER 7

SUMMARY AND CONCLUSIONS

The goal of this project was to gain an understanding of the mechanical properties of an IPC near the ceramic percolation threshold. The nickel / yttria stabilized cubic zirconia system was chosen in order to simplify processing and modeling because of the well matched thermal and elastic properties of nickel and zirconia. A colloidal processing routine was used in order to facilitate the production of functionally graded materials at some point in the future.

The tape casting, lamination, burnout and hot pressing procedure developed was capable of producing dense specimens in most cases, but was unreliable and difficult to optimize. The resulting materials had sufficient carbon remaining to produce nickel carbide particles.

The phase morphology was governed by the presence of the large nickel grains. A network of zirconia filled in gaps between abutting nickel grains, leading to agglomeration at low volume fractions, and a percolation threshold between 5% and 10% for the zirconia phase.

The nickel samples fractured in a ductile fashion through the coalescence of voids. The pure zirconia samples fractured in a mixed mode of intergranular and transgranular fracture. The 5% composite showed nucleation of 20 μm to 30 μm regions of damage on the fracture surface in the vicinity of zirconia particles, along

with smaller voids nucleated by smaller carbide particles. The 10% composite showed brittle fracture in the zirconia as well as regions of ductile fracture in the nickel. The higher zirconia volume fraction composite grades exhibited fracture of the zirconia matrix along with pull-out of nickel grains and ductile fracture of ligaments connecting adjacent grains.

Damage in a pure nickel sample was found to follow an exponential dependence on the local strain in the material. It was determined that there was no nucleation strain required for damage to occur, and that the residual porosity was 1.46%.

Mechanical testing of the composites was complicated by the transition from macroscopic ductility to brittle fracture. Only compression tests and hardness tests could be carried out on all grades. The addition of the reinforcing phase was seen to increase the yield strength of the composite. The ultimate tensile strength passed through a peak at a level of 10% zirconia and then decreased. The flexural strength of the 25% composite was the same as the tensile strength of the pure nickel.

At the low volume fractions of ceramic used in these materials, the flow stress of the nickel was not exceeded except in the case of the 25% zirconia composite. This can explain the plateau in hardness and yield stress for the 10%, 15% and 20% materials.

Modeling of the mechanical behaviour indicated that simple models based on the properties of the pure materials may not be appropriate for metal / ceramic

IPCs. The model by Ravichandran (1994) did not account for the increased work hardening observed in the percolating composite. This increased work hardening is caused by an effect similar to source shortening where dislocation loops around fibres increase the stress required for further loops to pass. This factor should be accounted for in future models of IPCs.

REFERENCES

- Anderson T.L. Fracture Mechanics : Fundamentals and Approach. CRC Press : Boston. pp. 42 (1991)
- Argon A.S., Im J., and Safoglu R. "Cavity Formation from Inclusions in Ductile Fracture". *Met. Trans. A* **6A** pp. 825-837 (1975)
- Ashby M.F., Blunt F.J., and Bannister M. "Flow Characteristics of Highly Constrained Metal Wires". *Acta Metall.* **37** pp.1847-1857 (1989)
- Ashby M.F. and Jones D.R. Engineering Materials 1 : An Introduction to Their Properties and Applications. Pergamon Press : Toronto. pp. 87. (1991)
- Bale R.A. and Chapman E.T. "Inco's Pressure Carbonyl Refining of Nickel". *CIM Proceedings : 25th Annual Conference of Metallurgists*. (1986)
- Cambridge Materials Selector. ed. Ashby, M.F. (1994)
- Cannon W.R., Morris J.R. and Mikeska K.R. "Dispersants for Nonaqueous Tape Casting". *Advances in Ceramics Vol. 19*. eds. J.B. Blum and W.R. Cannon. p 161-174, (1989a)
- Cannon, W.R. Becker, R. and Mikeska, K.R. "Interactions Among Additives Used for Tape Casting". *Advances in Ceramics Vol. 26*. eds. J.B. Blum and W.R. Cannon, pp. 525-541 (1989b)
- Clarke D.R. "Interpenetrating Phase Composites". *J. Amer. Ceram. Soc.* **75** pp. 739-759 (1992)
- Clayton D., McMaster University, unpublished work. (1997)
- Clyne T.W. and Withers P.J., An Introduction to Metal Matrix Composites. Cambridge University Press : Cambridge. (1993)
- Cox H., "The Elasticity and Strength of Paper and other Fibrous Materials", *Brit. J. Appl. Phys.* pp. 73-79 (1952)

Duxbury P.M., Leath P.L. and Beale P.D. "Breakdown Properties of Quenched Random Systems : The Random Fuse Network". *Phys. Rev. B.* **36** pp. 367-379 (1987)

Finnis M.W., Stoneham A.M. and Tasker P.W. "Approaches to Modeling Metal/Ceramic Interfaces". *Metal-Ceramic Interfaces.* eds. Ruhle M., Evans A.G., Ashby M.F., Hirsh J.P. pp. 35-44 (1990)

French J.D., Chan H.M., Harmer M.P. and Miller G.A. "Coarsening-Resistant Dual-Phase Interpenetrating Microstructures". *J. Amer. Ceram. Soc.* **73** pp. 2508-10 (1990)

French J.D., Chan H.M., Harmer M.P. and Miller G.A. "Mechanical Properties of Interpenetrating Microstructures : The $\text{Al}_2\text{O}_3/\text{c-ZrO}_2$ System". *J. Amer. Ceram. Soc.* **75** pp. 418-423 (1992)

Fukada H. and Chou T., "An Advanced Shear Lag Model Applicable to Discontinuous Fibre Composites" *J. Comp. Mat.* **15** pp. 79-91 (1981)

Griffith A.A. "The Phenomena of Rupture and Flow in Solids". *Phil. Trans. Series A.*, **221** pp. 163-198 (1920)

Henager C.H. and Brimhall Jr. J.L. "Solid State Displacement Reaction Synthesis of Interpenetrating-Phase Ni-Al/ Al_2O_3 Composites". *Scripta Metal. et Mat.* **29** pp. 1597-1602 (1993)

Hull D. and Bacon D.J. Introduction to Dislocations 3rd ed.. Pergamon Press : New York. pp. 244 et. seq. (1992)

INCO Material Safety Data Sheet, Type 123 Nickel Powder, (1996)

Kelly A. and MacMillan N.H. Strong Solids. Oxford University Press (1989)

Kingery W.D., Bowen H.K. and Uhlmann D.R. Introduction to Ceramics : Second Edition. John Wiley and Sons (1976)

Knechtel M., Prielipp H., Müllejans H., Claussen N. and Rodel J. "Mechanical Properties of Al/ Al_2O_3 and Cu/ Al_2O_3 Composites with Interpenetrating Networks". *Scripta Met. et Mater.* **31** pp. 1085-1090 (1994)

Lange F.F. "Powder Processing Science and Technology for Increased Reliability". *J. Amer. Ceram. Soc.* **72** pp. 3-15 (1989)

Le Roy G., Embury J.D., Edwards G. and Ashby M.F. "A Model of Ductile Fracture Based on the Nucleation and Growth of Voids". *Acta Met.* **29** pp. 1509-1522 (1981)

Meyers M.A. and Chawla K.K. Mechanical Metallurgy : Principles and Applications. Prentice-Hall : Toronto. p 410 (1984)

Miller W. and Humphreys F. "Strengthening Mechanisms in Metal Matrix Composites". *Fundamental Relationships Between Microstructure and Mechanical Properties of Metal-Matrix Composites* eds. Liaw and Gunger. TMS, pp. 517-41 (1990)

Mistler R.E., Shanefield D.J. and Runk R.B. "Tape Casting of Ceramics". *Ceramic Processing Before Firing*. eds. G.Y. Onoda, Jr. and L.L. Hench. pp. 411-448. (1978)

Nan C.W. "Physics of Inhomogeneous Inorganic Materials". *Prog. Mat. Sci.* **37** pp. 1-116 (1993).

Newkirk M.S., Urquhart A.W. and Zwicker H.R. "Formation of Lanxide™ Ceramic Composite Materials". *J. Mater. Res.* **1** pp. 81-89 (1986)

Pedersen O.B. "Thermoelasticity and Plasticity of Composites II - A Model System". *Acta Met.* **38** pp. 1201-1219 (1990)

Pickard S.M., Manor E., Ni H., Evans G. and Mehrabian R. "The Mechanical Properties of Ceramic Composites Produced by Melt Oxidation". *Acta Metall. Mater.* **40** pp. 177-184 (1992)

Prielipp H., Knechtel M., Claussen N., Streiffner S.K., Müllejans H., Ruhle M. and Rodel J. "Strength and Fracture Toughness of Aluminum/Alumina Composites with Interpenetrating Networks". *Mat. Sci. and Eng. A* **197** pp. 19-30 (1995)

Ravichandran K.S., "Deformation Behavior of Interpenetrating Phase Composites" *Composites Science and Technology.* **52** pp. 541-549 (1994)

Rice J.R. and Tracey D.M. "On the Ductile Enlargement of Voids in Triaxial Stress Fields". *J. Mech. Phys. Solids.* **17** pp. 201-217 (1969)

Richerson D.W. "Modern Ceramic Engineering : Properties, Processing and Use in Design", 2nd ed. pp. 519-545 (1992)

Rodel J., Prielipp H., Claussen N., Sternitzke M., Alexander K.B., Becher P.F. and Schneibel J.H.. "Ni₃Al/Al₂O₃ Composites with Interpenetrating Networks". *Scripta Metal. et Mat.* 33 pp. 843-848 (1995)

Roosen, A. "Basic Requirements for Tape Casting of Ceramic Powders" *Ceramic Transactions*, 1 : Ceramic Powder Science II, pp. 675-692 (1988)

Ruhle M. "Structure and Composition of Metal/Ceramic Interfaces". *J. Euro. Ceram. Soc.* 16 pp. 353-365 (1996)

Sarafinchan, D. "Processing and Characterization of Uniform Interpenetrating Ni-ZrO₂ Composites" M.Eng Thesis, McMaster University, (1995)

SGTE Phase Diagram Collection, Ni-C phase diagram (1997)

Skirl S., Hoffman M., Bowman K., Wiederhorn S. and Rodel J. "Thermal Expansion Behaviour and Macrostrain of Al₂O₃/Al Composites with Interpenetrating Networks". In Press (1997).

Stauffer D. and Ahonary A. Introduction to Percolation Theory : 2nd ed. Taylor and Francis : Philadelphia. (1994).

Stuijts A.L. "Ceramic Microstructures". *Ceramic Microstructures '76*. eds R.M. Fulrath and J. A. Pask. pp. 1-37 (1976)

Tuan W.H., Lai M.J., Lin M.C., Chan C.C. and Chiu S.C. "The Mechanical Performance of Alumina as a Function of Grain Size". *Mater. Chem. and Phys.* 36 pp. 246-251 (1994)

Velamakanni B.V. and Lange F.F. "Effect of Interparticle Potentials and Sedimentation on Particle Packing Density of Bimodal Particle Distributions During Pressure Filtration". *J. Amer. Ceram. Soc.* 74 [1] pp. 166-172 (1991)

Williams J.C. "Doctor Blade Process" from *Treatise on Materials Science and Technology Vol 9*. ed. F.F.Y. Yang, Academic Press, pp. 173-197, (1976)

Wu S. "Sintering Additives for Zirconia Ceramics". *Research Reports in Materials Science*. ed. P.E. Evans. pp. 6-38 (1986)

Wurst J.C. and Nelson J.A. "Lineal Intercept Technique for Measuring Grain Size in Two-Phase Polycrystalline Ceramics". *J. Amer. Ceram. Soc.* 55 pp. 109 (1972)